Ultra-low Temperature Magneto-transport and Spectroscopic Imaging

Soumyadip Halder

Department of Physical Sciences

Indian Institute of Science Education and Research, Mohali, Knowledge City,
Sector 81, SAS Nagar, Manauli PO, Mohali 140306, Punjab, India

Thesis submitted to IISER Mohali
for the fulfillment of the requirements for the degree

Doctor of Philosophy

March 2023

Dedicated to my parents

Acknowledgements

This thesis materializes with the immense support of many amazing people. Reaching the verge of my PhD, I express my gratitude and appreciation for their efforts. It is a far-fetched ambition to mention everyone's contribution here; still, I would make a sincere attempt.

First and foremost, I thank my supervisor Dr Goutam Sheet, who has been a constant support to my professional and personal front during this journey. His intuitive and scientific approach towards solving any problem has always inspired me. He has always encouraged me to take up challenges and follow through to the end, which improved my perspective towards science and life. Discussions with him and his valuable input in my research works would continue to benefit me to grow as an independent thinker and researcher in future. I am indebted to him for providing me unconditional access to all the instruments in the lab and trusting me with them, which improved my understanding of the instruments to minute details.

I am thankful to Dr Suvankar Chakraverty (INST), Dr Tanmoy Das (IISc), Dr Shantanu Mukherjee (IIT, Chennai), Dr Sanjeev Kumar (IISER Mohali) for their contributions to my research. I thank all my PhD committee members. Long hours in the lab were always enlightened by Mona and Nikhlesh, who have been the perfect teammates. One cannot ask for better juniors. I have always been motivated by their hard work and pushed myself to go the extra mile. I thank Deepti for being a very good lab partner. I thank Sandeep for being a very good friend. I have always appreciated his easygoing attitude and eagerness to help others in the lab. I'll always remember Soumya's constant presence as a friend in all the turmoils. I thank Dr Shekhar Das, Dr Ritesh Kumar, Dr Md Aslam, and Dr. Anshu Sirohi for their patience and for helping me understand some experimental techniques. And this list cannot be completed without Dr Shelender Kumar and Dr Sirshendu Gayen, who helped me construct my base in experimental physics. I also thank all my current lab mates.

IISER, for me, is not complete without Debsuvra Ghosh. He is the friend in need. The food and movie adventures with him are unforgettable. There are always a few people in everyone's life who may not be linked by blood, but the connection to those people is far stronger. In that regard, my gratitude towards Dr Pingal Dasgupta and Dr Tamal Sarkar is beyond words. The life of a researcher is no bed of roses, and the ups and downs during the journey could be exhausting at times. I am grateful to my wife, Dr Prantika Bhowmik, who remained by my side during all such difficulties and always motivated me. She has been the perfect elixir for me during difficult times. I have always been inspired by her work ethics, hardship and her perspective towards life.

I could not be what I am today without my parents. Their contributions and sacrifices towards my life are incalculable and beyond imagination.

Finally, I want to conclude this acknowledgement by thanking all the multimeters I have ever used in my life.

Abstract

The size of a physical system and the manifestation of quantum phenomena are closely related. With the size becoming smaller, the number of particles contained by a system is reduced, and the separation between the quantized energy levels increases. Consequently, the system reaches a limit where all or some of the observable phenomena are driven by a few quantum states rather than statistics. A measurable quantum signal is usually very small and also the particle statistics are determined by the system's temperature. As a result, it so happens that even if the size of the system is adequately small, the quantum signal is always suppressed by statistical thermal effects at high temperatures. Thus, quantum phenomena are observed in mesoscopic systems at ultra-low temperatures in general, and detecting such phenomena involves intense cryogenic instrumentation and modeling.

This thesis work is divided into two parts. The first part contains our work on the $LaVO_3$/ $SrTiO_3$ interfaces, where we discovered unconventional superconductivity. Further experiments revealed that the interface is highly disordered where superconducting islands separated by a bad metallic background are formed and the islands are percolatively connected. The superconducting phase can also be controlled by tuning the disorder with gate voltage. The second part contains our work on $PtSn_4$, where we have mapped the density of states with Scanning Tunneling Spectroscopy (STS) to extract the Quasi Particle Interference (QPI) pattern due to the presence of defect states. We used the same to reconstruct the momentum space and found evidence of Dirac node arcs. A summary of the thesis is given below chapter wise.

Perovskite oxide interfaces

Perovskite oxide interfaces have been a subject of interest to the scientific community for the last two decades not only because of the low dimensional nature of the possible conducting interfaces in them but also because the versatile characteristics in these interfaces are driven by the properties of the building materials. Very few of these conducting interfaces exhibit superconducting phase transition even at a very low temperature. In this chapter, I have

briefly discussed the history of conductive interfaces in perovskite oxide heterostructures and how conductivity emerges in such interfaces. I have also discussed a few of such interfaces which exhibit superconducting phases at a very low temperature.

Microscopic understanding of superconductivity

Superconductivity is a phenomenon where at a particular temperature, T_C, the resistance of a material becomes zero. Perfect diamagnetism along with zero resistivity differentiates a superconducting state from a perfect metallic state. Electrons as Fermions scatter from the defect sites, which causes finite resistance for a real metal even at zero temperature. However, in case of superconductors, the electrons pair up to make a Boson like state by interaction with lattice. These pairs are called Cooper pairs. The Cooper pairs condensate into a complex macroscopic quantum Bosonic ground state, $|\Psi_G\rangle$. Superconductivity can only be destroyed if sufficient energy is supplied to break all the Cooper pairs. $|\Psi_G\rangle$ has a global phase coherence which suggests that all the Cooper pairs should collectively maintain a constant phase. This phase stiffness does not allow scattering ande gives rise to zero resistance. When the Cooper pairs condensate, a gap, Δ (superconducting energy gap), opens up at the Fermi surface where there is no single particle (Fermion) states. Depending upon the symmetry of the gap, a superconductor could be categorized into *s*, *p* or *d* wave superconductors. A superconductor with a spherically symmetric gap (*s*-wave) can be explained in the framework of Bardeen Cooper Schrieffer (BCS) theory. Such superconductors are called conventional superconductors. The superconducting gap is experimentally measured by various techniques. Point contact Andreev reflection spectroscopy (PCARS) is one of the most used ones. For a mixed type or unconventional superconductivity (non *s*-wave gap symmetry), a sub-gap feature is also observed in the PCARS. In this chapter, I have briefly discussed the microscopic theory of superconductivity.

$LaVO_3$/ $SrTiO_3$

This chapter contains a brief discussion about $LaVO_3$/ $SrTiO_3$ interfaces. $LaVO_3$ is a Mott insulator, and $SrTiO_3$ is a band insulator. Band structure calculation shows that Ti-*d* bands from $SrTiO_3$ and V-*d* bands from $LaVO_3$ cross the Fermi level, and both of them participate in the electronic conduction. Further calculation for spin band structure suggests that V-*d* electrons are spin polarized. This also indicates that the superconductivity at $LaVO_3$/ $SrTiO_3$ interfaces probably is unconventional in nature.

$SrTiO_3$ is a quantum para-electric material which means that at low temperature (even at 0 K), $SrTiO_3$ is on the verge of becoming a ferroelectric but not a ferroelectric. The zero point quantum fluctuation does not allow for a ferroelectric transition in SrTiO3. However, it was observed that expansive strain on a $SrTiO_3$ thin film overpowers the quantum fluctuation and ferroelectric transition kicks in. $LaVO_3$/ $SrTiO_3$ interface has the potential to generate expansive strain due to lattice mismatch, which may cause ferroelectricity at the interface.

Cryogenic instrumentation

I have discussed the cryogenic instrumentation techniques used for transport measurements at $LaVO_3$/ $SrTiO_3$ interfaces. Previously, superconductivity was reported in similar kinds of materials at few hundred mK temperatures. Measurement at such a low temperature is extremely difficult. At this temperature, thermal conductivity is very low and thermalizing the sample is very challenging. Cooling power is also very low, which limits the magnitude of the current that can be sent through the sample for measurements. Consequently, the signal-to-noise ratio is also very small. We have used a dilution refrigerator with 350 μW cooling power at 100 mK and 10 mK base temperature at the mixing chamber (MC). The sample space is away from the MC but thermally connected to it via different thermal conducting materials like silver, coin-silver, copper etc. I have designed the sample space for our DC and low-frequency AC measurements. The base temperature of the sample space is around 27 mK. The sample space (sample holder and sample stage) is made of OFHC copper. Rogers RO4003C PCBs are used in the sample space for electrical connections. The use of coin silver instead of OFHC copper and Sapphire PCBs should noticeably increase the thermal performance. This chapter mainly contains brief discussions about the dilution refrigerator working principle, site preparation and lab set up for the installation of the dilution refrigerator, sample space design and performance, load lock chamber and breakout box design, the electronic measurement set up, experimental techniques, automated data acquisition process and logical flow charts of some programs.

$LaVO_3$/ $SrTiO_3$, experimental data and discussion

We have discovered superconductivity at $LaVO_3$/ $SrTiO_3$ interfaces. Our resistance vs temperature data exhibits superconducting transition onset at around 250 mK. The transition is broad, and the superconductivity is suppressed in the application of a magnetic field. At a magnetic field around 4.6 kG, the superconductivity is destroyed. The voltage vs current data also agrees with the fact that the interface is superconducting. To understand the nature of the superconductivity, we have employed a new technique, sub-surface point contact Andreev reflection spectroscopy (SSPCARS). We have found a sub-gap feature in the spectrum which is suppressed in the application of magnetic field, and the spectrum similar to that from a *s*-wave superconductor prevails. With increasing field, the superconducting feature in the spectrum was destroyed at about 2.7 kG. Our SSPCARS data is strikingly similar to that reported in a theoretical article about mix wave pairing superconductivity. We have also observed from our resistivity data that way below superconducting transition temperature, the resistance does not go to zero, although the superconducting transition is prominent. Our voltage vs current data also exhibits a finite slope at zero current value. Thus, we have concluded that our superconducting state is highly disordered. To explain the non-zero resistance, we have considered a model system where there are superconducting islands connected to each other by non-superconducting background. To investigate the superconducting state with finite resistance further, we have performed gate-dependent measurements. A gate electrode is connected at the bottom of the $SrTiO_3$ which is also called the back gate. We have observed that with changing gate voltage, the T_C and H_{C_2} for the superconducting state do not change. The finite resistance at the superconducting state, however, changes dramatically. If the gate voltage is increased on the negative side, resistance for both the normal state and the superconducting state increases. The opposite phenomenon was observed when the gate voltage was increased on the positive side. Our Hall measurement also confirmed that gating does not change the carrier density appreciably. To employ all such effects in our model, we considered that $SrTiO_3$ is ferroelectric at the interface, which essentially changes the superconducting islands' sizes with gate voltage.

Scanning tunneling spectroscopy (STS) and quasi-particle interference (QPI)

STS is an energy-resolved surface-sensitive measurement to estimate the relative local density of states (LDOS) on a clean surface. For a perfect crystal with no defects, the quantum states are pure Bloch states, and the LDOS has no contribution from momentum, k. However, impurities in a crystal act as scattering centres for Bloch states. The Bloch states elastically scatter from the defects and mix up. In such a case, the LDOS has k dependence, which can be observed as ripples in the LDOS map. This is called QPI. Depending upon the chosen system, some of the k states have higher probability of mixing for which the ripple intensity will be maximum. Taking a Fourier transformation of LDOS, one can identify such k values and reconstruct the surface bands. All the LDOS maps are acquired at different energy values in an ultra high vacuum environment. In this chapter, I will discuss general STS technique and QPI analysis technique.

$PtSn_4$, STS data and discussion

$PtSn_4$ is a topologically non-trivial material, accommodating a Dirac node arc in the band, that emerges from the surface states. $PtSN_4$ has an orthorhombic crystal structure and the LDOS data was acquired on a [010] surface. Before measurement the surface was cleaved in UHV at 77k to expose the dirt free layer. Cleaving $PtSn_4$ surface may result in exposing either Pt layer or Sn layer. In our case by determining the lattice constants from the topographic image we concluded that the exposed layer was the Pt-layer. Atomic resolution topographic images were taken to select an area for LDOS measurements. Our experimental QPI data has a good match with that constructed from band structure calculation. Our data also capture the signature of nodal arc states.

Concluding remarks

We have discovered superconductivity at $LaVO_3$/ $SrTiO_3$ interfaces and achieved precise control of the superconducting phase by in-situ disorder tuning with gate voltage. This interface is a potential system to study disordered low-dimensional superconductivity where exotic phases (like Bose metal) may be observed by tuning the disorder.

From the LDOS mapping of the $PtSn_4$ surface, we have acquired QPI patterns for both the valence bands and the conduction bands. The QPI patterns generated from the theoretical band structure calculation also match to a good extent with our experimental data. From our QPI spectroscopy we provide an evidence of $PtSn_4$ being a nodal arc semimetal.

Research publications emanating out of this thesis work

(1) Unconventional superconductivity at $LaVO_3$/ $SrTiO_3$ interfaces, *ACS Appl. Electron. Mater.*,2022, 4, 12, 5859–5866, Halder et al.
(2) Spectroscopic observation of Dirac arc nodes and inter-arc mixing in PtSn4, Halder et al. (in preparation).
(3) Electric-field-tuned disorder, controlling superconductivity in $LaVO_3$/ $SrTiO_3$ interfaces, Halder et al. (in preparation).

Table of contents

List of figures **17**

List of tables **23**

1 Conductive Interfaces in Perovskite Oxide Heterostructures **1**

1.1 Introduction 1

1.2 The beginning 1

1.3 Origin of conductive interface 4

1.3.1 Polar catastrophe 5

1.3.2 Oxygen vacancy doping 6

1.3.3 Cation intermixing 6

1.4 Superconductivity at insulating oxide interfaces 7

1.5 Conclusion 9

2 Microscopic understanding of superconductivity **11**

2.1 Introduction 11

2.2 Second quantization 14

2.3 Bardeen, Cooper and Schrieffer (BCS) theory 16

2.4 Types of superconductors 22

2.5 Conclusion 23

3 $LaVO_3/SrTiO_3$ interface **27**

3.1 Introduction 27

3.2 Possible interfacial properties 28

3.3 Conclusion 30

3.4 Contribution 31

4 Cryogenic instrumentation **33**

4.1 Introduction 33

4.2 Noise isolation 34
4.2.1 Acoustic noise 34
4.2.2 Electronic noise 34
4.3 Dilution refrigerator 35
4.4 Sample space 38
4.5 Thermometry and measurement electronics 40
4.6 Experimental methods 41
4.7 Data acquisition 42
4.8 Conclusion 42
4.9 Contribution 43

5 $LaVO_3$/ $SrTiO_3$, Experimental data and discussion 59
5.1 Introduction 59
5.2 Sample preparation 59
5.3 Discovery of unconventional superconductivity at $LaVO_3$/$SrTiO_3$ interfaces 60
5.3.1 Methods 60
5.3.2 Data, analysis and discussions 62
5.4 $LaVO_3$/$SrTiO_3$ interface: a ferroelectric controlled superconductor 68
5.4.1 Methods 68
5.4.2 Data, analysis and discussion 70
5.5 Conclusion 79
5.6 Contribution 80

6 Scanning tunneling spectroscopy (STS) and quasi-particle interference (QPI) 83
6.1 Introduction 83
6.2 Scanning Tunneling Spectroscopy (STS) 83
6.3 Quasi particle interference (QPI) 87
6.4 Conclusion 88

7 $PtSn_4$, STS data and discussion 89
7.1 Introduction 89
7.2 Data and discussion 90
7.3 Image analysis 94
7.4 Conclusion 96
7.5 Contribution 97

8 Concluding remarks 99

Bibliography **101**

List of figures

1.1 Graphic representation of two Perovskite Oxide crystals with different A and B and their interface. '#' represents an arbitrary relation between Properties X and Y at the interface, which defines the interfacial properties of the system. 2

1.2 Graphic representation of the polar catastrophe mechanism. As can be seen, the potential builds up across $LaAlO_3$ due to the stacking of +1 and -1 charged layers in an alternating fashion. To avoid such polar catastrophe, -0.5 charge migrates to the interface, leaving +0.5 charge on the $LaAlO_3$ surface behind, and the effective potential across $LaAlO_3$ becomes zero. . . 5

2.1 **a** $H_C - T_C$ phase diagram of a superconductor. **b** electronic heat capacity vs temperature graph shows a finite jump at T_C 12

2.2 Diagram of a phonon exchange process between two electrons with momentum k and k' 17

2.3 Two Fermi spheres with radii k_F is drawn at O and O' to represent the available states for each electron. 17

2.4 Plot of v_k^2 vs $\bar{\varepsilon}_k$ at absolute zero temperature **a** for normal metal, **b** for superconductor. 20

2.5 Different gap symmetries for superconductors 23

2.6 **a** $\rho_S(E)$ vs E graph. The blue vertical line represents the interface between normal metal and superconductor. An electron from the metal side is reflected as a hole at the interface, and a Cooper pair forms. **b** The dark grey area represents superconducting material, and the light grey area represents normal metal (tip in this case). The mesoscopic contact can be considered as a combination of parallel tunneling (red lines) and ballistic (black lines) channels. Differential conductance spectrum for pure ballistic regime (**c**), pure metallic regime (**e**),combination of ballistic and tunneling regime (**d**). . 26

3.1 Graphical representation of $LaVO_3/SrTiO_3$ [001] (left top) and $LaVO_3/SrTiO_3$ [111] samples with their respective polar stacking is shown. For both cases, resistivity vs temperature data is presented (right top and right bottom). . . 28
3.2 Supercell structure used for band and spin band structure calculations. . . . 29
3.3 Band structure of (A) $LaAlO_3/SrTiO_3$ [001] and (B) $LaVO_3/SrTiO_3$ [001] interfaces. 29
3.4 Spin band structure of (A) $LaAlO_3/SrTiO_3$ [001] and (B) $LaVO_3/SrTiO_3$ [001] interfaces. 30

4.1 3D model of massive concrete block, also known as pit, to minimize acoustic noise. 44
4.2 A photo of the pit after construction. 45
4.3 A photo of the electronic measurement setup 46
4.4 **Left** phase diagram of liquid 3He and 4He mixture. **Right** schematic of a dilution refrigerator(DR). The percentages are approximated for 0K operation. Commercial DR can reach down to 2 mK base temperature. 47
4.5 Simplistic model of dilution refrigerator. 47
4.6 A photo of the dilution refrigerator 48
4.7 3D model of the load lock chamber designed using Solidworks. There are two CF 200 windows opposite to each other (one is visible here) and two CF 150 windows opposite to each other (one is visible here). One of these windows is opened for access to the shuttle. CF 50 flange at the bottom is connected to the DR top. The manipulator assembly is connected to the CF 63 flange on top. The rest of the ports are for pumping or pressure gauge attachment. 49
4.8 Image and 3D model of the shuttle. The sample space inside the shuttle is visible. 50
4.9 3D model of the sample space, designed in solidworks. The sample space has two parts, namely: sample stage and sample holder. The vertical collage of small images on the right hand side represents the sample holder and sample stage relative positions just before the sample holder insertion. The white arrow shows the direction of insertion. 51
4.10 Locking mechanism for sample holder. The white bidirectional arrow shows the movement of wing during the sample holder insertion. 52
4.11 3D model of the sample stage at an intermediate step of the assembly. The image shows the thermal anchors. 53

4.12 Last step of the sample stage assembly. The zoomed image of the pogo-pin is for the dimensional reference. 54

4.13 The PCB is designed using Eagle CAD. In the design, the color red represents the top copper layer, and the color blue represents the bottom copper layer. The green color represents a through hole. Yellow lines in the design are the boundaries of the PCBs. The images of the PCBs are also shown here. . . 55

4.14 Circuit diagram for gate-dependent measurements. The light and dark grey layers in the sample represent $LaVO_3$ and $SrTiO_3$, respectively. The interface is conducting. S, A, B, and D are the contacts to the interface. S and D stand for source and drain, respectively. A and B are voltage probes. 56

4.15 Circuit diagram for sub-surface point contacts Andreev reflection measurements. The light and dark grey layers in the sample represent $LaVO_3$ and $SrTiO_3$, respectively. The interface is conducting. S, B, A, and D are the contacts to the interface and contact A is assumed to be in the ballistic regime. 56

4.16 Logical flow chart of the magneto/ Hall resistance program, part-1 57

4.17 Logical flow chart of the magneto/ Hall resistance program, part-2 58

5.1 **Preparation of 2DEG at the $LaVO_3/SrTiO_3$ interfaces: a** The schematic of the $LaVO_3/SrTiO_3$ s. **b**, **c** the AFM image and RHEED pattern of the (001) $SrTiO_3$ before deposition, respectively. **d**, **e** the AFM image and RHEED pattern for the $LaVO_3/SrTiO_3$ surface after deposition, respectively, showing a smooth crystalline growth of film. **f** RHEED oscillations for the films grown at $4J/cm^2$ laser fluence as a function of time indicate the controlled deposition of $LaVO_3$ film over (001) $SrTiO_3$ substrate. **g** The sheet resistance of the sample. The *inset* shows the Hall measurement of the $LaVO_3/SrTiO_3$ interface at 300K. R_{yx} instead of R_{xy} was measured here, which resulted in an opposite slope in Hall measurement for the n-type carrier. 61

5.2 **Evidence of superconductivity at $LaVO_3/SrTiO_3$ interfaces. a** Sheet resistance (R) vs. temperature (T) of the interface at magnetic fields up to 4.5 kG along $+\hat{z}$ (vertically up). **b** V vs. I characteristics at magnetic fields up to 4.5 kG along $+\hat{z}$. The *inset* in **a** shows $H_c - T_c$ phase diagram. 64

5.3 **a** dR/dT vs T derived from the R-T data taken at 0 kG for the superconducting state. **b** Calculated error values for T_C measured at different field. The inset shows the parameters for the linear fit. 65

5.4 **Indication of unconventional superconductivity:** **a** Temperature dependence of normalized differential conductance $\frac{dI}{dV}$ *vs* applied DC bias (V). The lowest temperature and zero field data is shown as a black line (in both **a** and **b**). **b** Magnetic field dependence of normalized differential conductance $\frac{dI}{dV}$ *vs* applied DC bias (V). The *inset* shows a double peak feature around $V = 0$ at higher magnetic fields in 2D plots. 67

5.5 PCS spectra for the ballistic point contact at higher magnetic field values showing the zero bias feature becoming flatter with increasing magnetic field. 68

5.6 Spectra showing critical current dips(indicated by black arrows) on different point contacts. In these spectra, the signature of the low-bias slope change(indicated by red arrows) are also seen. This could be due to non-zero contribution of Andreev Reflection in an intermediate regime. 69

5.7 Graphic representation of a model that may explain the non-zero resistivity of the superconducting state. The deep blue structures are superconducting islands, separated by bad metallic background (light blue). 71

5.8 Resistivity R vs temperature T graph at different gate voltages. T_C does not change appreciably with gate voltage. 72

5.9 Hall data recorded at different gate voltages at 350 mK. The carrier density is more or less constant at different gate voltages. 73

5.10 Example of a non-local probe configuration on a disordered system (island system in our case). Probes S and A are connected to two superconducting islands, whereas probes B and D are connected to the background. S and D represent the source and the drain, respectively. B and D are voltage probes. The current from S to D can be divided into different paths: SAD and SBD are two such paths on which probes A and B are located. 74

5.11 Hall data (red dots) recorded at $V_G = 0$ at 350 mK. The straight grey line is the reference for an imaginary linear hall effect with the same initial and end data points. 75

5.12 Voltage V vs current I graph, recorded at 27 mK at different gate voltages. . 76

5.13 Resistivity R vs temperature T graph, recorded at 27 mK at different gate voltages. H_{C_2} does not change with gate voltage. 77

5.14 The size of the superconducting island changes with varying gate voltage, V_G. For higher V_G value on the negative side (V_G-), the superconducting islands' size decreases, whereas, on the positive side (V_G+), the superconducting islands grow in size. 80

5.15 Resistivity vs temperature data recorded at -100V gate voltage in the absence (brown) and presence (black) of the magnetic field. Similar data was recorded at -120V gate voltage in the absence (green) and presence (red) of the magnetic field. The gray arrows point to the region where metal-to-insulator transitions occur in the black and red graphs. 81

5.16 **a** Derivative of the resistivity vs temperature graph with respect to the temperature recorded at -80V gate voltage. The graph is noisy. **b** Similar graphs after 100 points averaging. **c** Considering T_C to be the peak positions of the respective graphs in **a** T_C vs gate voltage is plotted. 82

6.1 **a** STM circuit diagram. The yellow patches on the piezo, marked as X+, Y+ and Z, are electrodes to drive the tip along X, Y and Z directions. X- and Y- electrodes are located at the opposite sides of the X+ and Y+ electrodes (not shown here). V is the applied voltage between the tip and the sample. The orange dot on the sample represents the position on the sample where the tip is scanning. The tip is exactly above the orange dot and not touching the sample. The tunneling current runs through an amplifier marked as 'Amp' here. The output from the amplifier is measured.**b** STS mapping/ $\rho(E)$ mapping at different energy values. Respective axes are shown. Each rectangle on the stack represents ρ as a function of X and Y at different energy values. There should be an infinite number of such rectangles to cover the whole energy spectrum. However, for any material, a certain energy range is only relevant. The red rectangle represents the ρ map at the Fermi energy E_F. **C** the atomic resolution image of the surface of a sample ($PtSn_4$), acquired by STM. Ideally, the image should represent the summation of all rectangles in the stack, but for a metal above E_F, ρ should be zero. Thus, it is sufficient to consider energy up to E_F. **d** ρ mapping of the $PtSn_4$ surface, a rectangle out of the stack. 85

7.1 **a** R-T data of the crystal. The orthorhombic unit cell of $PtSn_4$ is shown in the inset, **b** Atomic resolution image of cleaved surface of $PtSn_4$ **c** Large area topograph (154nm×154nm) showing bright and dark defects recorded at V_b = 100 mV and I_t=290pA. **d** dI/dV map of the topographic image shown in **c**.) 91

7.2 **a-d** Experimentally measured QPI images for energies 50 meV, 100 meV, 200 meV and 300 meV. **e-h** shows the corresponding constant energy surfaces. **i-l**) are the simulated QPI plots with in a full BZ ($-\pi$ to π). 92

7.3 **a-d** Experimentally measured QPI images for energies -40 meV, -50 meV, -100 meV and -200 meV. (e)-(h) shows the corresponding constant energy surfaces. **i-l** are the simulated QPI patterns with in a full BZ (-π to π). . . . 93
7.4 **a** The experimentally extracted QPI patterns for -15 meV. **b** A qualitative sketch of nodal arc state. Relevant q vectors (q_1, q_2, q_3) are showing by the green arrows. 94
7.5 Oblique corrected DOS map for -20 mV. The checker pattern is to represent the lattice after correction. Each node of the checker pattern represents one Pt atom. 95
7.6 Brillouin zone cut of the symmetrized FFT. 96
7.7 After 2 pixels averaging to smooth the data 97
7.8 Final QPI data after background subtraction. 98

List of tables

4.1 Properties of cryogenic liquids 36
4.2 Thermal performance of the sample space compared with the MC performance 40
4.3 List of temperature sensors and heaters 40

Chapter 1

Conductive Interfaces in Perovskite Oxide Heterostructures

1.1 Introduction

Perovskite Oxide materials are often mentioned as Lego blocks in material science. The composition formula of such materials is ABO_3 where A and B are usually alkaline and d- block elements, respectively. With variations of different A's and B's, the material properties could be changed. For example, for a particular A and B, the material could show ferromagnetic behaviour; for another A and B, the material may show ferroelectric behaviour. What is convenient about such materials is that the lattice parameters for different A's and B's are almost the same, which enables preparing heterostructures of such materials without many technical difficulties. Hence it's called the 'Lego blocks'. When a heterostructure is grown, the interface tends to have properties from both the building materials or some new interfacial properties may emerge. A famous example of such heterostructure is $LaAlO_3$/ $SrTiO_3$ where both the building materials are although electrical insulators, but the interface is conductive [1]. Additionally, the BO_6 octahedral crystal structure tends to be preserved throughout the whole heterostructure, which, consequently contributes to the electronic and structural stability of the system. This is more relevant for a heterostructure with same B and different A's, e.g., $LaTiO_3$/ $SrTiO_3$ [2].

1.2 The beginning

In 2002 Ohtomo et al. first observed the emergence of conductivity in the interface of $LaTiO_3$, a Mott-Hubbard insulator and $SrTiO_3$, a band insulator [2]. A superlattice of $LaTiO_3$ and

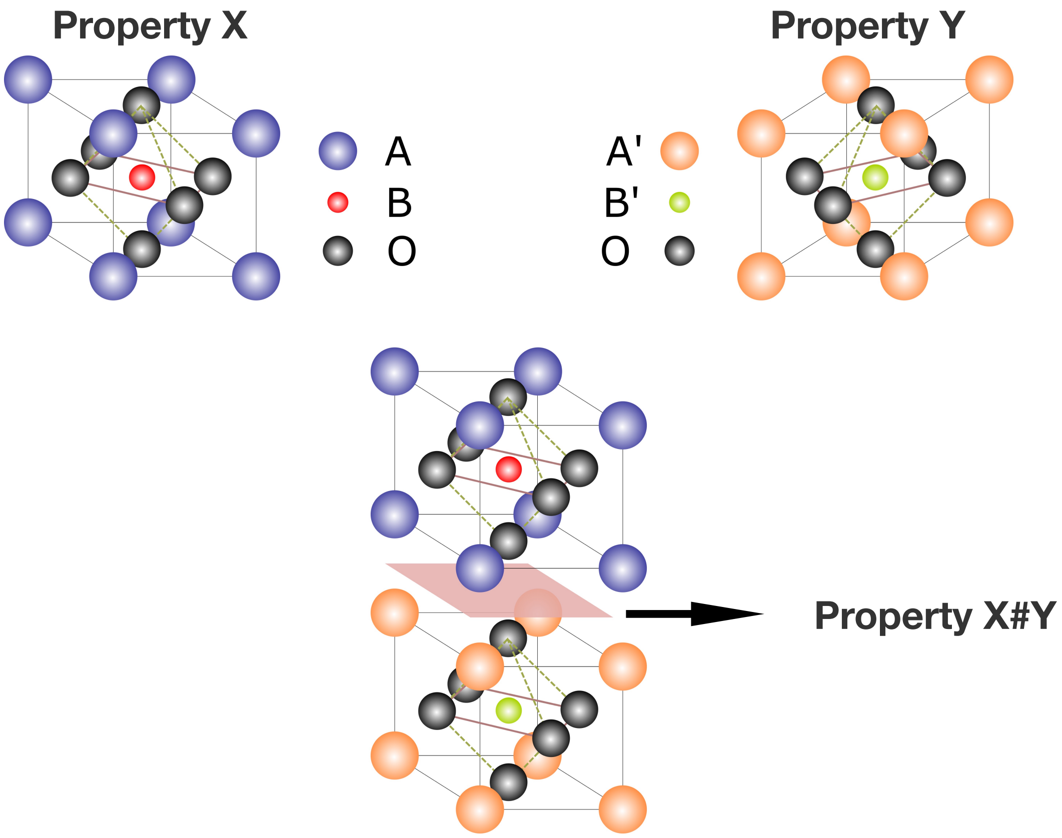

Fig. 1.1 Graphic representation of two Perovskite Oxide crystals with different A and B and their interface. '#' represents an arbitrary relation between Properties X and Y at the interface, which defines the interfacial properties of the system.

$SrTiO_3$ with variable thickness profiles was grown over a TiO_2 terminated $SrTiO_3[100]$ surface. The sample cross section along the [001] zone axis was probed with scanning transmission electron Microscopy (STEM) in annular dark field (ADF) mode. The ADF imaging also enabled the authors to record the titanium $L_{2,3}$ and lanthanum $M_{4,5}$ edges simultaneously in electron energy loss spectra (EELS) mode. The data confirms the presence of Ti^{3+} signal in the vicinity of La columns with a prominent peak about La sites. It was also observed that at 5 monolayer thickness of $LaTiO_3$, the peak value corresponds to that of 100% Ti^{3+} state. This diffusion of Ti^{3+} states towards the $SrTiO_3$ layers where the usual Ti oxidation state is Ti^{4+}. This implies that a fraction of the Ti^{4+} states in the $SrTiO_3$ layers adjacent to the $LaTiO_3$ layers becomes Ti^{3+}. This reduction of the Ti oxidation state is driven by some electronic reconstruction at the junctions to accommodate extra electrons in the $SrTiO_3$ layers, which consequently participate in electrical conduction. It was noticed as well that the fraction of Ti^{3+} also varies with $LaTiO_3$ layer thickness. In the later part, we shall also see that Ti d bands primarily participate in conduction in $SrTiO_3$ based Perovskite-Oxide heterostructures.

It was evident that to alter the insulating nature of ABO_3 type materials, elements of variable valencies, to the first order approximation, are required (usually at B sites) that may harbour the conducting electrons. In 2004 Ohtomo et.al discovered conductivity at $LaAlO_3$/ $SrTiO_3$ interfaces [1] with a low temperature mobility of the order of 10,000 $cm^2V^{-1}s^{-1}$. Such high mobility of a low dimensional conductor indicated that quantum electronic transport could be observed in the system. The authors indeed found quantum oscillations in the magnetoresistance measurements. The importance of this work lies in the optimisation of the $SrTiO_3$ substrate condition to attain the conductive interface. Perovskite ABO_3 structures can be considered as AO and BO_2 sheets stacked alternatively along the [001] direction. For example, along the [001] direction, $LaAlO_3$ crystal is composed of alternate AlO_2 and LaO stacks with $-e$ and $+e$ net charge, whereas $SrTiO_3$ crystal is composed of charge neutral TiO_2 and SrO stacks. It is evident that there is a polar discontinuity at the interface. It was verified that the dominant mechanism responsible for charge reconstruction at the interface, which leads to conductivity, is polar discontinuity. However, the possibility of oxygen vacancy at the interface during the growth could not be denied; after all, the growth depends upon extensive environmental parameters. $SrTiO_3$ could be chemically processed to terminate at TiO_2 or SrO plane along 001 direction. It was found that only the interface between $(LaO)^+$ and $(TiO_2)^0$ conducts, and inserting a single monolayer of SrO before growing $LaAlO_3$ completely mutes the conductivity. The dimension of the conductive layer was interpreted from the oscillation of the magnetoresistance with increasing magnetic field value. The authors measured the magnetoresistance oscillation with the applied field along and perpendicular to the sample plane. The oscillation frequency was observed to be independent of the field direction, which suggested that the obtained metallic layer was rather 3- dimensional in nature.

It should be noted that among Sr, Ti, Al, La and O, only Ti has variable valency. Thus this observation was also consistent with the fact that elements with variable valencies are one of the requirements for producing conductive interfaces in Perovskite Oxide heterostructures.

100% Ti^{3+} signal about La ions for 5 monolayer thickness of $LaTiO_3$ in the case of $LaTiO_3$/ $SrTiO_3$ already led to speculation of a connection between conductivity and critical donor layer thickness. In 2006 Thiel et. al [3] reported that in the case of $LaAlO_3$/ $SrTiO_3$, the critical thickness of the $LaAlO_3$ layer must be 4 unit cells for the interface to conduct. However, the interface conductivity could be modulated with a gate voltage. The authors demonstrated that the application of an adequate gate voltage at a conducting/non-conducting interface turned it into non-conducting/ conducting. These gate-dependent metal-insulator transitions were investigated for samples with close to critical donor layer thicknesses (3,5,6 unit cells etc.).

Followed by the discovery of conducting interface at $LaAlO_3$/ $SrTiO_3$ junction several $SrTiO_3$ based Perovskite Oxide heterostructures with conducting interfaces were developed, e.g., $LaTiO_3$/ $SrTiO_3$ [4; 20], $GdTiO_3$/$SrTiO_3$ [5], $LaVO_3$/$SrTiO_3$ [6] etc. In our case, we have selected the $LaVO_3$/$SrTiO_3$ interface as our device under test. In the past decade $SrTiO_3$ based conducting oxide heterostructure interfaces have been a popular playground to hunt for reach and novel physics. The other popular choice is $KTaO_3$ based heterostructures [7–9], where like Ti, Ta also owns variable valencies. Additionally, $KTaO_3$ possesses high spin-orbit coupling, which introduces non-trivial phenomena to the interfaces. However, with all these discoveries, $LaAlO_3$/ $SrTiO_3$ interface, for its diverse properties, some of which were discovered later in the timeline(superconductivity, magnetism etc.), is still considered to be the standard for similar research front. This section, thus, is kept limited to $LaAlO_3$/ $SrTiO_3$, primarily.

1.3 Origin of conductive interface

At this point of the discussion, the natural question is what mechanism results in such electronic reconstruction that leads to a conductive interface. The growth conditions like temperature and pressure immensely control the interface property. The variation in these conditions not only can reconstruct the $SrTiO_3$ surface or develop strain in the deposited $LaAlO_3$ films but also can produce defects (vacancy, doping etc.) at the interface. Such modifications also could lead to a conductive interface.

The dependence of the interfacial properties on growth conditions is prominent in the works discussed earlier. The growth condition maintained by Ohtomo et al. [1] was to hold the oxygen partial pressure, p_{O_2}, at 10^{-4}-10^{-6} torr and the temperature at 800°C, followed by a cool down at same p_{O_2}. In case of thinner $LaAlO_3$ layers, the interface developed at 10^{-6} torr showed metallic behaviour down to 2K from room temperature, whereas interfaces formed at higher pressure values were found to have an insulating behaviour even at low temperatures. Annealing the as-grown sample in 1-atmosphere pressure at 400°C for 2 hours during cool down slightly altered the transport properties. However, high-temperature annealing dramatically decreased the conductivity, which, as suggested by the authors, might be a result of La/ Sr interdiffusion.

Thiel et al. had slightly different protocols for the sample preparation [3]. They have deposited $LaAlO_3$ on $SrTiO_3$ in $p_{O_2} \approx 2 \times 10^{-5}$ mbar at 770°C or at 815°C. Although the growth condition was almost similar to that followed by Ohtomo et al., the cool-down process was different. The as-grown samples were cooled down to room temperature in $p_{O_2} \approx 400$ mbar in 2.5 hours which also included oxidation for an hour at 600°C. The carrier mobility of the conducting interface was found to be ~ 1200 cm^{2}V^{-1}s^{-1} which was almost an order of magnitude lower than that achieved by Ohtomo et al.

Although the origin of a conducting layer at Perovskite Oxide insulator junctions is debatable, it is believed that there are basically three phenomena that explain the emergence of conductivity which are discussed in the following.

1.3.1 Polar catastrophe

This simplistic model relies on the formation of potential across [001] $LaAlO_3$ layer [10]. The magnitude of the potential depends upon the number of unit cells of $LaAlO_3$ along [001]. At a certain thickness (4 unit cells) of the $LaAlO_3$, the built-up potential is high enough to facilitate charge transfer from the surface to the interface in order to avoid polar catastrophe (refer to Fig. 1.2). This excess charge is accepted by Ti *d* orbitals at the surface of $SrTiO_3$ substrate lowering the oxidation state of Ti from +4 towards +3. Ohtomo et al. [1] also proposed this mechanism to be the primary factor that results in the presence of mobile electrons at the interface. This mechanism also supports the critical thickness phenomenon observed by Thiel et al. [3].

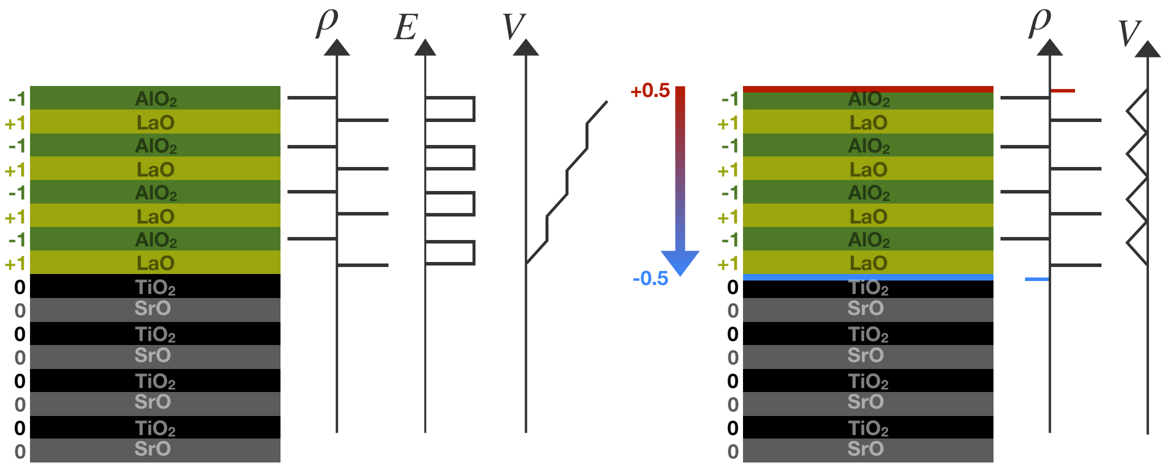

Fig. 1.2 Graphic representation of the polar catastrophe mechanism. As can be seen, the potential builds up across $LaAlO_3$ due to the stacking of +1 and -1 charged layers in an alternating fashion. To avoid such polar catastrophe, -0.5 charge migrates to the interface, leaving +0.5 charge on the $LaAlO_3$ surface behind, and the effective potential across $LaAlO_3$ becomes zero.

It should also be noted that in polar single crystals, such kind of polar catastrophe is neutralized by atomic reconstruction of the surface, surface absorption of charged contamination, electronic reconstruction of the surface etc. In contrast to bulk, surfaces/ interfaces usually have different atomic or electronic configurations and are more active. Thus a surface/ interface is vulnerable to reconfiguration/ reconstruction. Fig. 1.2 also shows that the proposed mechanism only affects the surface and interface. During the growth of such polar and non-polar interfaces, what kind of surface-interface reconfiguration/ reconstruction should be dominant is entirely decided by the energy cost of the process, which is also somewhat controlled by growth parameters.

1.3.2 Oxygen vacancy doping

It was also reported [11; 12], $SrTiO_{3-x}$ is conducting. Oxygen vacancy in TiO_2 layers in $SrTiO_3$ substrate during growth could also appear if the oxygen partial pressure is kept very low. Such vacancy could diffuse through the whole $SrTiO_3$ substrate resulting in a lower oxidation state of Ti at different sites within the crystal. Additionally, Al has a very high affinity to O, which may also be responsible for oxygen vacancy at the interface. Herranz et al. in 2007 investigated [13] the metallicity in $LaAlO_3$/ $SrTiO_3$ in an exciting way. They have grown the sample in a similar growth protocol followed by Ohtomo et al. [1] to obtain similar carrier density and mobility. Analyzing the Shubnikov-de Haas (SDH) oscillation data with the Onsager formula, $F_{SDH} = \hbar A_{ext}/2\pi e$ (where F_{SDH} and A_{ext} are SDH oscillation frequency along magnetic field axis and area of extremal orbit in k space, perpendicular to the applied magnetic field direction and the rest of the symbols have conventional meanings), they have discovered that A_{ext} is independent of the direction of the applied magnetic field. The estimated thickness of the conducting layer was comparable to $SrTiO_3$ substrate thickness. Conductivity persisted upon removal of the $LaAlO_3$ layer along with a few monolayers of $SrTiO_3$. By altering the growth parameters with high oxygen pressure, they found that the interface becomes insulating. All these observations suggested that the conductivity is not only bulk in nature but also due to oxygen vacancy doping.

1.3.3 Cation intermixing

Substitution of Sr^{2+} with La^{3+} [14; 15] or Ti^{4+} with Al^{3+} [16] during the growth could also result in n-type and p-type interfaces, respectively. The dominant mechanism responsible for the origin of the conductivity strongly depends upon the growth condition. Basletic et al. in 2008 carried out cross-sectional imaging across the $LaAlO_3$/$SrTiO_3$ interfaces prepared at different conditions to map the spatial charge carrier distribution with the conductive tip atomic force microscopy (CT-AFM) method [17]. Their observation revealed that an interface developed at the condition followed by Ohtomo et al. exhibited high conductivity at the interface and saturated at a value of around 4 orders of magnitude lower inside the $SrTiO_3$ substrate, whereas $LaAlO_3$ side remained highly insulating. On the other hand, for an interface grown with a protocol similar to that by Thiel et al. [3], the conductivity was only observed at the interface. Although, in both cases, conductivity at the interface had similar order of magnitude, in the latter case, the spatial distribution of the carrier was limited to a few nano-meters along the [001] direction. The authors concluded that for the latter case, since the growth process is followed by cool down at high oxygen pressure the contribution of oxygen vacancy doping to the conductivity could practically be ruled out. In this case, the origin of conductivity could primarily be a polar catastrophe and cation intermixing. Also, the measured carrier density was close to (but a little higher than) the estimated value if the primary mechanism responsible for the conductivity was assumed to be a polar catastrophe. The excess carrier density could be attributed to cation intermixing. Today the consensus is that the origin of the conductivity in $LaAlO_3$/ $SrTiO_3$ interfaces is owed to all the mechanisms mentioned above. However, their relative contribution depends upon preparation protocols.

It has also been observed that interfaces prepared for other crystallographic orientations of $SrTiO_3$ [18] are also conducting, and similar mechanisms as we have discussed can also explain those conductive interfaces. However, our discussion for this thesis is primarily limited to [001] orientation.

1.4 Superconductivity at insulating oxide interfaces

Reyren et al. in 2007 reported that the $LaAlO_3$/$SrTiO_3$ [001] interfaces undergo superconducting transition around a temperature of the order of 100 mK [19]. Later, Biscaras et. al also observed superconductivity in $LaTiO_3$/ $SrTiO_3$ [001] interfaces [20]. Coherence length, ξ could be speculated from the clean limit relationship, $H_{C_2} = \frac{\phi_0}{2\pi\xi^2}$, where H_{C_2} and ϕ_0 are measured upper critical field and magnetic flux quanta respectively. For both cases, it was confirmed that $\xi >$ the thickness of the conducting layer, which indicates that the superconducting phases observed were low dimensional.

Low dimensional superconductivity emerging at insulating oxide interfaces has potential application in superconducting nanoelectronics. Additionally, such superconductivity, being confined between complex oxides, may appear with certain unconventional features, inexplicable within the limit of the BCS (Bardeen-Cooper-Schrieffer) framework. These superconducting states, thus, besides their prospect in MOSFET-like devices with gate tunability, are also very interesting in terms of their superconducting characteristics. We shall discuss superconductivity more in later chapters.

Electronic states residing at the interfaces of the insulating materials could be controlled by an external electric field. This method is called gating, where applying a DC voltage to a special electrode reflects as an electric field at the region of interest in the device under test. The applied DC voltage is called gate voltage. Gating could affect an interface in versatile ways like modulating the carrier density, tuning the disorders etc. However, which factor should dominantly control the interface depends upon the system itself.

Thiel et al., in their work, also reported that $LaAlO_3$/ $SrTiO_3$ [001] interfaces have significant sensitivity to gating [3]. They also observed that even the interfaces developed for $LaAlO_3$ thickness less than the critical thickness conduct under the influence of a high gate voltage (of the order of 100 V). Caviglia et al. demonstrated that the superconducting phase at $LaAlO_3$/ $SrTiO_3$ [001] interface could be efficiently modulated by gating [21]. The superconducting transition temperature, T_C, varies with gate voltage. This effect owes to the systematic change in the carrier density at the interface with gating. The approximate modulated carrier density, δn, could be estimated by considering the system as a simple parallel plate capacitor with the interface and gate electrode being the plates and the $SrTiO_3$ substrate being the dielectric: $\delta n \approx \varepsilon_0 \varepsilon_r V_G / et$, where ε_0, ε_r, V_G, e and t are vacuum permittivity, the dielectric constant of $SrTiO_3$, applied gate voltage, charge of the electron and the thickness of the $SrTiO_3$ substrate, respectively. This estimation of carrier density sits quite right with measured carrier density by conventional Hall measurement. The interface could undergo a transition from an under-doped to an over-doped regime in terms of carrier density in the application of gate voltage. While doing so, the T_C also changes accordingly. The authors demonstrated that T_C/ T_{BTK} vs gate voltage (V) acquires a dome-type shape indicating the under-doped regime for negative gate voltage where T_C drops drastically with increasing gate voltage (magnitude) and the over-doped regime for positive gate voltage where again T_C drops gradually with increasing gate voltage.

Although gating can tune the carrier density at the interface, it can also modulate other properties unrelated to the carrier density. Recently, Cheng et al. reported that for $LaAlO_3$/ $KTaO_3$ [111] interface, gating could control the disorder more effectively than the carrier density [22]. The interface is superconducting below 2K, and the T_C vs gate voltage also appears as a dome-shaped curve. But unlike $LaAlO_3$/ $SrTiO_3$ [001], the carrier density, as extracted from Hall measurement, does not change appreciably with the gate. Also, towards negative gate voltage, the resistance saturates to a non-zero value below the transition. The saturation value increases with increasing the negative gate voltage. This indicates that the carrier mobility changes with gate voltage instead of carrier density. This observation suggests that the disorder at the interface can be tuned with gating.

1.5 Conclusion

The conductive interfaces of insulating Perovskite oxide materials are the potential playground for novel quantum phenomena. The low dimensional nature of conductivity coexisting with the versatile characteristics like magnetism, ferroelectricity or spin-orbit interaction offered by Perovskite oxide materials is of immense importance not only in application but also in understanding basic quantum phenomena. Such conductive interfaces are very sensitive to electric fields (gating) in different ways, which makes them suitable for nanoelectronics applications. Low dimensional superconductivity in these materials is also very interesting. They have a high possibility of appearing with some unconventionality and are easily controlled by gate voltage as well. All in all, the Perovskite oxide interfaces are a very promising hunting ground for novel physical phenomena.

Chapter 2

Microscopic understanding of superconductivity

2.1 Introduction

Superconductivity is characterized mainly by two macroscopic effects: zero electrical resistivity and perfect diamagnetism. The presence of perfect diamagnetism distinguishes the superconducting phase from a perfect conductor. Theoretically, both of these macroscopic features are satisfied by a single equation.

$$j_S \propto -\frac{1}{\mu_0 \lambda_L^2} A, \tag{2.1}$$

where j_S is super current density, A is vector potential, μ_0 is vacuum permeability, and λ_L is known as London penetration depth. This equation is famous Londons' equations in a concise form. The equation (2.1) also suggests that the magnetic field strength inside a superconductor falls off exponentially as $e^{-\frac{x}{\lambda_L}}$. λ_L can be considered as a length scale for a superconductor.

After realizing the liquefaction process for He^4 in 1909, Kammerling Onnes in 1911 discovered superconductivity in mercury. It was observed that the resistivity of the mercury underwent a sharp drop down to zero at 4.2 K. This indicated that the sudden fall in the resistivity should be associated with some phase transition. This transition from a metallic non-zero resistance state to a zero resistance state is called a superconducting phase transition. The temperature at which such phase transition occurs is known as transition temperature, T_C. Henceforth, we shall call the metallic state, a normal state.

Superconductor to normal state transition can be achieved by tuning different environmental parameters. Temperature and magnetic field are two important parameters in that regard. By raising the temperature or by increasing the magnetic field a superconducting state can be altered to a normal state. The magnetic field required to destroy superconductivity is called the critical field, H_C. The typical $H_C - T_C$ phase diagram is shown in Fig.2.1. Since the superconducting state exhibits perfect diamagnetism, the magnetic moment, M and the applied magnetic field, H are related by $M = -H$. Now, if we consider that at temperature, T, in the superconducting state, the magnetic field is swept gradually from 0 to $H_C(T)$, for any intermediate field H, the energy added to the system is

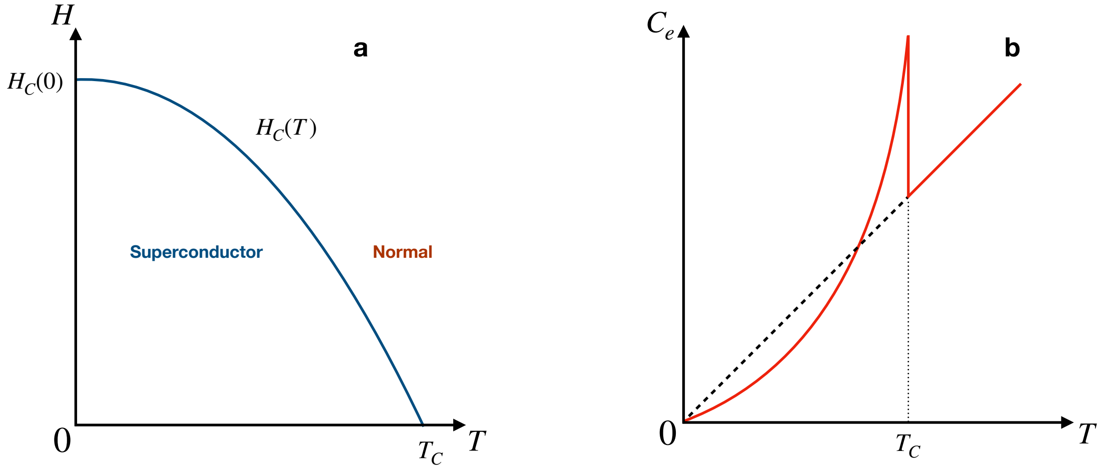

Fig. 2.1 **a** $H_C - T_C$ phase diagram of a superconductor. **b** electronic heat capacity vs temperature graph shows a finite jump at T_C

$$-\mu_0 \int_0^H M \cdot dH = -\mu_0 \int_0^H (-H) \cdot dH = \mu_0 \frac{H^2}{2}. \tag{2.2}$$

The difference in the Gibb's free energy between the normal state (G_N) and the superconducting state (G_S) at any temperature T below T_C is, thus, given by,

$$G_N - G_S = \mu_0 \frac{H_C(T)^2}{2}. \tag{2.3}$$

The difference in entropy between the normal state (S_N) and the superconducting state (S_S) can be obtained by taking the derivative of equation (2.3) with respect to T,

$$S_N - S_S = \mu_0 H_C(T) \frac{dH_C(T)}{dT}. \tag{2.4}$$

Equation (2.4) suggests that for any temperature, $T < T_C$ at the point $(T, H_C(T))$ the energy added to the system would contribute to the disorder only, i.e., by acquiring energy, the system would undergo a phase transition from the ordered superconducting state to disordered normal state. This idea is similar to that of latent heat. Thus, in the presence of a magnetic field, the superconducting phase transition is a first-order phase transition. For $T = T_C$ we can see that $H_C = 0$ (Fig. 2.1), which makes the right hand side of the equation (2.4) zero. This means at $T = T_C$, the superconducting transition is not a first-order phase transition. One can calculate the electronic heat capacity, C_e at $T = T_C$ by taking the derivative of equation (2.4). With a simple calculation, it can be shown that at $T = T_C$, there is a finite discontinuity in C_e between the normal state and superconducting state (Fig. 2.1 b) which suggests that the superconducting phase transition at $T = T_C$ is a second order phase transition.

The existence of a zero resistance state could be understood microscopically. It was observed by flux quantization measurements in 1961 that for a superconductor, carrier charge is $2e$, where e is the charge of a single electron. The finite resistance in a metal persists even at absolute zero temperature due to the scattering of electrons from defects. However, the scattering mechanisms for Fermions that give rise to resistance are not valid for Bosons. One can assume that in case of superconductivity the electrons pair in a new Boson-like state protected from scattering. These electron pairs are called Cooper pairs. The pairing of electrons in a superconductor is a complicated mechanism. All the Cooper pairs in a superconductor are highly correlated and collectively create a global quantum state. In this complex Bosonic system, the minimum excitation energy required to break one Cooper pair to a Fermionic state is the same for destroying all cooper pairs. This cooper pair breaking energy is $\mu_0 \frac{H_C^2}{2}$ as we have calculated in the last section. This required energy is huge and cannot be supplied by scattering mechanisms that cause resistivity for Fermions in a typical metal state. Thus the Coopper pairs move through the system ignoring the defects and consequently causing a zero resistance state [24]. The mechanism that allows such pairing is coherent electron-phonon interaction, where a phonon created by one electron of the pair is absorbed by the other electron. The possibility of such interaction is evident if we look at the Bloch wave function, which is,

$$\psi_{nk} = \exp^{ik\cdot r} u_{nk}(r). \tag{2.5}$$

In equation (2.5) k is crystal momentum and n is band index. k is a good quantum number for ψ_{nk}. Since k is crystal momentum, the lattice vibration that generates the phonons is also quantized in the same k values. Thus, whenever an electron absorbs or releases a phonon, it can transit into available k states. As the vibration of the lattice is involved in superconductivity, naturally, the phonon frequency is limited by Debye frequency ω_D. This concludes that electron-phonon interaction is also limited by ω_D in superconductivity. The quantum mechanical model of superconductivity was first realized by Bardeen, Cooper and Schrieffer in 1957. Their work is also known as the famous BCS theory [23].

2.2 Second quantization

Superconductivity is a complex state of matter which involves many particles, and to theoretically deal with such systems, the convenient approach is via second quantization. In the second quantization, a many-particle basis is constructed by taking a linear combination (summation) of the product of orthonormal single-particle states. The coefficients of the product states inside the summation are chosen to satisfy the symmetry of the particle, i.e., the coefficients allow a defined many-particle Bosonic state to be symmetric and a Fermionic state to be antisymmetric.

A N particle Bosonic state with a defined occupation number for each state is represented by,

$$\phi^B_{\nu_1,\nu_2...\nu_N} = \frac{1}{\prod_\mu \sqrt{n_\mu!}\sqrt{N!}} \sum_P \phi_{\nu_1}[P(1)]\phi_{\nu_2}[P(2)]...\phi_{\nu_N}[P(N)]. \tag{2.6}$$

Here $\phi_{\nu_1}, \phi_{\nu_2}, ...\phi_{\nu_N}$ are orthonormal single particle states from a complete set with quantum numbers $\nu_1, \nu_2, ...\nu_N$ respectively. $P(1), P(2), ...P(N)$ are permutations of $1, 2, ...N$. n_μ is the number of times the state ν_μ appears in the product. ϕ^B is normalized by the factor before the summation.

Similarly, a N particle Fermionic state with a defined occupation number for each state is represented by:

$$\phi^F_{\nu_1,\nu_2...\nu_N} = \frac{1}{\sqrt{N!}} \sum_P (-1)^P \phi_{\nu_1}[P(1)]\phi_{\nu_2}[P(2)]...\phi_{\nu_N}[P(N)]. \tag{2.7}$$

Here the factor $(-1)^P$ makes the Fermionic state anti-symmetric.

Creation and annihilation operators for many body states could be defined, which transform any N particle state to $N+1$ or $N-1$ particle state, respectively, depending on the availability of the states for the transformation. For a fully occupied state and a completely unoccupied state, the creation and annihilation operation, respectively, should result in zero. Any Hamiltonian can be written in terms of creation and annihilation operators. To do that, the operators should be defined in a way that satisfies the symmetry of the Bosonic and Fermionic states. A many-particle state could be written in occupation number representation, $|n_1 n_2, ...n_K\rangle$ where $1, 2, ...K$ are the indices of single particle orthonormal quantum states $\nu_1, \nu_2 ...\nu_K$ and $n_1, n_2, ...n_K$ are their respective occupation numbers. For Fermions, the occupation number is either 0 or 1. Here, $n_1 + n_2 + ...n_K = N$ where N is total number of particles. Also, $\langle n'_1 n'_2 ...n'_K | n_1 n_2 ...n_K \rangle = \delta_{n'_1 n_1, n'_2 n_2, ...n'_K n_K}$. In the occupation number representation, the symmetry information is lost, but that information is also not required since the symmetry information is already incorporated in the creation and annihilation operators. The gist of the second quantization algebra is given below,

Bosons:

$$[b_\nu, b_{\nu'}] = [b^\dagger_\nu, b^\dagger_{\nu'}] = 0 \tag{2.8}$$

$$[b_\nu, b^\dagger_{\nu'}] = \delta_{\nu\nu'} \tag{2.9}$$

$$b^\dagger_\nu |n_1 ...n_\nu ...\rangle = \sqrt{n_\nu + 1} |n_1 ...n_\nu + 1...\rangle \tag{2.10}$$

$$b_\nu |n_1 ...n_\nu ...\rangle = \sqrt{n_\nu} |n_1 ...n_\nu - 1...\rangle \tag{2.11}$$

Fermions:

$$\{c_\nu, c_{\nu'}\} = \{c^\dagger_\nu, c^\dagger_{\nu'}\} = 0 \tag{2.12}$$

$$\{c_\nu, c^\dagger_{\nu'}\} = \delta_{\nu\nu'} \tag{2.13}$$

$$c^\dagger_\nu |n_1 ...n_\nu ...\rangle = (-1)^{n_1 + n_2 + ... + n_{\nu-1}} (1 - n_\nu) |n_1 ...n_\nu + 1...\rangle \tag{2.14}$$

$$c_\nu |n_1 ...n_\nu ...\rangle = (-1)^{n_1 + n_2 + ... + n_{\nu-1}} n_\nu |n_1 ...n_\nu - 1...\rangle \tag{2.15}$$

Here $b^\dagger_\nu$ and $c^\dagger_\nu$ create a particle in the state ν; b_ν and c_ν annihilate a particle from state ν. In the second quantization formalism a one body operator for a N particle state, $\hat{H}_0 = \sum_{i=1}^{n} \hat{h(i)}$ can be represented as,

$$\hat{H}_0 = \sum_{\nu\nu'} \langle \nu | \hat{h} | \nu' \rangle a^\dagger_\nu a_\nu = \sum_{\nu\nu'} h_{\nu\nu'} a^\dagger_\nu a_\nu \tag{2.16}$$

and a two body operator for N particle state, $\hat{H}_I = \frac{1}{2} \sum_{\substack{i,j=1 \\ i \neq j}}^{n} \hat{v}(i,j)$ can be represented as,

$$\hat{H}_I = \frac{1}{2} \sum k,l,m,n \langle kl | \hat{v} | mn \rangle a^\dagger_k a^\dagger_l a_n a_m = \frac{1}{2} \sum_{k,l,m,n} v_{klmn} a^\dagger_k a^\dagger_l a_n a_m \tag{2.17}$$

where operators $a, a^\dagger$ should be replaced by respective Fermionic or Bosonic operators depending upon the symmetry of the chosen system. Another important operator is the number operator, $\hat{N}_\nu$, upon operation on a many-particle state, it gives the number of particles in a state ν,

$$\hat{N}_\nu = a_\nu^\dagger a_\nu \tag{2.18}$$

$$\hat{N}_\nu |n_1 ... n_\nu ...\rangle = n_\nu |n_1 ... n_\nu ...\rangle$$

Many particle states are usually eigenfunctions of $\hat{N}_\nu$ unless the system is considered to be grand canonical. In such cases, the state is a linear combination of eigenstates of $\hat{N}_\nu$. BCS theory is based on a grand canonical system where the number of particles is not conserved.

2.3 Bardeen, Cooper and Schrieffer (BCS) theory

As discussed in the introduction, superconductivity emerges through electron pairing, and the pairing happens via electron-phonon interaction. When an electron moves through a lattice, it creates polarization in the medium by attracting the ion cores. This polarization created by such interaction attracts the second electron. If the attraction potential is significant enough to override the Coulomb repulsion between two electrons, a bound state of two electrons is created. The importance of lattice-electron interaction in superconductivity was realized by Fröhlich in 1950. However, Cooper 1965 devised a model to estimate the attractive potential magnitude. This is known as the famous Cooper problem. In this model, he added two electrons above a filled Fermi sea and calculated the effective, attractive potential required to attain a bound state between them. The two electrons can interact with each other by phonon exchange and transit to other available states but not with the electrons in the Fermi sea as they are already occupied.

For a superconductor, a pair of electrons $|k, k'\rangle$ with an exchange of a phonon of momentum q becomes $|k+q, k'-q\rangle$ as shown in Fig. 2.2. This process should be elastic since for superconductivity there is no energy loss, the total momentum $K = k + k'$ is conserved. If two electrons above the Fermi surface create a bound state by phonon exchange, their energy must be limited by Debye frequency ω_D. For a metal, $\omega_D \ll E_F$, where E_F is the energy at the Fermi surface. In Fig. 2.3, two Fermi spheres are drawn for two such electrons where Δk is the range (limited by ω_D) within which such electrons can exist. However, the shaded regions are the ones where the $K = k + k'$ condition is followed. Thus, the shaded regions represent the allowed states for pairing. And it is evident that for $K = 0$, the number of states is maximum. Thus, in superconductivity, a pair of electrons with $K = 0$ or $k = -k'$ have the maximum contribution. This pair $|k, -k\rangle$, can access all the states within Δk by

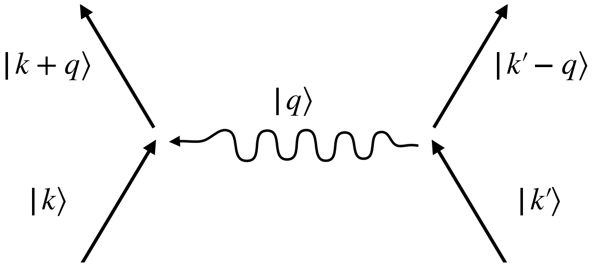

Fig. 2.2 Diagram of a phonon exchange process between two electrons with momentum k and k'

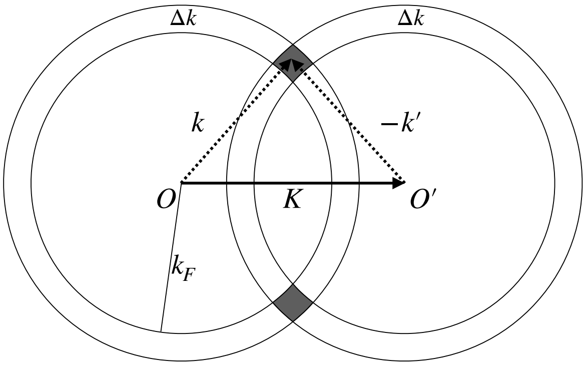

Fig. 2.3 Two Fermi spheres with radii k_F is drawn at O and O' to represent the available states for each electron.

electron-phonon interaction and the wave function, $\psi(r_1,\sigma_1,r_2\sigma_2)$ for such two electrons can be written as a linear combination of all such k states where σ is the spin quantum number, and r is the particle coordinate,

$$\psi(r_1,\sigma_1,r_2\sigma_2) = \sum_k g(k)\frac{1}{\Omega}e^{ik.(r_1-r_2)}\chi(\sigma_1,\sigma_2). \tag{2.19}$$

Here Ω is the volume of the system, and χ is the spin function. $g(k)$ could be obtained by solving the Schrödinger's equation. For ψ to be antisymmetric, either the spatial part should be antisymmetric (symmetric) and the spin function should be symmetric (antisymmetric). However, the spatial part being symmetric means maxima at $r_1 - r_2 = 0$, which is a requirement for a bound state. Thus the spin part must be antisymmetric. Cooper started with a wave function of the form in equation (2.19) with the spin function being antisymmetric and solved the Schrödinger's equation for a constant attractive potential V_0. By choosing the magnitude of the energy of each of the two electrons with respect to Fermi energy, E_F, within the scale, $\hbar\omega_D$, to limit the accessible states in the ΔK, the energy E of the pair in weak coupling approximation ($\rho(E_F)V_0 \ll 1$) can be estimated to

$$E \simeq 2E_F - 2\hbar\omega_D e^{-\frac{2}{V_0\rho(E_F)}} \tag{2.20}$$

where ρ is the density of states. For the calculation, ρ could be approximated to a constant $\rho(E_F)$, the density at the Fermi surface, since $\hbar\omega_D \ll E_F$. The Cooper problem has the following significant conclusions [25],

1. in the presence of a filled Fermi sea as a background, two electrons could form a bound state in an attractive potential, regardless of how weak the magnitude of the potential is.

2. The energy, E, of the bound state is not an analytic function of V_0 for $V_0 \to 0$. The energy cannot be calculated by perturbation theory.

3. The binding energy of the Cooper pair increases as V_0 increases. Stronger electron-phonon interaction means larger binding energy.

4. The binding energy also increases with the density of states at Fermi energy.

Although the Cooper problem explains the nature of the pairing and the pairing requirements, this essentially is a two-body problem. For a real system, one needs to consider all the electrons that form Cooper pairs. Cooper's problem already suggested that a filled Fermi sea of electrons is unstable against the formation of at least one bound pair, and one may expect that Cooper pairs keep on condensing until a stable equilibrium is reached. To deal with such complex many-body problems, Bardeen, Cooper, and Schrieffer constructed a Hamiltonian, H_{BCS} of the following form,

$$H_{BCS} = \sum_{k\sigma} \varepsilon_k c^{\dagger}_{k\sigma} c_{k\sigma} + \sum_{kk'} U_{kk'} c^{\dagger}_{k'\uparrow} c^{\dagger}_{-k'\downarrow} c_{-k\downarrow} c_{k\uparrow} \tag{2.21}$$

where ε_k is the energy of each electron, $U_{kk'}$ is the matrix element of attractive potential. As mentioned earlier, antisymmetry to a two-electron state is incorporated in the spin function, which means that the electrons are paired in a singlet state. Thus, $|k\uparrow, k\downarrow\rangle$ should represent one cooper pair where $\uparrow$ and $\downarrow$ represent up spin and down spin, respectively. By electron-phonon interaction $|k\uparrow, k\downarrow\rangle$ can be scattered to $|k'\uparrow, k'\downarrow\rangle$. The second term of the equation (2.21) takes care of all such interactions, whereas the first term represents the total kinetic energy of all the particles. The many-particle wave function will have the form of multiplication of $|k\uparrow, k\downarrow\rangle$ states for all the pairs (k will be different for different pairs) and summation over all such multiplications. Thus, the BCS ground state trial wave function, $|\psi_G\rangle$, is chosen as,

$$|\psi_G\rangle = \prod_k (u_k + v_k c^\dagger_{k\uparrow} c^\dagger_{-k\downarrow})|0\rangle \tag{2.22}$$

where $|0\rangle$ is the vacuum state. $|u_k|^2$ and $|v_k|^2$ are the probability amplitude of $|k\uparrow, k\downarrow\rangle$ state is unoccupied and occupied respectively.

$$|u_k|^2 + |v_k|^2 = 1 \tag{2.23}$$

One can readily observe that $|\psi_G\rangle$ is not an eigen function of the occupation number:

$$\hat{N} = \sum_{k\sigma} \hat{N_{k\sigma}} = \sum_{k\sigma} c^\dagger_{k\sigma} c_{k\sigma}. \tag{2.24}$$

This is because the system chosen here is grand canonical, where the Fermi sphere is considered as the bath, which is much much larger than the system made of Cooper pairs. So the effective Hamiltonian, $\bar{H}_{BCS}$ is,

$$\bar{H}_{BCS} = H - \mu\hat{N} = \sum_k \bar{\varepsilon}_k (c^\dagger_{k\uparrow} c_{k\uparrow} + c^\dagger_{-k\downarrow} c_{-k\downarrow}) + \sum_{kk'} U_{kk'} c^\dagger_{k'\uparrow} c^\dagger_{-k'\downarrow} c_{-k\downarrow} c_{k\uparrow} \tag{2.25}$$

where μ is chemical potential and $\bar{\varepsilon}_k = \varepsilon_k - \mu$. μ is nothing but the Fermi energy E_F and $\bar{\varepsilon}_k$ is the energy with respect to the Fermi surface. By taking

$$u_k = cos\theta_k, \qquad v_k = sin\theta_k \tag{2.26}$$

and minimizing the energy, $\bar{E} = \langle\psi_G|\bar{H}_{BCS}|\psi_G\rangle$, for θ_k one can find,

$$u_k^2 = \frac{1}{2}\left[1 + \frac{\bar{\varepsilon}_k}{\sqrt{\bar{\varepsilon}_k{}^2 + \Delta_k{}^2}}\right], \qquad v_k^2 = \frac{1}{2}\left[1 - \frac{\bar{\varepsilon}_k}{\sqrt{\bar{\varepsilon}_k{}^2 + \Delta_k{}^2}}\right] \tag{2.27}$$

where

$$\Delta_k = -\sum_{k'} U_{kk'} u_{k'} v_{k'} = -\frac{1}{2}\sum_{k'} U_{kk'} \frac{\Delta_{k'}}{\sqrt{\bar{\varepsilon}_{k'}{}^2 + \Delta_{k'}{}^2}}. \tag{2.28}$$

By invoking the BCS approximation, which is,

$$U_{kk'} = \begin{cases} -U_0 & |\bar{\varepsilon}_k| < \hbar\omega_D \\ 0 & \text{Otherwise} \end{cases} \tag{2.29}$$

Δ_k becomes a constant, Δ_0. The BCS approximation also limits the energy, $|\bar{\varepsilon}_k|$, by $\hbar\omega_D$. The v_k^2 vs $\bar{\varepsilon}_k$ graph at absolute zero temperature is shown in Fig. 2.4 **b**, which suggests that in the case of superconductivity, states with occupation probability 1 or 0 in terms of energy are far from E_F and do not participate in the superconductivity. Also, from Fig. 2.4 **b**, it is evident that the Fermi surface cannot be defined for a superconductor. Cooper pairs condensate near E_F, and consequently, occupation probability becomes smeared around E_F, indicating that about E_F now also unoccupied states with probability u_k^2 are created, which electrons of the Cooper pairs from the occupied states can avail after electron-phonon interactions. In weak coupling limit, the following expressions for Δ_0 and $\bar{E_S}$ (energy of the ground state with respect to E_F) are in order,

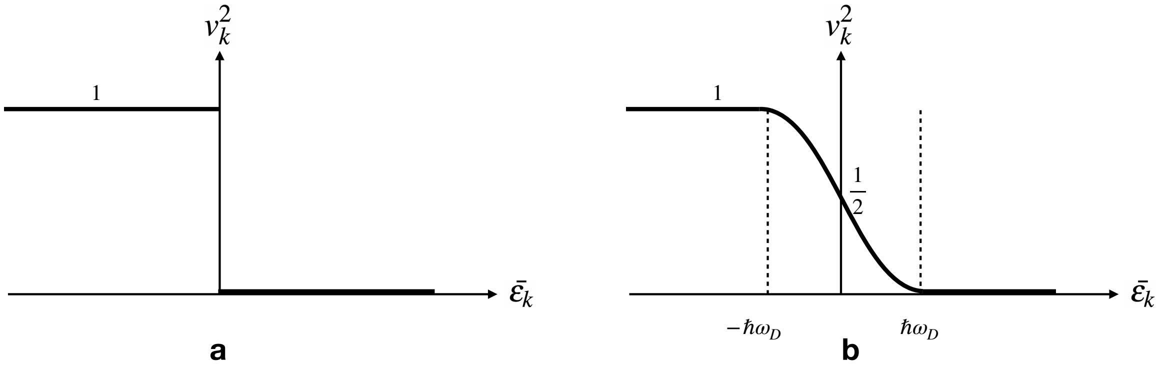

Fig. 2.4 Plot of v_k^2 vs $\bar{\varepsilon}_k$ at absolute zero temperature **a** for normal metal, **b** for superconductor.

$$\Delta_0 \simeq 2\hbar\omega_D exp\left[\frac{-1}{U_0\rho(E_F)}\right] \tag{2.30}$$

$$\bar{E_S} \simeq \bar{E_N} - \frac{1}{2}\rho(E_F)\Delta_0^2 \tag{2.31}$$

where $\bar{E_N}$ is the normal state energy with respect to E_F. Equation (2.31) immediately suggests that the energy of the superconducting state is lower than the normal state, which is why the superconducting transition occurs to minimize the system's energy. Δ_0 is the energy gap parameter. From the equation (2.30), it can be conjectured that Δ_0 becomes larger with increasing ω_D, attractive interaction, and density of states at Fermi energy and consequently, the superconducting state becomes stronger (the ground state energy is lowered), which is also evident from the equation (2.31).

To calculate the excited states, $\bar{H}_{BCS}$ needs to be diagonalized. In order to do that mean field decoupling of the last term in the expression of $\bar{H}_{BCS}$ (equation (2.25)) is required. We already know, electron-phonon interaction should scatter a state, $|k\uparrow, k\downarrow\rangle$ to some other state, $|k' \uparrow, k' \downarrow\rangle$. This means, creating a state at $|k' \uparrow, k' \downarrow\rangle$ depends upon the expectation value of $|k \uparrow, k \downarrow\rangle$ state being destroyed and destroying a state $|k \uparrow, k \downarrow\rangle$ also depends upon the expectation value of $|k' \uparrow, k' \downarrow\rangle$ state being created. So the last term in equation (2.25) can be written in a form like $\sum_k \Delta_k^* c_{-k\downarrow} c_{k\uparrow} - \sum_k \Delta_k c_{k\uparrow}^\dagger c_{-k\downarrow}^\dagger$. After ignoring the higher order fluctuation terms, the exact mean-field calculation gives a transformed Hamiltonian, H_{MF},

$$H_{MF} = \sum_{k\sigma} \bar{\varepsilon}_k c_{k\sigma}^\dagger c_{k\sigma} - \sum_k \Delta_k^* c_{-k\downarrow} c_{k\uparrow} - \sum_k \Delta_k c_{k\uparrow}^\dagger c_{-k\downarrow}^\dagger + \sum_k \Delta_k \langle c_{k\uparrow}^\dagger c_{-k\downarrow}^\dagger \rangle \tag{2.32}$$

where $\Delta_k = -\sum_{k'} U_{kk'} \langle c_{-k',\downarrow} c_{k'_\uparrow} \rangle$. By the following canonical transformation, also known as the Bogoliubov transformation:

$$\gamma_{k\uparrow} = u_k c_{k\uparrow} - v_k c_{-k\downarrow}^\dagger, \qquad \gamma_{-k\downarrow} = u_k c_{-k\downarrow} + v_k c_{k\uparrow}^\dagger \tag{2.33}$$

the Hamiltonian H_{MF} is diagonalized to:

$$H_{MF} = \sum_k E_K (\gamma_{k\uparrow}^\dagger \gamma_{k\uparrow} + \gamma_{-k\downarrow}^\dagger \gamma_{-k\downarrow}) \tag{2.34}$$

where $E_k = \sqrt{\bar{\varepsilon}_k{}^2 + \Delta_k^2}$ represents single particle excitation energy. Bogoliubov transformation introduces new Fermionic creation, and annihilation operators, $\gamma_k^\dagger$ and γ_k, respectively and the corresponding quasiparticles are called Bogoliubons. With a similar approximation as is done before, Δ_k can be treated as a constant, Δ_0, and the expression for excitation energy becomes:

$$E_k = \sqrt{\bar{\varepsilon}_k{}^2 + \Delta_0^2} \tag{2.35}$$

Equation (2.35) suggests that excitation to a normal state from superconducting state requires an additional energy Δ_0. The density of single-particle states ρ_S for superconductors can also be calculated from equation (2.35).

$$\rho_S(E) = \begin{cases} \rho(E_F) \frac{E}{\sqrt{E^2 - \Delta_0^2}} & E > \Delta_0 \\ 0 & \text{Otherwise.} \end{cases} \tag{2.36}$$

Equation (2.36) also suggests that in a superconductor, a gap of $2\Delta_0$ opens up at the Fermi level, where there cannot be any single-particle states. At $E = \pm\Delta_0$ the single-particle density of states diverges and far from E_F it becomes constant ($\rho_S(E) = \rho(E_F)$). Since, $\Delta_0 = 0$ beyond $\hbar\omega_D$, $\rho_S(E)$ becomes flat before $\hbar\omega_D$. From this, one may also conclude that the gap parameter, $\Delta_0 < \hbar\omega_D$.

BCS theory not only successfully describes the microscopic phenomena that allow superconductivity, but macroscopic characteristics of a superconductor, like zero resistivity, perfect diamagnetism, penetration depth etc., can also be explained. BCS theory, thus, is a complete theory for the primary understanding of superconductivity that originates from electron-phonon interactions.

2.4 Types of superconductors

In the introduction, we came across a length scale parameter, λ_L, the London penetration depth. There exists another length scale parameter, ξ, called the coherence length. ξ, in a way, represents the average size of the Cooper pairs. ξ can also be calculated from the BCS theory. A ratio $\kappa = \frac{\lambda_L}{\xi}$ can be defined. κ is called the Ginzburg-Landau parameter. If for a superconductor $0 < \kappa < \frac{1}{\sqrt{2}}$, it is called type-I superconductor. This means the superconductivity must be completely destroyed before the system is transparent to a critical magnetic field. For type-II superconductors $\kappa > \frac{1}{\sqrt{2}}$. In this case, the system becomes partially transparent above a critical magnetic field H_{C_1}, also known as the lower critical field. Normal state regions are formed in the system in a closed-pack hexagonal structure. The magnetic flux passes through these normal state regions, whereas the rest of the system remains superconducting. These regions are also called vortices. The size of a vortex depends upon ξ, and each vortex allows only one magnetic flux quanta, ϕ_0. With increasing field, the number of vortices increases and at a field H_{C_2}, known as the upper critical field, the vortex density becomes so large that the whole system becomes transparent to the magnetic field. ξ can be estimated from the following formula,

$$H_{C_2} = \frac{\phi_0}{2\pi\xi^2}. \tag{2.37}$$

H_{C_2} can be measured experimentally.

In BCS theory, the gap Δ at the Fermi surface is considered to be spherically symmetric and, thus, a constant, (Δ_0), since $U_{kk'}$ is taken as a constant. This also suggests that the electron-phonon interaction is isotropic in the momentum space. Superconductors with spherically symmetric (s-wave) gaps are called conventional superconductors since they can be explained within the BCS framework. However, there are scenarios where the gap may not be symmetric (Fig.2.5). In such cases, the pairing mechanism could be different. Such superconductors are called unconventional superconductors [26; 27].

Superconductors can be categorized by other properties, like crystal structure, but those are beyond the scope of this thesis.

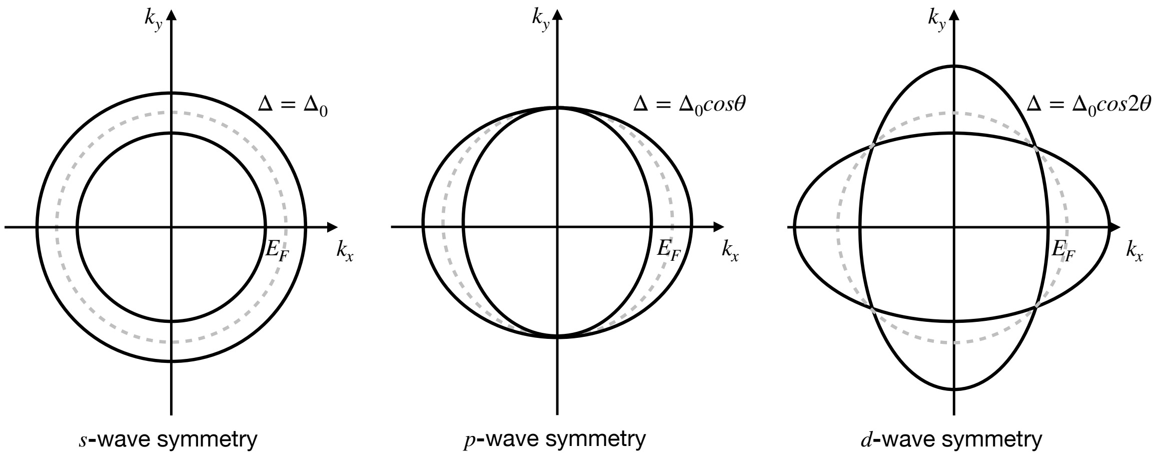

Fig. 2.5 Different gap symmetries for superconductors

2.5 Conclusion

There are three measurable macroscopic parameters that define a superconducting state. They are,

- Critical temperature, T_C. Above T_C superconductivity dies.
- Critical field, H_C. Above H_C, superconductivity is destroyed. For Type-II superconductors, there are two critical fields, lower (H_{C_1}) and upper (H_{C_2}). At H_{C_1} superconductor becomes partially transparent to the magnetic field, and vortices form. At H_{C_2}, superconductivity is completely suppressed.
- Critical current, I_C. We have not discussed I_C before. Current in a superconductor flows through the surface. We know that $\nabla \times H = j_s$, where H is the magnetic field induced by the applied current and j_S is the supercurrent density in a superconductor. Thus current has an associated loop of the magnetic field with it. Since a superconductor is perfectly diamagnetic, such a magnetic loop cannot exist inside a superconductor. Consequently, current cannot exist as well. However, near the surface, the situation is very different. As discussed earlier magnetic field can penetrate up to a certain length from the surface, λ_L, inside the superconductor. Within λ_L magnetic field inside the superconductor is allowed in a fashion of exponential decay from the surface. Consequently, j_S also exists within this range. j_S is maximum on the surface and exponentially decays down inside the superconductor. For type-II superconductors, normal state regions (vortex) could form, allowing supercurrent through the bulk. This is why type-II superconductors can carry a much higher current than type-I

superconductors and are used in applications like high-field solenoid magnets etc. However at sufficiently high current the vortex in type-II superconductors become mobile and superconductivity is destroyed.

Experimentally, T_C, H_C and I_C for a material can easily be measured by varying these parameters while recording the resistance.

Another important defining parameter for a superconductor is the energy gap, Δ. Δ is a microscopic parameter; thus, the measurement for Δ is not straightforward. The single-particle density of states (SDOS), $\rho_S(E)$, for a superconductor is plotted against the energy, E, following the expression from the equation (2.36) in Fig. 2.6 **a**. In this case $\Delta = \Delta_0$. One way to experimentally measure Δ_0 is to transmit energy resolved electrons through the superconducting sample and monitor transport properties like conductance. Since the SDOS is a function of energy, the transport properties of electrons at different energies should be different. One of the most popular methods to send energy-resolved electrons to a sample is point contact spectroscopy [29]. A sharp metallic tip is engaged into a sample to form a mesoscopic channel between the tip and the sample. If the channel diameter is small enough, in the ballistic regime for the transport, the electrons crossing the channel become energetically resolved. The electron energy can be changed by varying the bias voltage between the tip and the sample. At the tip-sample interface, there is also a barrier potential, Z. We can consider two limiting conditions for Z. When $Z \to \infty$, the transport through the mesoscopic channel is pure tunneling. In such a case, the measured differential conductance for a superconductor at different energy values follows $\rho_S(E)$, i.e., way beyond the gap, there is finite differential conductance, near the gap but not within the differential conductance diverges, at the gap the conductance becomes zero since there is no single particle state within the gap. The energy difference between the two points where the differential conductance diverges gives Δ_o. Such kind of spectrum is shown in Fig. 2.6 **e**. Another limiting case is when $Z \to 0$, the transport is purely ballistic. In this case, a similar feature is observed beyond the superconducting gap. However, when the energy falls within the gap limit, an interesting phenomenon called Andreev reflection [28] eventuates at the interface. Since a single electron at this energy cannot transmit to the superconductor at the interface, an electron-hole pair with momentums opposite to each other is created (Fig. 2.6 **a**). This newly created electron and the incoming electron form a Cooper pair and transmit into the superconductor. Thus, the conductance is doubled at energy values within the gap. Such kind of spectrum is shown in Fig. 2.6 **c**. Practically at the interface, obtaining a pure ballistic contact is difficult.

Instead, a mix of ballistic and tunneling channels can be prepared, as shown in Fig. 2.6 **b**. In such a case, a spectrum similar to Fig. 2.6 **d** is observed. The conductance at the energies within the gap tends to double, but the presence of tunneling channels suppresses the signal at the same time. Such competition results in a conductance dip at the centre of the gap and a peak at $\pm\Delta_0$. For non s-wave superconductors or mix-type superconductors, a sub-gap feature along with the peaks at $\pm\Delta_0$ in the spectrum can be observed. For a mix-type superconductor, if the non s wave fraction has lower energy, it can be suppressed by the application of a magnetic field, and the s-wave conductance peak should prevail. For such measurements on a superconductor, a tip made of normal metal should be used. Since Andreev reflection is the phenomenon that allows probing the gap energy, this method is called point contact Andreev reflection spectroscopy (PCARS).

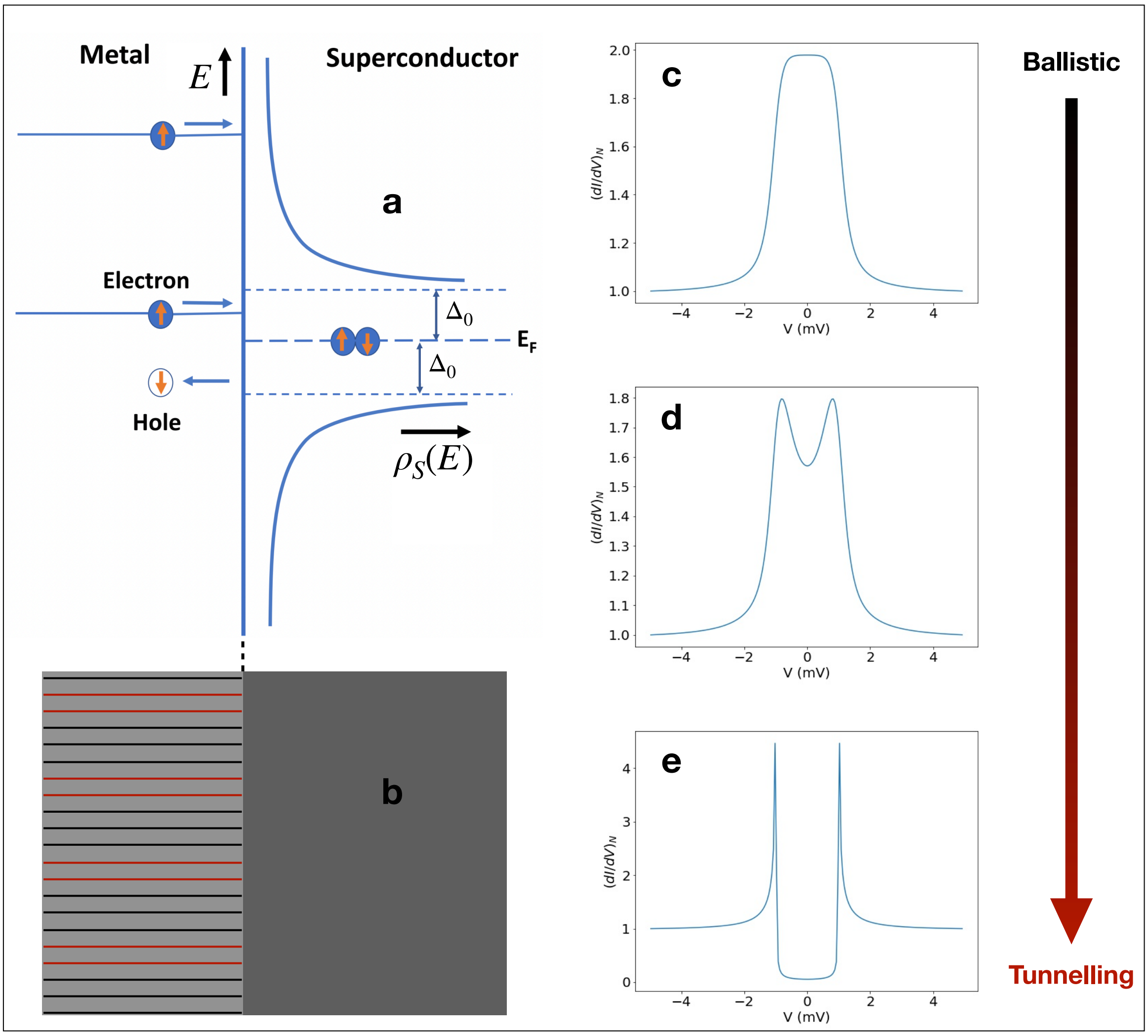

Fig. 2.6 **a** $\rho_S(E)$ vs E graph. The blue vertical line represents the interface between normal metal and superconductor. An electron from the metal side is reflected as a hole at the interface, and a Cooper pair forms. **b** The dark grey area represents superconducting material, and the light grey area represents normal metal (tip in this case). The mesoscopic contact can be considered as a combination of parallel tunneling (red lines) and ballistic (black lines) channels. Differential conductance spectrum for pure ballistic regime (**c**), pure metallic regime (**e**),combination of ballistic and tunneling regime (**d**).

Chapter 3

$LaVO_3/SrTiO_3$ interface

3.1 Introduction

Both $LaVO_3$ and $SrTiO_3$ are Perovskite oxide insulators of Cubic structures with lattice constants 3.930Å and 3.905Å, respectively. $LaVO_3$ is a Mott insulator, whereas $SrTiO_3$ is a band insulator. The interfaces of these two insulators under some particular conditions are conducting. In 2007 Y. Hotta et al. observed that when the $LaVO_3$ layer is grown over $SrTiO_3$ [001] surface, the interface becomes conducting only when the termination layer of $SrTiO_3$ is TiO_2 [6]. For a similarly grown $LaVO_3$ layer over $SrTiO_3$ [110], however is an insulator. In the former case, a polar discontinuity arises at the interface, whereas in the latter case, no such discontinuity can exist at the interface. The authors concluded that the dominant mechanism that allows such conducting interface is the polar catastrophe. It was also reported recently that the conductivity of the interface depends upon the La stoichiometry as well [30]. While cooling down in magnetic field bulk, $LaVO_3$ undergoes an anti-ferromagnetic transition at 145K [31]. This magnetic property is owed to the V ions. In the field cool down, a magnetostrictive force in $LaVO_3$ allows such magnetic transition. Thus, for a thin film, some effects due to the magnetic ordering (not necessarily by field cooling) may also be observed at the interface. Also, for a $LaVO_3$/ $SrTiO_3$ heterostructure the interface may be strained due to lattice mismatch between $LaVO_3$ and $SrTiO_3$. All these facts cumulatively indicate that the conducting phase at the interface may be complex. The conducting interface is also obtained if $LaVO_3$ is grown over $SrTiO_3$ [111] surface. However, between two prepared interfaces by our collaborators for $SrTiO_3$ [001] and [111] surfaces, the former one had higher carrier density and mobility (Fig. 3.1) [32]. Thus, we chose $LaVO_3/SrTiO_3$ [001] interface for our ultra low-temperature electronic transport studies.

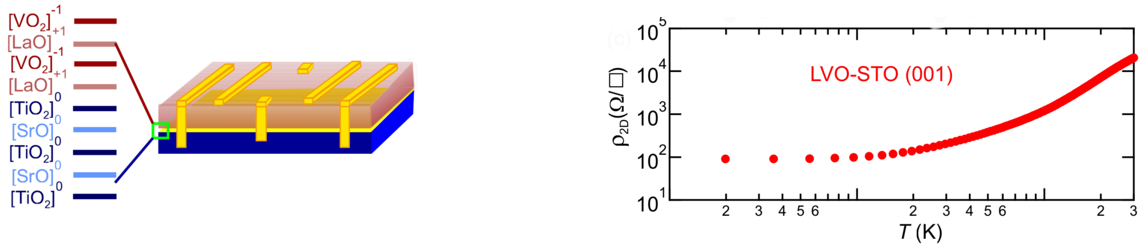

Carrier Density: 3.1×10^{14} cm^{-2}, **Mobility**: 220 cm^{2}V^{-1}s^{-1}

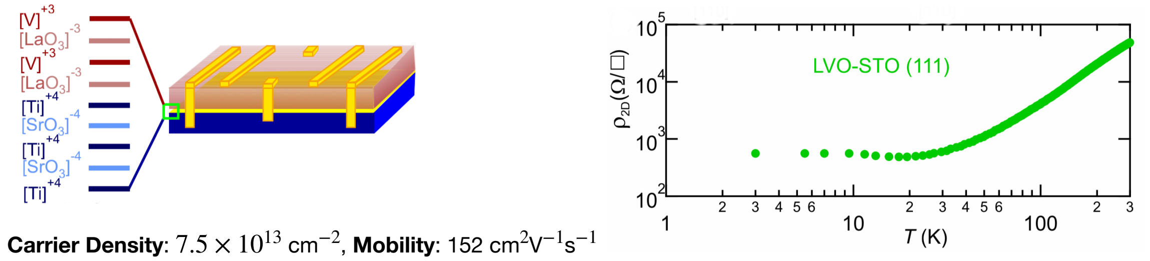

Carrier Density: 7.5×10^{13} cm^{-2}, **Mobility**: 152 cm^{2}V^{-1}s^{-1}

Fig. 3.1 Graphical representation of $LaVO_3/SrTiO_3$ [001] (left top) and $LaVO_3/SrTiO_3$ [111] samples with their respective polar stacking is shown. For both cases, resistivity vs temperature data is presented (right top and right bottom).

3.2 Possible interfacial properties

We have already discussed in the first chapter that in a polar catastrophe scenario, migrated charges to the interface participate in the conduction. by accepting these charges, d-block elements lower their oxidation state. In case of $LaAlO_3/SrTiO_3$ [001] the Ti ions act as acceptors. However, in the case of $LaVO_3/SrTiO_3$ [001], both Ti and V are d-block elements, and there is a possibility that the migrated electrons are accepted by V as well as by Ti. In $LaVO_3$, the natural oxidation state of V is +5, but it can be downgraded as well by receiving electrons since V has variable oxidation states. In such a scenario, both V-d and Ti-d bands should participate in the conduction. Since V is the source of magnetization in $LaVO_3$, the conducting electrons contributed by the V-d bands could be spin polarized. The band (Fig. 3.3) and spin band (Fig. 3.4) structures for both $LaAlO_3/SrTiO_3$ [001] and $LaVO_3/SrTiO_3$ [001] interfaces were calculated by our collaborators using supercells consisting of 4 layers of $SrTiO_3$, 4 layers of $LaAlO_3$ or $LaVO_3$ and 20Å vacuum in the out of plane direction ([001]) as shown in Fig. 3.2. It is evident that for $LaVO_3/SrTiO_3$ [001] interface both V-d and Ti-d bands cross the Fermi level ensuring contribution from both the bands in conduction. Also, there is relative shifting between the spin-up and spin-down bands in the case of

$LaVO_3/SrTiO_3$ [001] interface, which indicates the presence of spin-polarized electrons. For $LaAlO_3/SrTiO_3$ [001] interface such shifting is not there.

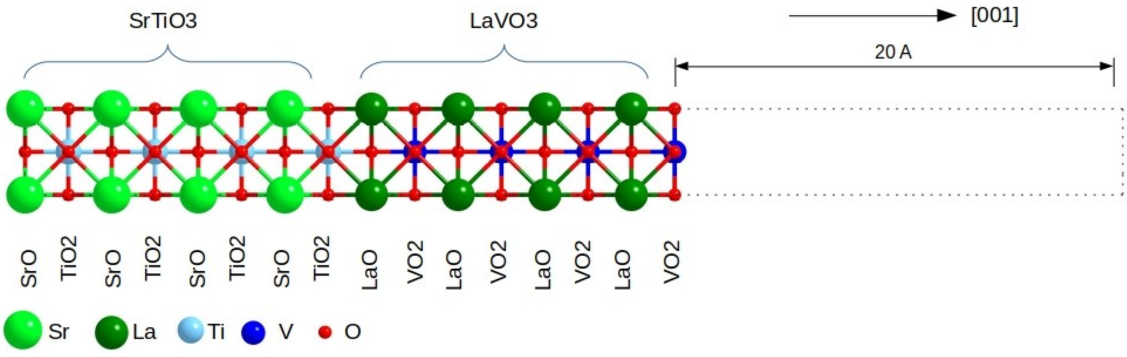

Fig. 3.2 Supercell structure used for band and spin band structure calculations.

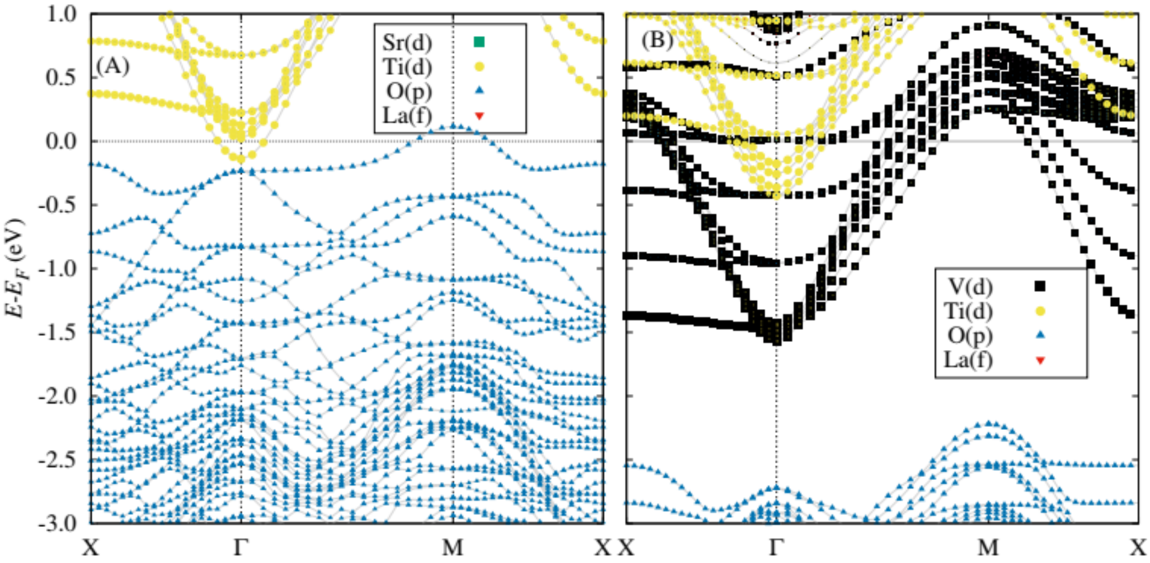

Fig. 3.3 Band structure of (A) $LaAlO_3/SrTiO_3$ [001] and (B) $LaVO_3/SrTiO_3$ [001] interfaces.

We have discussed the contribution of $LaVO_3$ at the interface, but what about the contribution of $SrTiO_3$? $SrTiO_3$ is cubic at room temperature and undergoes a structural phase transition at around 110K. Similar structural phase transitions are observed in some other Perovskite oxide crystals. Such phase transitions lead to a relative shift between positive and negative sub-lattices for these crystals, and ferroelectric order sets in. Also, most of the available ferroelectric materials have Perovskite structures. $SrTiO_3$ is special. At around 30K, the dielectric constant of $SrTiO_3$ starts diverging, which is a signature of the onset of a paraelectric to ferroelectric transition, but it never settles to a ferroelectric phase. The dielec-

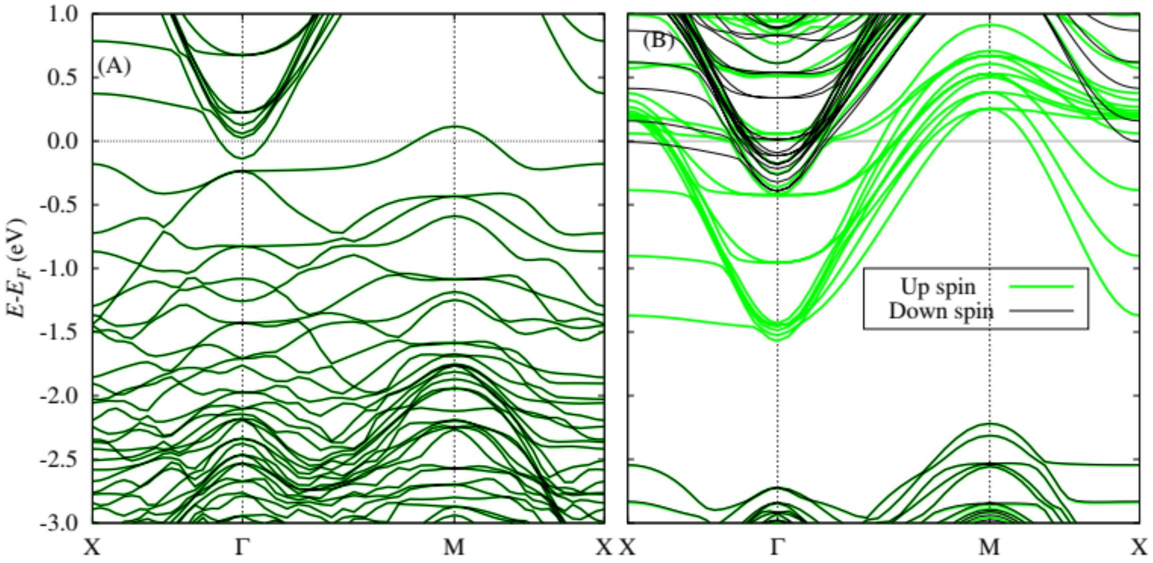

Fig. 3.4 Spin band structure of (A) LaAlO$_3$/SrTiO$_3$ [001] and (B) LaVO$_3$/SrTiO$_3$ [001] interfaces.

tric constant saturates at about 4K and remains constant down to 0K. Zero point quantum fluctuation forbids ferroelectric transition of SrTiO$_3$. Thus, SrTiO$_3$ is quantum paraelectric [33], which means at low temperatures, it is on the verge of becoming a ferroelectric but not a ferroelectric. This suggests that strain in SrTiO$_3$ could assist in a ferroelectric transition. The phase diagram of a strained SrTiO$_3$ film is shown in the article by Haeni et al [34].The strain, ε_S on a surface is defined by $\varepsilon_s = \frac{a-a_0}{a_0}$, where a and a_0 are in-plane lattice parameters with and without strain respectively. A positive value of ε_s represents expansive strain, whereas a negative value represents compressive strain. Haeni et al. has discussed that there are two available ferroelectric regions in the phase diagram for compressive and expansive strains, respectively. However, the quantum paraelectric phase of the SrTiO$_3$ is almost at the boundary of the ferroelectric phase for expansive strain and far from the ferroelectric phase for compressive strain. Thus, for a minimal expansive strain, the SrTiO$_3$ film becomes ferroelectric. The lattice parameter of LaVO$_3$ is greater than that of SrTiO$_3$, which suggests that at LaVO$_3$/SrTiO$_3$ [001] interface SrTiO$_3$ may experiences expansive strain and ferroelectricity may emerge.

3.3 Conclusion

From the discussion of the last section, we may conclude that the LaVO$_3$/SrTiO$_3$ [001] interface not only hosts spin-polarized conduction electrons, but the interface itself may have a ferroelectric nature at low temperatures. The interface should exhibit complex phenomena. If the interface becomes superconducting, there is a high possibility that the superconductivity is unconventional due to spin-polarized electrons. It should also be interesting to investigate whether application of an electric field at the interface allows the conducting electrons to react in a nature which may indicate the presence of ferroelectric phase at the interface in a direct/ indirect way. All these facts motivated us to conduct an ultra-low-temperature study of the $LaVO_3/SrTiO_3$ [001] interface.

3.4 Contribution

- **Fig. 3.1:** S. Chakraverty et al., Quantum Materials and Devices Unit, Institute of Nano Science and Technology, Sector-81, Punjab, 140306, India.
- **Fig. 3.2, Fig. 3.3, Fig. 3.4 and band/ spin band structure calculation:** Rajesh Sharma and Tanmoy Das, Indian Institute of Science, CV Raman Rd, Bengaluru, Karnataka 560012, India.

Chapter 4

Cryogenic instrumentation

4.1 Introduction

A system with a sufficiently small size does not guarantee any observable quantum phenomena since the quantum signal is usually masked by thermal fluctuation. In our discussion about the superconducting phases in the perovskite oxide interfaces, we have also observed that, in most cases, the transition appeared at very low temperatures. Measurements at such low temperatures have two fundamental difficulties.

- The cooling power of the cryogenic setups becomes very low, which limits the maximum possible current through a sample and signal to noise ratio becomes very small. Isolating sources of noise is a way to improve the ratio.

- Thermalization of the sample requires some critical cryogenic engineering, since, the thermal conductivity at this temperature is very low. There are very few materials that can be used for parts/ setups to use in such environment. Also, the thermal contact between two materials, thermalizing with each other, should be strong, and the contact area should be maximized for optimal efficiency.

In our experiments, we have taken proper measures to overcome such difficulties. We have conducted our experiments in a commercial dilution refrigerator (DR) manufactured by Janis (model: JDR500) with 350 μW cooling power at 100 mK and 10 mK base temperatures. The system is equipped with a 16T single-axis magnet. Since our DR is a wet system minimizing liquid 4He loss is also a concern to be addressed. In our case, although there is a reliquefier that manages the boiled-off 4He from the system in normal operating conditions. However, switching the magnetic field at a value beyond 7.5T requires careful operation of the magnet to prevent 4He loss. At this range, the Joule heating from the current at the magnet leads is high enough to overpower the reliquefier cooling efficiency and driving the magnet continuously is not possible. A protocol in the data acquisition program was employed that successfully manages the Joule heating in the magnet leads. In the following sections, I will discuss all the details of our setup.

4.2 Noise isolation

An experimental setup can be affected by two types of noises primarily:

4.2.1 Acoustic noise

Acoustic noise propagates through the surface of the earth and transmits to the system. Sources of such noise are plenty in the environment. Basically, any source of vibration can generate such noise and disturb the signal, especially in experiments where spatial distances between elements within an experimental setup are crucial (like scanning tunneling microscopy). This noise can be minimized by increasing the system's mass, which consequently reduces the natural vibration frequency down to almost DC. However, for a commercial system, the mass cannot be increased arbitrarily. The alternate way is to build a massive concrete structure and attach the system with that to increase the total mass effectively. This structure should be isolated from the rest of the earth by damping materials like neoprene sheets, quartz sand, etc. In our case, to build such a facility an area of 144” × 122” was excavated down to 126”. A concrete construction was built (Outer wall in Fig. 4.1) to block the groundwater. The floor was covered uniformly with 2" thick neoprene sheets. Another concrete structure was constructed (Inner wall in Fig. 4.1) over the neoprene floor. This concrete structure is separated sideways from the inside of the outer walls by quartz sand. DR was installed over this structure which, in our case, acts as the massive block. The details of the construction are presented in Fig.4.1. The 3D model was designed using Solidworks.

4.2.2 Electronic noise

The source of such noises could be ground loops, radio signals etc. For very low signal measurements, grounding should be clean. The DR has mainly two parts: the DR itself, which is electrically passive and the gas handling system (GHS) electrically active. A photo of the GHS is shown in Fig.4.6. The GHS contains pumps, compressors etc. which dump high current (with respect to the measurement signal) to the ground. This consequently modifies the reference for the measurement system, and the measured signal should have a noise signal with the line frequency (50 Hz in our case) overlapped. The amplitude of the noise signal depends upon the magnitude of the current dumped to the ground by the GHS. One immediate consequence of the ground noise is the saturation of the signal from resistive thermometers at a very low temperature. We have observed that for an inefficient grounding, our RuOx thermometer saturates at 40 mK, whereas the base temperature of our DR is 10 mK. The solution is to use a separate grounding for the measurements and electrically isolate the GHS from the DR. For our measurements, we have used clean isolated ground. There are two stainless still gas lines, namely the still pumping line and the mixture return line, which connect GHS with DR. For both of these lines, electrical insulators are used at the junctions. The DR is connected to the measurement ground. Another source that can dump noise into the DR is the 4He reliquefier. Usually, the 4He feedthrough line of the reliquefier is electrically short with the DR, which mixes two grounds (the reliquefier has the same ground as GHS). In our case, we have isolated the feedthrough line using Kapton tapes.

To cut off the radio signals, the ideal solution is to use a Faraday cage. In our case, we did not build a Faraday cage. Instead, we have channelled our DC/low-frequency signal lines from the DR to the distribution box through a stainless steel bellow (Fig. 4.3). The lines are terminated at BNC connectors at the distribution box. We have used twisted pairs to minimize mutual induction in the signal lines. We have used shielded cables from the break-out box to the measurement setup. All the signal cables are carefully manoeuvred to avoid induction from the power cables for the instruments.

4.3 Dilution refrigerator

In the lab, ultra-low temperature is reached by force evaporative cooling of a cryogenic liquid. A liquid phase coexists with a vapour phase. Pumping out the vapour phase causes inequilibrium in the system, the lowering in vapour pressure is countered by the increment of the evaporation rate of the liquid at the liquid-vapour interface until a steady state is reached. For a liquid-to-vapour phase transition, latent heat from the liquid phase is extracted during the evaporation, which eventually cools down the liquid. The steady state (even the base temperature) is limited by the pumping rate and evaporation rate, as well as the liquid surface-to-volume ratio. However, there are technical and physical limitations to evaporative cooling. For an optimum condition, the typical base temperatures for different cryogenic liquids are given in Table 4.1.

To achieve a temperature in the order of 10mK, the evaporative cooling process must be modified [35]. In a DR, such modified evaporation process is used to cool a cryogenic liquid, a mixture of 3He and 4He (in gas volume 27L and 100L in our case). To understand the DR working principle, let us look at the phase diagram of liquid 3He and 4He mixture in Fig.

Table 4.1 Properties of cryogenic liquids

Cryogenic liquid	**Liquefaction temperature**	**Base temperature**
Nitrogen	77K	60K
4He	4.2K	1K
3He	2K	300mK

4.4 and consider a phase point **A** (45% 3He concentration at 2K) in the phase diagram as our starting point. At this point, the mixture is in a normal fluid state. As the temperature is lowered, the phase point crosses the normal fluid - super fluid boundary and reaches point **B** (45% 3He concentration at 1.1K). The normal evaporative cooling works at this point as the vapour pressure of 3He for this phase is high. With further cool down, the phase point hits the boundary of the forbidden region, point **C** ((45% 3He concentration at 0.7K)). Lowering temperature beyond this point causes phase separation in the liquid.

The phase point is separated into two: 3He dilute phase, point **D** and 3He rich phase, point **E**. Since 4He is heavier than 3He, the 3He-rich phase floats over 3He dilute phase (since this phase contains more 4He). This phase separation is the key that allows cooling down to a few mK. The cool-down happens at the interface of these two phases. From the phase diagram in Fig. 4.4, it is evident that at 0K, the phase point **D** would reach a non-zero value for 3He concentration. This suggests, for a 3He-4He mixture, even at 0K, there is finite solubility of 3He in 4He.

A simplistic design of the DR is shown in Fig. 4.5. In this design There are mainly two stages: still and mixing chamber (MC). Both of them contain a liquid mixture (enough mixture should be condensed). However, the temperature at the MC only allows phase separation. Although the MC is filled with liquid in phase-separated form, the still is partially filled with 3He dilute phase. The vapour pressure in this phase is much higher for 3He than 4He. Thus, the still is filled with 3He vapour. There is a heater in the still chamber that can increase the vapour pressure as well. Pumping out the 3He vapour lowers the percentage of 3He in the dilute phase, balanced by incoming 3He atoms from the 3He-rich phase to the 3He dilute phase. 3He rich phase is an ordered phase, whereas 3He dilute phase is a disordered phase for 3He. Thus the dilute phase has higher entropy than the rich phase, and while the transition from rich to dilute phase occurs, 3He atoms acquire energy from the rich-dilute interface in the form of latent heat. In this way, the interface of the two phases starts cooling down. A closer look at Fig. 4.5 reveals that this is a top-down evaporation process of 3He through 4He. In the case of pure 3He cryogenic liquid, the vapour pressure is very low at 300 mK. Such limitation is not there in a dilution process since the vapour pressure in still can be increased by heating. Since the phenomenon that allows the cooling is 3He rich phase to 3He dilute phase conversion, it is called the dilution refrigeration technique.

Although the simplistic DR model is enough to understand the basic working principle of a DR, the actual operating process of the DR is much more complex. It should also be noted that the vapour from still always contains some small amount of He4 in reality. For the simplicity of discussion we have not considered this aspect. DR process is a cyclic process. Pumped out 3He gas is compressed and then again fed into the DR. The outgoing gas and incoming gas are thermalized at different stages. The schematic of a DR [36] is shown in Fig. 4.4. From the top, the first stage is the 4K stage which is in direct thermal contact with liquid 4He for a wet system. The next stage is the still. Between the 4K stage and the still, there is Joule Thomson cryocooler, comprised of a recuperative heat exchanger or Joule Thomson heat exchanger (JTHE) and a primary flow impedance, Z_1. JTHE thermalizes the incoming and outgoing gas. At the end of JTHE, just above the still, there is Z_1 which acts as a throttle for Joule Thomson cooling as well. The Joule Thomson process cools down the incoming 3He from 4K to 2K. The compressor mentioned earlier drives the Joule Thomson process. Between still and MC there is another stage, the intermediate cooling plate (ICP). Just below the still there is secondary flow impedance, Z_2, which stops the backflow of the mixture. Z_2 terminates at a continuous heat exchanger (CHE) located just above the ICP. CHE thermalizes the 3He dilute and rich phase. Between ICP and MC, there is a step silver heat exchanger (SHE) to thermalize 3He rich and dilute phase.

The DR has several heat exchange steps to cool the incoming 3He gas. The flow rate of 3He should be optimum. In case of a high flow rate, incoming 3He gas does not have enough time to thermalize. On the other hand, if the flow rate is too low, the cooling power is reduced. The Joule Thomson cooling process depends on the pressure and temperature of the throttling input and the pressure of the throttling output. The flow and pressure are optimized by Z_1 and Z_2. The temperature of different stages of the DR during operation is presented in Fig. 4.6. The coldest point in a dilution refrigerator is the MC. However, an MC cannot fit inside a superconducting magnet bore. Thus, a thermal extension is required from the MC stage to the magnet bore. In our case, this is called cradle (Fig. 4.6) which is made of silver. At the bottom of the cradle facing the MC, there is one 51 pins male nano-D connector and 6 male SMP connectors. 15 superconducting DC wires and 36 manganin DC wires in shielded twisted pair form are guided from the other end of the nano-D connector to two 32 pin circular connectors at the top of the dilution refrigerator for external access. The DC wires are thermalized at each stage of the DR. A shuttle (Fig. 4.8) made of coin silver is also supplied by Janis. The shuttle is a cylindrical structure with windows and screw holes and also has matching 51 pins female nano-D connector, and 6 female SMP connectors. The shuttle can be attached to a manipulator (a photo of the manipulator is shown in Fig.4.6), which can drive the shuttle down to the bottom of the cradle through a central clear shot in the DR and release the shuttle after the matching connectors of cradle and shuttle are mated.

During the DR operation to stop radiation through the clear shot to the MC, there are two shutters at the bottom of the 4K plate and the still stage. The shuttle is thermally connected to the cradle. This whole operation is executed at a high vacuum of the order of 10^{-6} mbar. To access the shuttle when extracted from the DR a load lock chamber (LLC) is designed (Fig.4.7), which is connected between the manipulator assembly and the DR insert. DR and the LLC are separated by a VAT gate valve. LLC also has a vacuum of the order of 10^{-6} mbar. only during the vacuum operation, as mentioned earlier, the gate valve is opened. To remove or attach the shuttle from and to the manipulator at room temperature, first, the LLC vacuum is broken then one of the LLC windows is opened to access the shuttle. During this, the VAT gate valve protects the DR unit from exposure to the air. The shuttle without the sample mounting mechanism is of no use. We have designed our sample mounting mechanism/ sample space which is discussed in the next section.

4.4 Sample space

There are several challenges in designing a sample stage for a dilution refrigerator. First, at sub 100 mK temperature, most materials are not good thermal conductors. At the contact of two materials, the thermal resistance (Kapitza resistance) is also very high at low temperatures. Thus, for a sample space, ultra-low temperature compatible materials should be judiciously selected, and the inter-material thermal contacts should be tight to minimize thermal resistance. Secondly, the sample must situate at the centre of the magnet during magnetic measurements. For our magnet, there is a spherical volume of 10 mm diameter at the centre where the applied field is uniform within an error of $\pm 0.1\%$. The sample must sit in this region. Also, the inner diameter of the shuttle is about 33 mm. Thus, the sample space has two restrictions in terms of dimension apart from a limited choice of cryogenic materials. The sample space design has two components made of OFHC copper mainly: a sample stage and a sample holder, as shown in Fig. 4.9. Sample stage is tightly attached to the shuttle with screws, as shown in Fig. 4.8. Sample holder, on the other hand, is a moving part and can be attached to or detached from the sample stage (Fig. 4.9). Sample can be mounted on a sample holder and inserted to the sample stage. This sample exchange process does not require the removal of the sample stage from the shuttle. The sample holder can be inserted into the sample holder through the shuttle window. The sample stage has a locking mechanism, as shown in Fig. 4.10, which locks the sample holder at a particular position.

Two spring-loaded wings, as shown in Fig. 4.10, act as locks. The wings have protruded structures, and the mating groove structures are on the sample holder (sample holder locking groove), as shown in Fig. 4.12. During the sample holder insertion, the wings move apart from each other and then at a particular position, the locking structures on the wings and the sample holder match; consequently, the sample holder is locked in position. Different parts of the sample space and the step-by-step assembling process are shown in Fig. 4.9 - 4.12. The sample stage assembly (sample stage base and wings (Fig. 4.10)) has additional slots for thermal anchoring OFHC copper braids connected to these slots. The other ends of the OFHC copper braids are terminated to thermal sinks, which are also made of OFHC copper (Fig. 4.11). These thermal sinks are tightly screwed to the shuttle (Fig. 4.8). The sample holder has a rectangular RO4003C PCB (Fig. 4.12). We call this the sample PCB and mount the sample on it. The sample stage has two semi-circular RO4003C PCBs, which are called pogo-pins-PCBs (Fig. 4.12). The PCB designs are given in Fig. 4.13. The sample PCB has a central copper pad on the front side where the sample is pasted and then connected to the nearby copper tracks, which are also on the front side, by wire bonding. The copper tracks end in an array of circular copper pads on the backside of the PCB. The circular pads and the tracks are connected by plated through holes. The pogo-pin-PCBs also have the same array of circular copper pads on the front side. In this case, the circular pads have holes at the centres to mount pogo-pins. Both the 3D design and the actual pogo-pins-PCB after mounting the pogo-pins are shown in Fig. 4.12 and Fig. 4.13, respectively. These circular copper pads in the pogo-pins PCB are connected to copper tracks. These tracks are connected to the 51 pins nano-D connector at the bottom of the shuttle by phosphor-bronze wires. When the sample holder is locked in the sample stage, each pogo-pin connects the respective circular copper pads on the sample PCB. The Sample mounting side/ top side of the sample PCB is marked in Fig. 4.9. During the insertion of the sample holder, the pogo-pins adjust their heights by sliding over the ramp on the sample holder (Fig. 4.12).

The lateral stress on the pogo-pins is countered by the pogo-pins lateral support on the sample stage (Fig. 4.12). This support can be made of sapphire, PEEK, Kapton etc. At the moment, we are not using this part. The sample holder is thermalized with the sample stage by wings. In the sample stage, there are covers (Fig. 4.10). The wings also push a portion of the sample holder against the covers. Pogo-pins assists to this pushing force as well with their own spring-loaded mechanism. In this design, the pogo-pins are used not only for electrical connections but also to reduce thermal resistance between the sample stage and the sample holder. We have a calibrated RuOx resistive thermometer in the sample holder to measure the sample temperature (Fig. 4.9). The thermal performance of the sample space is given in

Table 4.2. The whole sample space assembly fits into a cylinder of 31.5 mm diameter and 34.5 mm height.

Table 4.2 Thermal performance of the sample space compared with the MC performance

Temperature	**Time**
500mK to 100mK	1 hr 15 minutes (<1 hr for MC)
100mK to 50mK	1 hr (30 min for MC)
50mK to 27mK	1.5 hr (48 min for MC)

4.5 Thermometry and measurement electronics

To monitor the temperature at different stages of DR during operation we use Model 372 ac resistance bridge & temperature controller from Lakeshore. In the Table 4.3 heaters and temperature sensors used at different parts in the DR are given. All the heaters but the one in the sample space are controlled by the lakeshore 372 controllers. On the other hand, the sample space heater is powered by a Keithley constant current source. Z_1 heater is used to unblock the impedance in case it is clogged by frozen impure gas like nitrogen. The Still heater is used to increase 3He vapour pressure at the still, which consequently increases the flow rate and cooling power. We use the MC heater to empty the MC chamber of the mixture during shuttle transfer.

Table 4.3 List of temperature sensors and heaters

DR part	**Temperature sensor**	**Heater**
4K stage	Cernox	X
Z_1	Cernox	50Ω cartridge heater
Still	Cernox	100Ω cartridge heater
ICP	RuOx	X
MC	Cernox, RuOx and CMN	100Ω cartridge heater
Sample space	RuOx	In house made coil with phosphor bronze wire (10Ω)

RuOX and Cernox are resistive-type sensors and are calibrated for the temperature ranges of the respective DR parts. RuOx sensors at the MC and sample stage are calibrated against a CMN thermometer for sub-100 mK temperature. CMN is a magnetic salt and follows Curie Weiss law, $\chi \propto \frac{1}{T-T_C}$ down to 6 mK. A mutual inductance measurement is done to determine χ. Lakeshore 372 supplies low-frequency AC excitation to the thermometers and can measure the imaginary part of the signal along with the real part. In mutual inductance measurement, *chi* can be extracted from the imaginary part, also known as reactance. Temperature and reactance have an inverse proportional relation for CMN. To calibrate the RuOx thermometers first reactance of the CMN thermometer is determined at a particular temperature against a commercially calibrated Cernox above 100 mK. Then taking this point as the reference, we can evaluate sub-100 mK temperatures from the reactance-temperature relationship by measuring the reactance only. This measured temperature is then plotted against the measured RuOx resistance values to obtain a calibration curve for the RuOx.

For AC measurements, we have used the SR830 lock-in amplifier from SRS. We usually kept the bandwidth of the low pass filter at around 20 Hz. We set the output frequency from the lock-in to some value where the signal is clean within this bandwidth. We have never set the frequency above 789.1 Hz and always been careful to choose a frequency which is not a harmonic or subharmonic of 50Hz, the power line frequency. For DC measurements, Keithley 6221 constant current source and Keithley 2000 multimeter are used. We have also used Keithley 2400 source meter as the gate voltage source for gate-dependent measurements. Keithley 2400 can supply up to ±210 V from a floating output. To apply higher gate voltage, we connect a high-voltage piezo driver probe from the RHK R9 controller in series with Keithley 2400 (Fig. 4.14). RHK R9 can supply up to ±215 V. Thus, with two power supplies in the series configuration, we can reach up to ±425 V.

4.6 Experimental methods

We employed contacts at the $LaVO_3$/ $SrTIO_3$ interfaces by ultrasonic wedge-type wire bonding. For resistivity and Hall measurements, we use Hall geometry. We convert the measured resistance, R, to sheet resistance, $R_\Box$ with the formula: $R_\Box = R\frac{w}{l}$, where w and l are the effective width of the sample and the distance between voltage probes. The back of the $SrTiO_3$ is coated with silver paint to make a gate electrode. Voltage, V_G, applied to this electrode changes the interfacial properties. This is called back gating. The circuit diagram for gate-dependent/ normal resistivity measurements is presented in Fig. 4.14.

For resistance vs temperature measurements, the current to the heater at the sample space is gradually increased in very small steps. At each step, there is a waiting time for the sample to thermalize before the resistance data is recorded at that step. We have not used any PID controller for the sample space heater. Schematic for a sub-surface point contact Andreev reflection spectroscopy (SSPCARS) measurement is shown in Fig. 4.15. In SSPCARS, differential resistance is measured at different energies. During wire bonding, some contacts form a ballistic channels at the interface. Such contacts are used for SSPCARS. In Fig. 4.15, contact A is of ballistic type. Differential resistance is measured by a lock-in amplifier to minimize the noise in the data. A DC signal, I_{DC}, along with an AC signal, $I\sin\omega t$, a few orders of magnitude smaller, is sent through the ballistic contact. A ballast resistor at the lock-in output converts the AC voltage source to an AC signal source. The potential drop, V, across the point contact can be expressed as,

$$V(I_{DC}+I\sin\omega t) = V(I_{DC}) + \frac{dV}{dI}I\sin\omega t + ... \tag{4.1}$$

In the equation (4.1) the first term on the RHS can be measured by DC voltmeter. The second term which contains differential resistance expression, can be measured by lock-in amplifier.

4.7 Data acquisition

An automated data acquisition technique is used. The instruments are interfaced with a computer using RS232, serial, and Ethernet ports, depending upon availability. For RS232 communication, the NI GPIB controller is used. For Ethernet, a network switch is used for multiple connections. Automated data acquisition programs are written in Python and LabView. Depending upon the instruments, GPIB, serial and TCP/IP communication protocols are used to send commands to the instruments and read the acquired data. For TCP/IP protocols, static IP addresses are used. We have used separate programs for different types of measurements. For the program to measure magnetoresistance, a special magnet sweeping protocol is implemented to avoid overheating the magnet leads. The flow chart of this program is presented in Fig. 4.16-4.17. We have observed that below 7.5 kG, the magnet can run in driving mode. Beyond 7.5 kG, the magnet leads start heating, and cryostat pressure rises. The cryostat has a pressure safety relief valve of 4 psi. With a higher magnet lead current, the cryostat pressure increase rate also is enhanced. Although we measure the sample while the magnet is in the driving mode, we also set the magnet in the persistence mode to cool the leads. We have seen that for a higher magnetic field value, the persistence mode to driving mode switching should begin at a lower pressure, P_{limit}, to maintain the cryostat pressure below 4 psi. Our formulation of P_{limit} is optimized for a maximum magnetic field of 14T.

4.8 Conclusion

We have set up the Zero lab from scratch, installed the dilution refrigerator and performed ultra-low temperature measurements. Special care is taken to minimize acoustic and electronic noises. A load lock chamber is designed in-house. An ultra-low temperature sample space is also designed. The base temperature of the sample space is 27 mK, whereas the base temperature of the MC is 10 mK. However, given the operating temperature range, the sample space thermal performance is very good. The thermal performance can be further increased by using coin silver and sapphire PCBs instead of OFHC copper and RO4003C PCBs. The mechanical performance of the ramp can be improved by using sapphire over layers. The design of the sample space allows quick sample exchange in the load lock chamber. A magnet sweeping protocol is employed in the program for magnetoresistance measurement to optimize the magnet lead heating so that the 4He boil-off can be efficiently managed by the reliquefier.

4.9 Contribution

- The load lock chamber Solidworks model and the CAD drawing of the PCBs are produced jointly with Mona Garg.

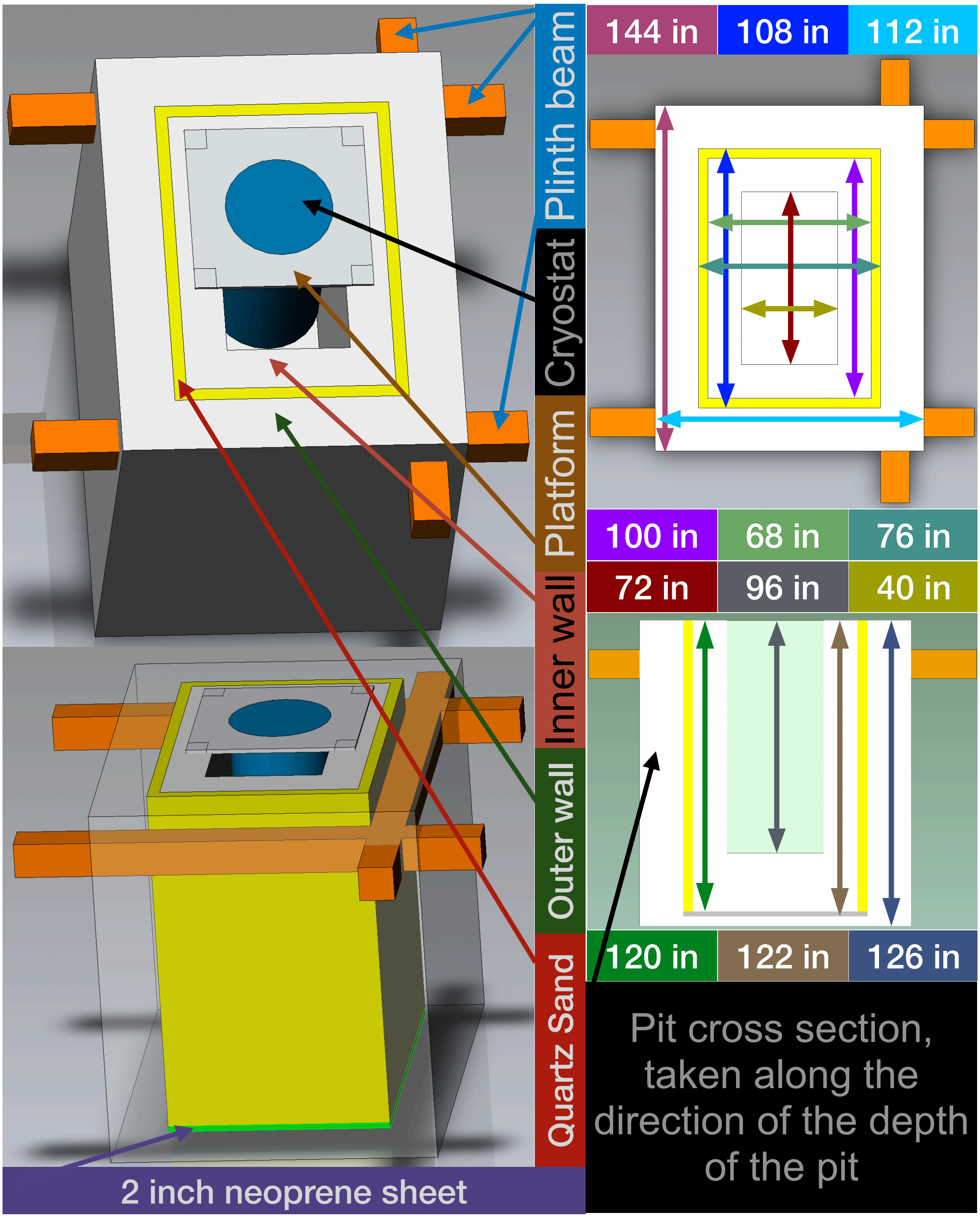
Plinth beam
Cryostat
Platform
Inner wall
Outer wall
Quartz Sand
2 inch neoprene sheet
144 in
108 in
112 in
100 in
68 in
76 in
72 in
96 in
40 in
120 in
122 in
126 in
Pit cross section, taken along the direction of the depth of the pit

Fig. 4.1 3D model of massive concrete block, also known as pit, to minimize acoustic noise.

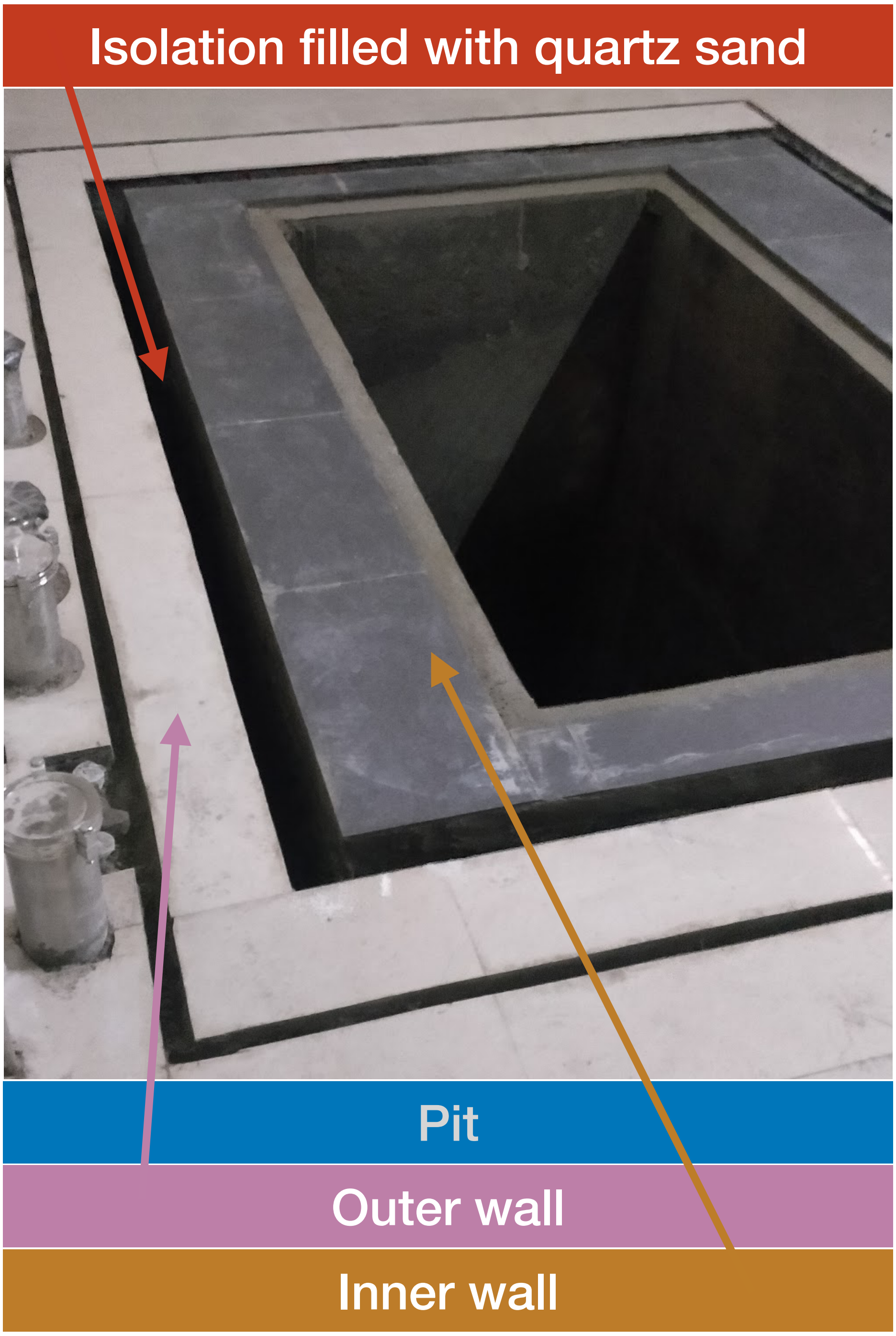
Isolation filled with quartz sand
Pit
Outer wall
Inner wall

Fig. 4.2 A photo of the pit after construction.

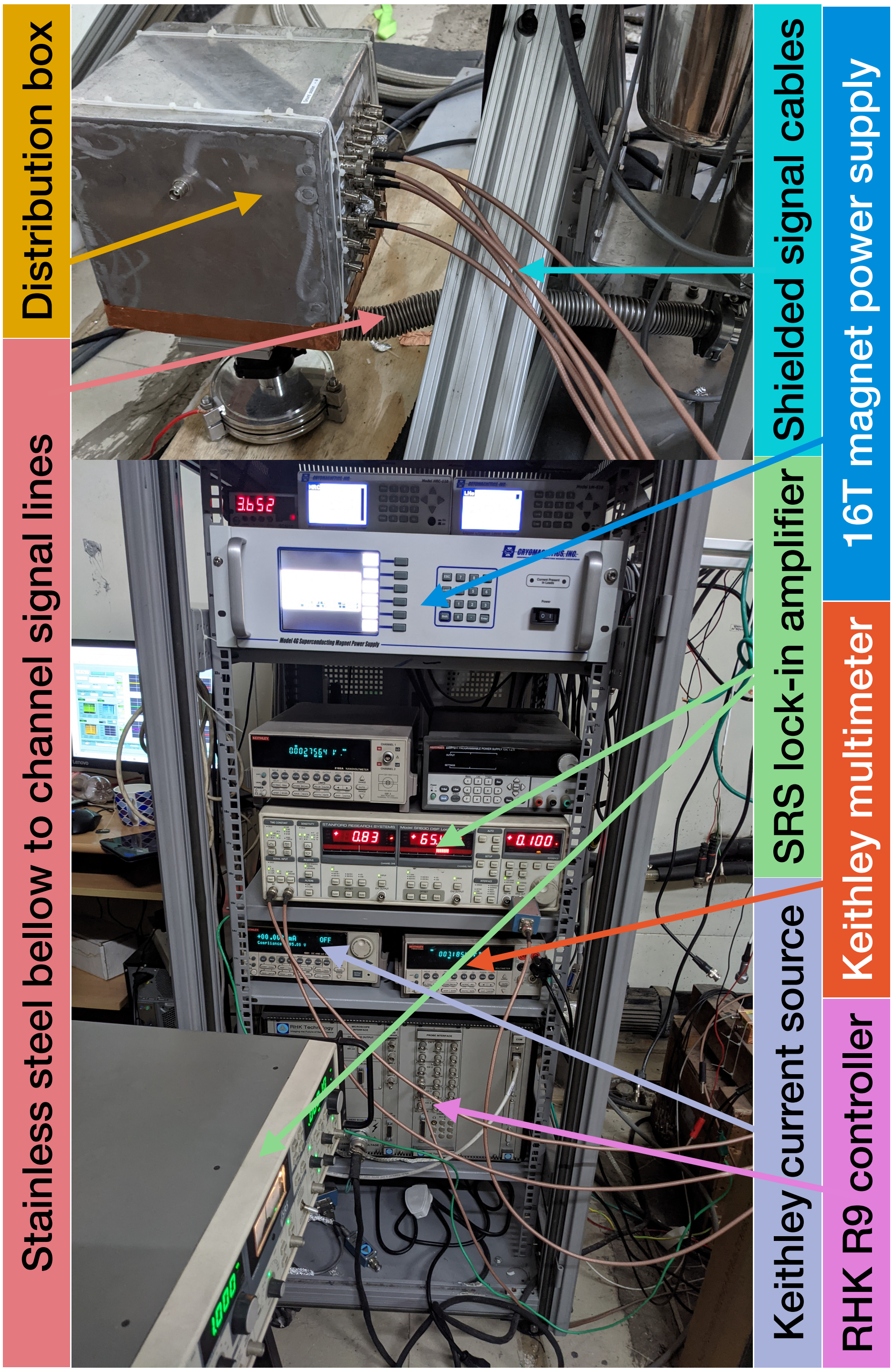
Distribution box
Stainless steel bellow to channel signal lines
Shielded signal cables
16T magnet power supply
SRS lock-in amplifier
Keithley multimeter
Keithley current source
RHK R9 controller

Fig. 4.3 A photo of the electronic measurement setup

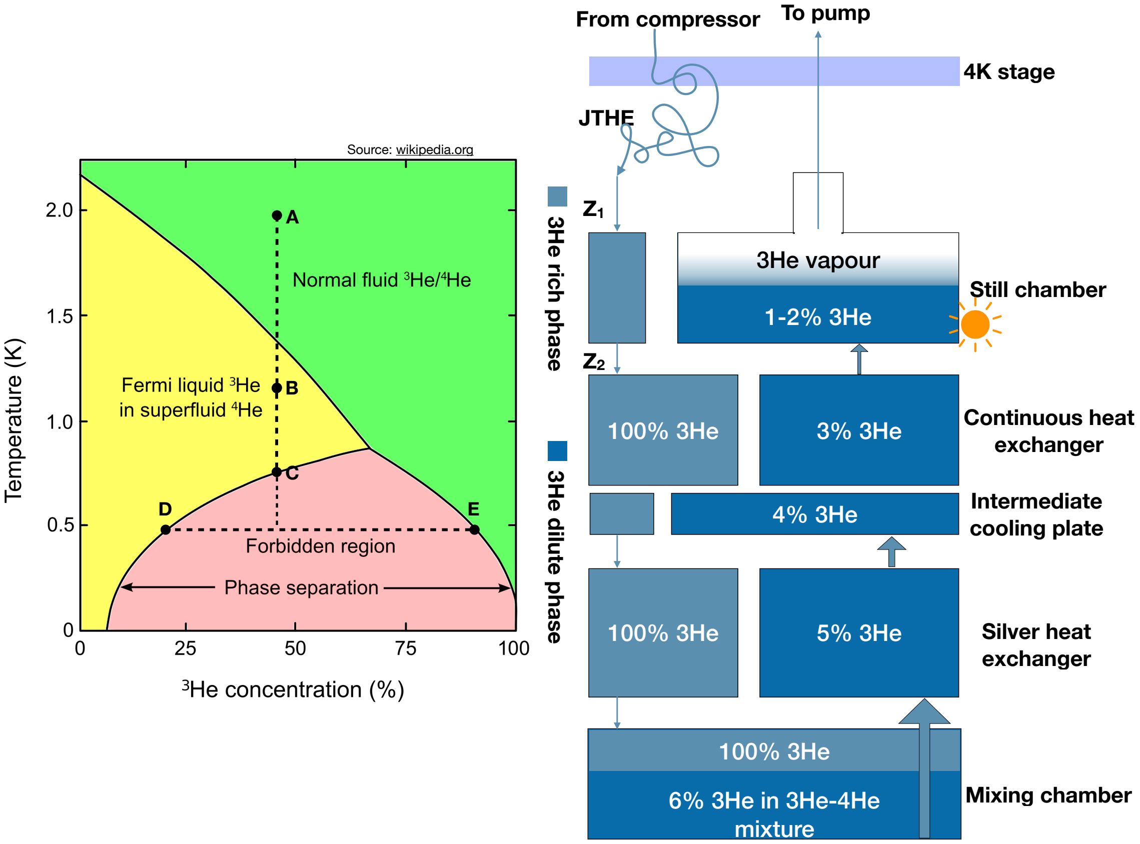
Source: wikipedia.org
Temperature (K)
2.0
1.5
1.0
0.5
0
0
25
50
75
100
³He concentration (%)
A
B
C
D
E
Normal fluid ³He/⁴He
Fermi liquid ³He in superfluid ⁴He
Forbidden region
Phase separation
From compressor
To pump
4K stage
JTHE
Z₁
Z₂
3He rich phase
3He dilute phase
3He vapour
1-2% 3He
Still chamber
100% 3He
3% 3He
Continuous heat exchanger
4% 3He
Intermediate cooling plate
100% 3He
5% 3He
Silver heat exchanger
100% 3He
6% 3He in 3He-4He mixture
Mixing chamber

Fig. 4.4 **Left** phase diagram of liquid 3He and 4He mixture. **Right** schematic of a dilution refrigerator(DR). The percentages are approximated for 0K operation. Commercial DR can reach down to 2 mK base temperature.

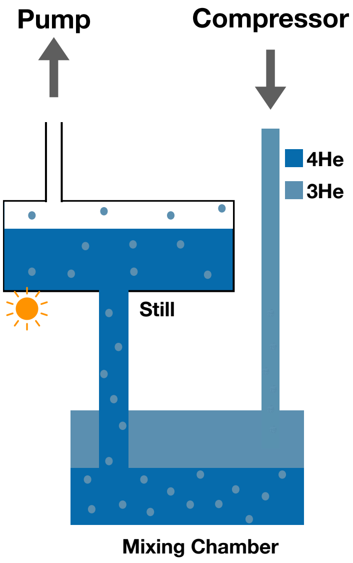
Pump
Compressor
4He
3He
Still
Mixing Chamber

Fig. 4.5 Simplistic model of dilution refrigerator.

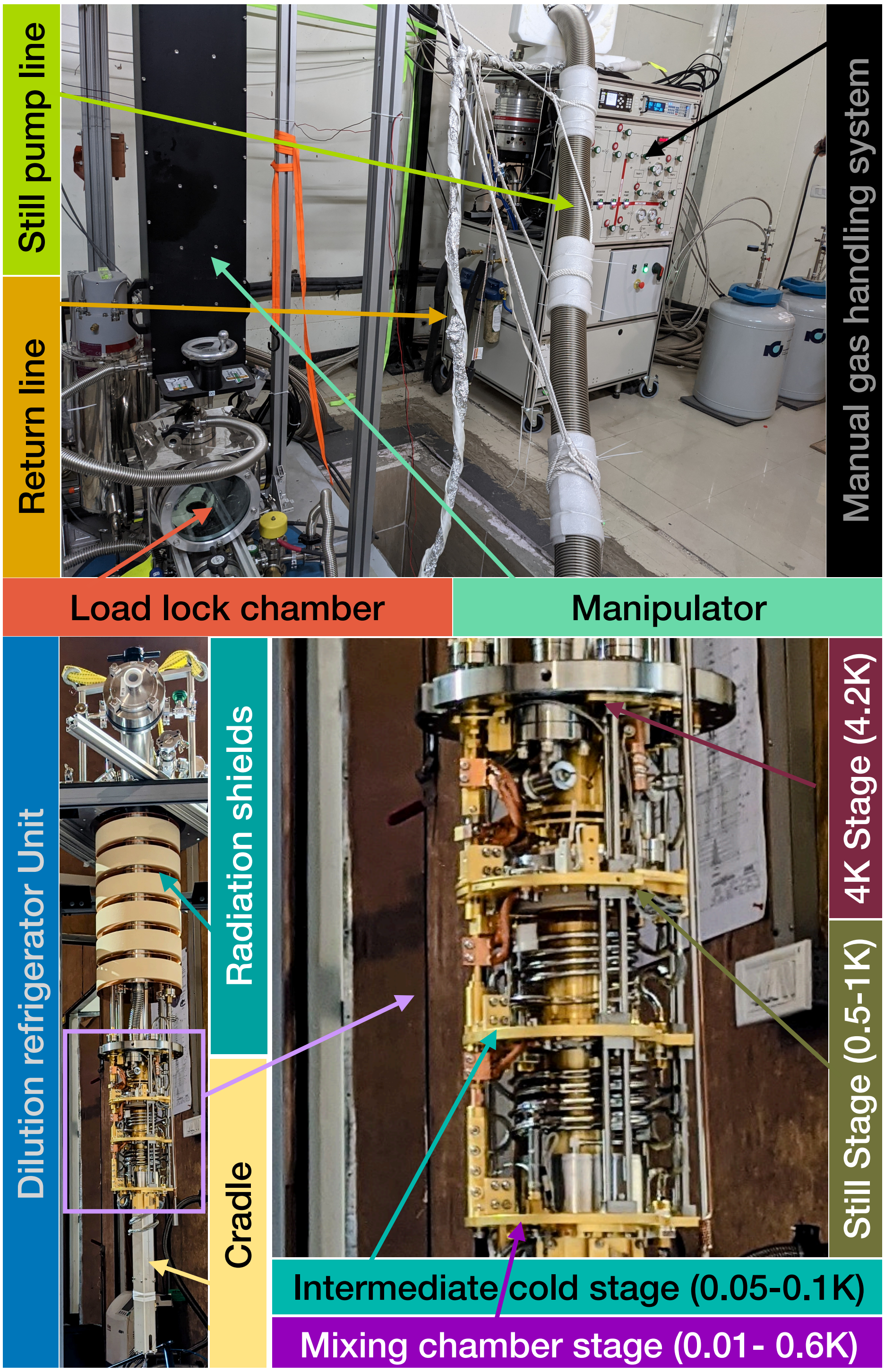
Still pump line
Return line
Manual gas handling system
Load lock chamber
Manipulator
Dilution refrigerator Unit
Radiation shields
Cradle
4K Stage (4.2K)
Still Stage (0.5-1K)
Intermediate cold stage (0.05-0.1K)
Mixing chamber stage (0.01- 0.6K)

Fig. 4.6 A photo of the dilution refrigerator

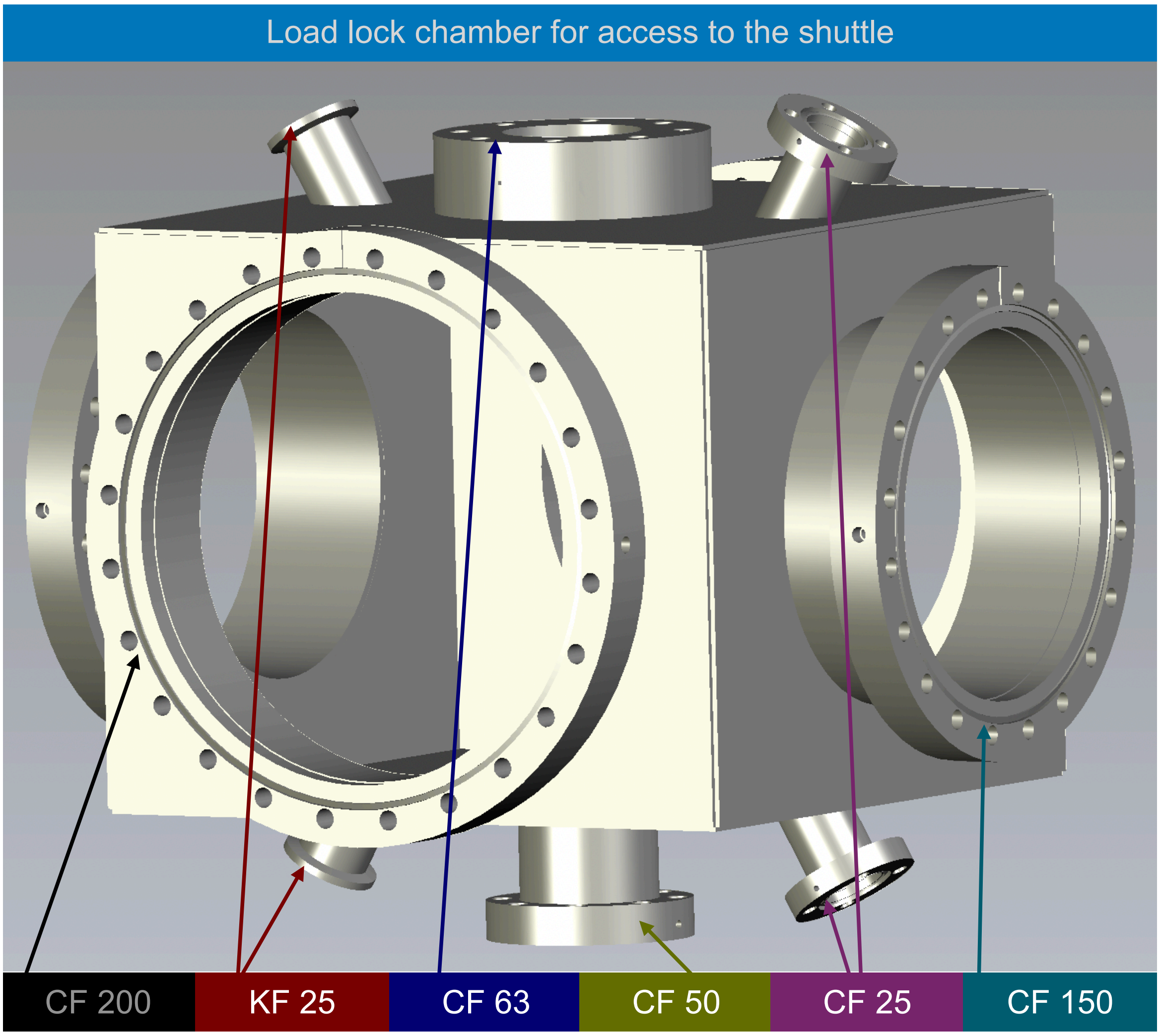
Load lock chamber for access to the shuttle
CF 200
KF 25
CF 63
CF 50
CF 25
CF 150

Fig. 4.7 3D model of the load lock chamber designed using Solidworks. There are two CF 200 windows opposite to each other (one is visible here) and two CF 150 windows opposite to each other (one is visible here). One of these windows is opened for access to the shuttle. CF 50 flange at the bottom is connected to the DR top. The manipulator assembly is connected to the CF 63 flange on top. The rest of the ports are for pumping or pressure gauge attachment.

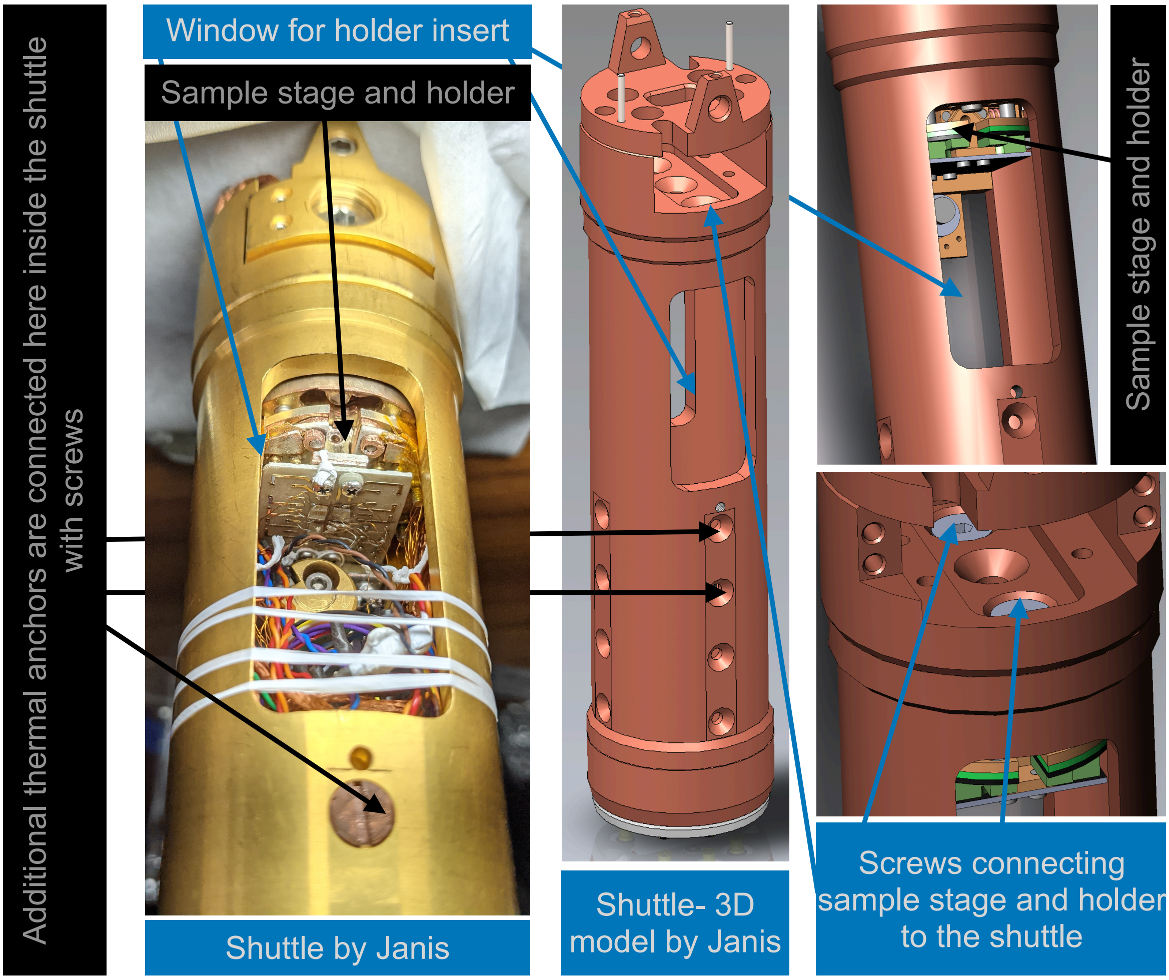
Additional thermal anchors are connected here inside the shuttle with screws
Window for holder insert
Sample stage and holder
Shuttle by Janis
Shuttle- 3D model by Janis
Sample stage and holder
Screws connecting sample stage and holder to the shuttle

Fig. 4.8 Image and 3D model of the shuttle. The sample space inside the shuttle is visible.

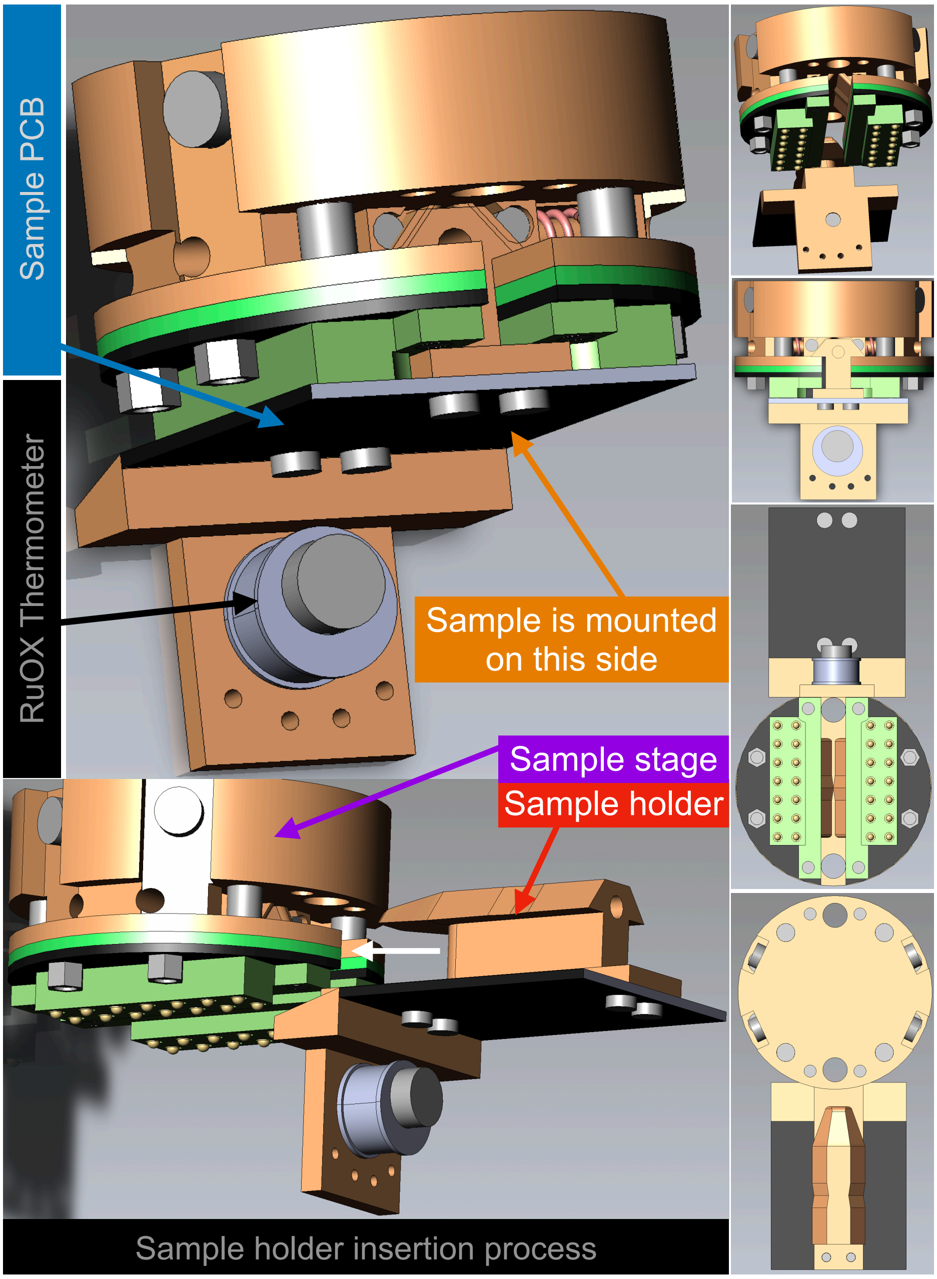
Sample PCB
RuOX Thermometer
Sample is mounted on this side
Sample stage
Sample holder
Sample holder insertion process

Fig. 4.9 3D model of the sample space, designed in solidworks. The sample space has two parts, namely: sample stage and sample holder. The vertical collage of small images on the right hand side represents the sample holder and sample stage relative positions just before the sample holder insertion. The white arrow shows the direction of insertion.

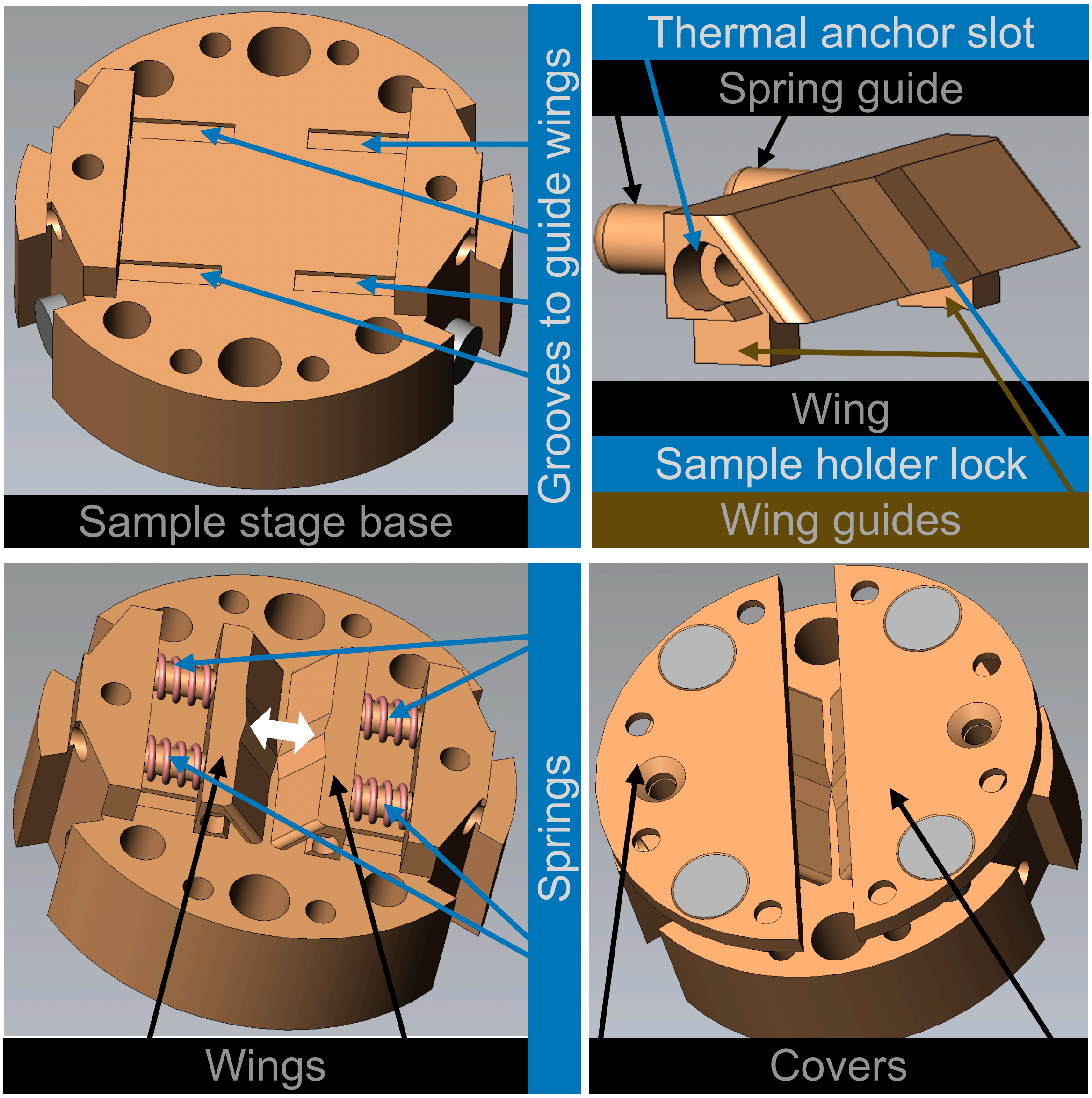
Sample stage base
Grooves to guide wings
Thermal anchor slot
Spring guide
Wing
Sample holder lock
Wing guides
Wings
Springs
Covers

Fig. 4.10 Locking mechanism for sample holder. The white bidirectional arrow shows the movement of wing during the sample holder insertion.

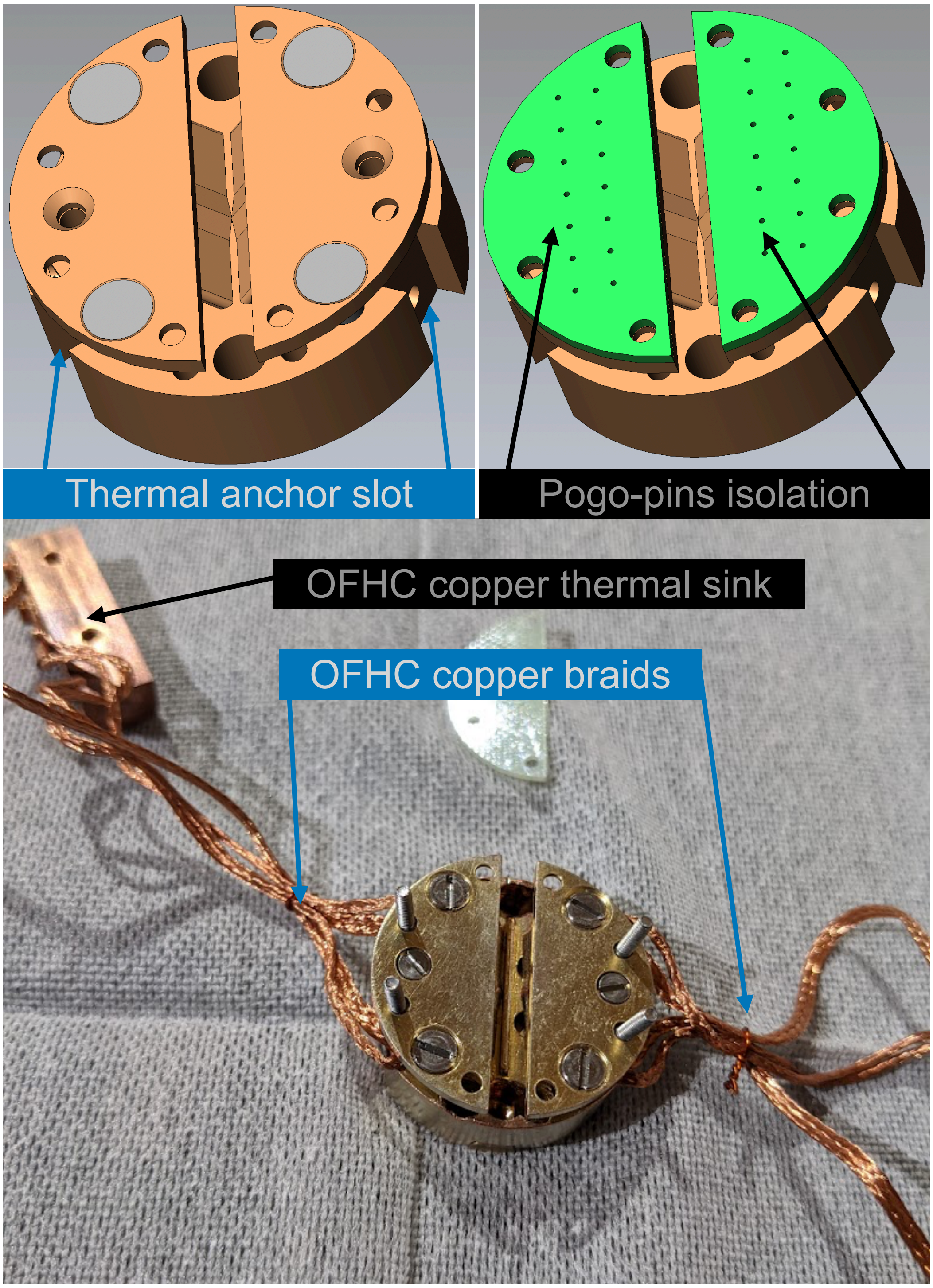
Thermal anchor slot
Pogo-pins isolation
OFHC copper thermal sink
OFHC copper braids

Fig. 4.11 3D model of the sample stage at an intermediate step of the assembly. The image shows the thermal anchors.

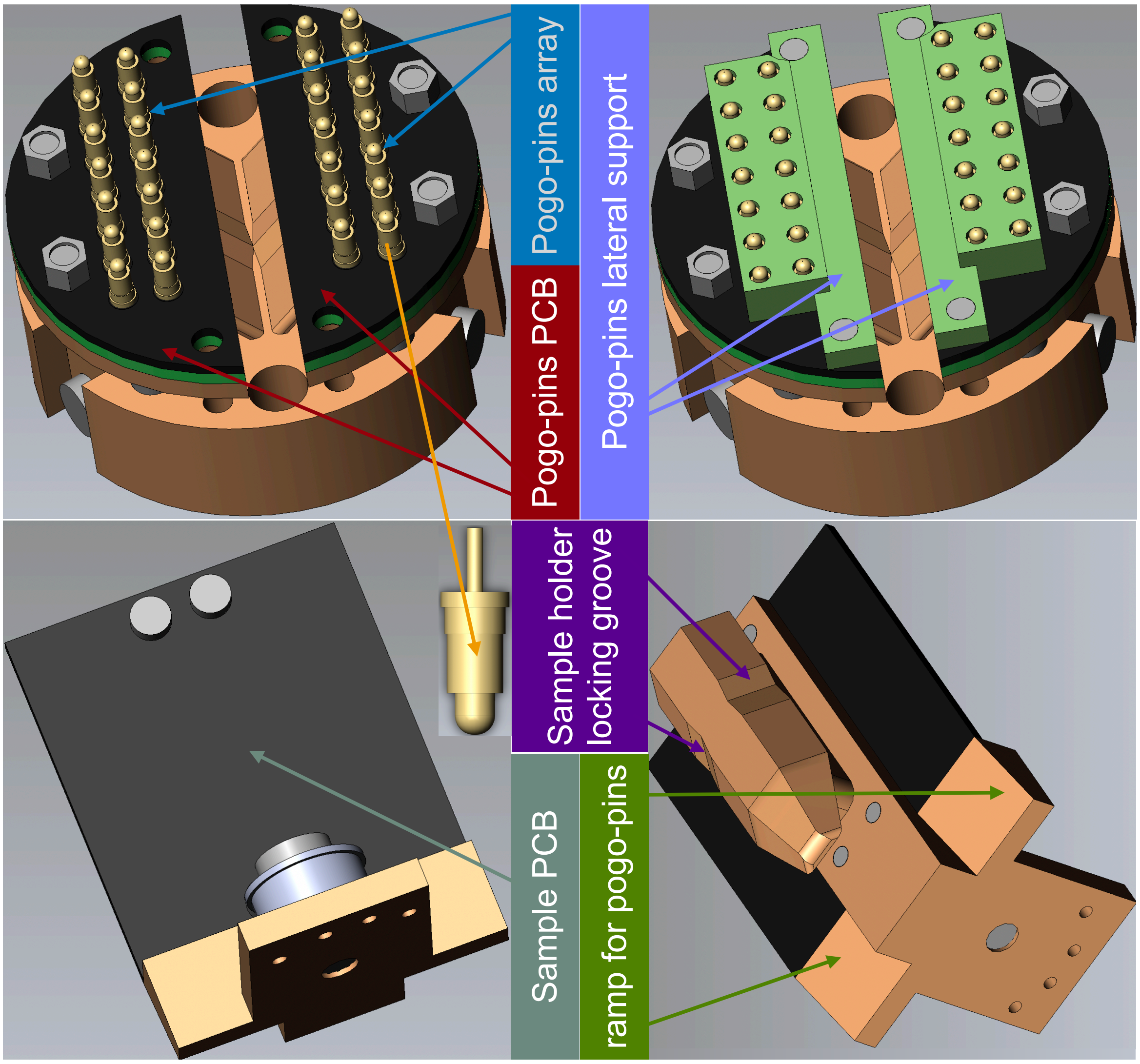
Pogo-pins array
Pogo-pins PCB
Pogo-pins lateral support
Sample holder locking groove
Sample PCB
ramp for pogo-pins

Fig. 4.12 Last step of the sample stage assembly. The zoomed image of the pogo-pin is for the dimensional reference.

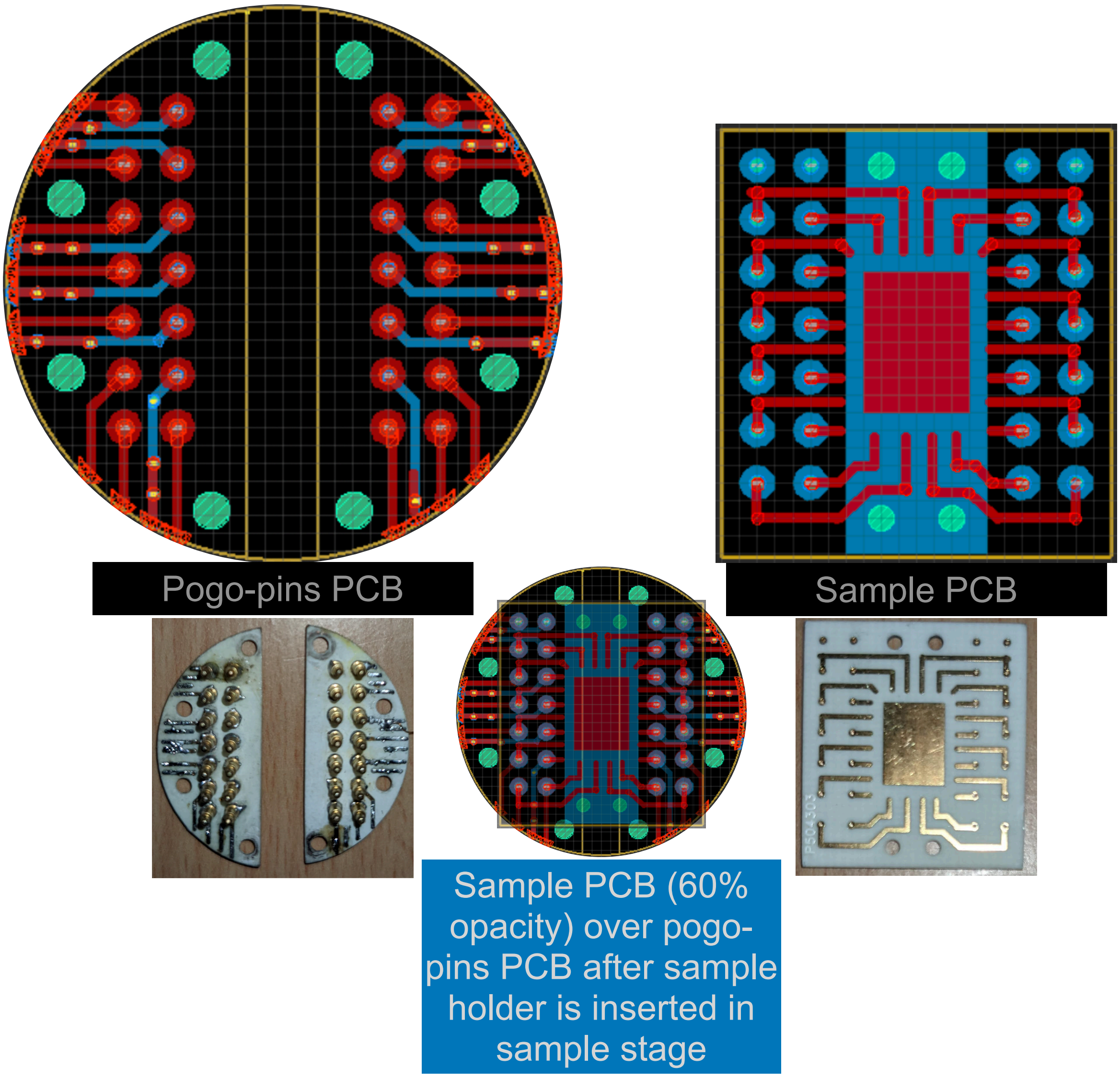
Pogo-pins PCB
Sample PCB
Sample PCB (60% opacity) over pogo-pins PCB after sample holder is inserted in sample stage

Fig. 4.13 The PCB is designed using Eagle CAD. In the design, the color red represents the top copper layer, and the color blue represents the bottom copper layer. The green color represents a through hole. Yellow lines in the design are the boundaries of the PCBs. The images of the PCBs are also shown here.

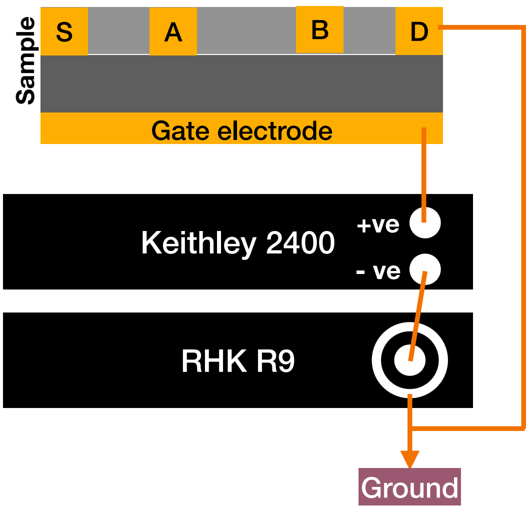
Sample
S
A
B
D
Gate electrode
Keithley 2400
+ve
- ve
RHK R9
Ground

Fig. 4.14 Circuit diagram for gate-dependent measurements. The light and dark grey layers in the sample represent $LaVO_3$ and $SrTiO_3$, respectively. The interface is conducting. S, A, B, and D are the contacts to the interface. S and D stand for source and drain, respectively. A and B are voltage probes.

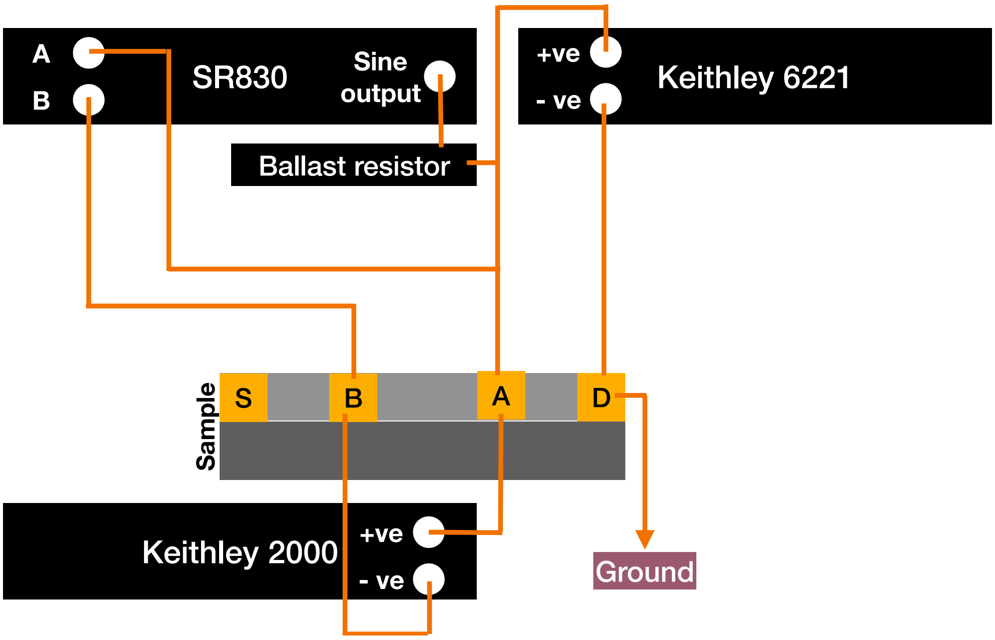
A
B
SR830
Sine output
+ve
- ve
Keithley 6221
Ballast resistor
Sample
S
B
A
D
Keithley 2000
+ve
- ve
Ground

Fig. 4.15 Circuit diagram for sub-surface point contacts Andreev reflection measurements. The light and dark grey layers in the sample represent $LaVO_3$ and $SrTiO_3$, respectively. The interface is conducting. S, B, A, and D are the contacts to the interface and contact A is assumed to be in the ballistic regime.

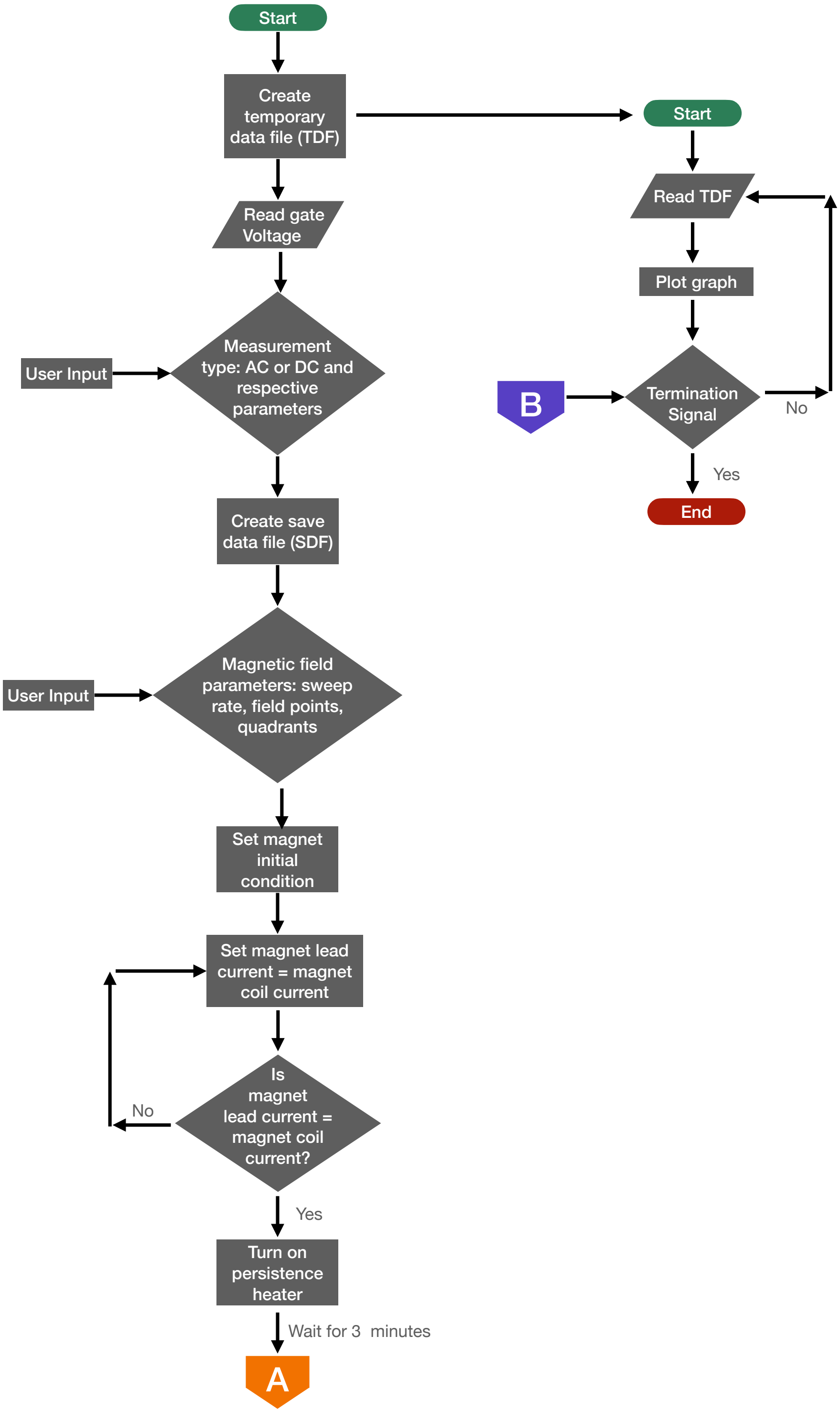
Start
Create temporary data file (TDF)
Read gate Voltage
User Input
Measurement type: AC or DC and respective parameters
Create save data file (SDF)
User Input
Magnetic field parameters: sweep rate, field points, quadrants
Set magnet initial condition
Set magnet lead current = magnet coil current
Is magnet lead current = magnet coil current?
No
Yes
Turn on persistence heater
Wait for 3 minutes
A
Start
Read TDF
Plot graph
B
Termination Signal
No
Yes
End

Fig. 4.16 Logical flow chart of the magneto/ Hall resistance program, part-1

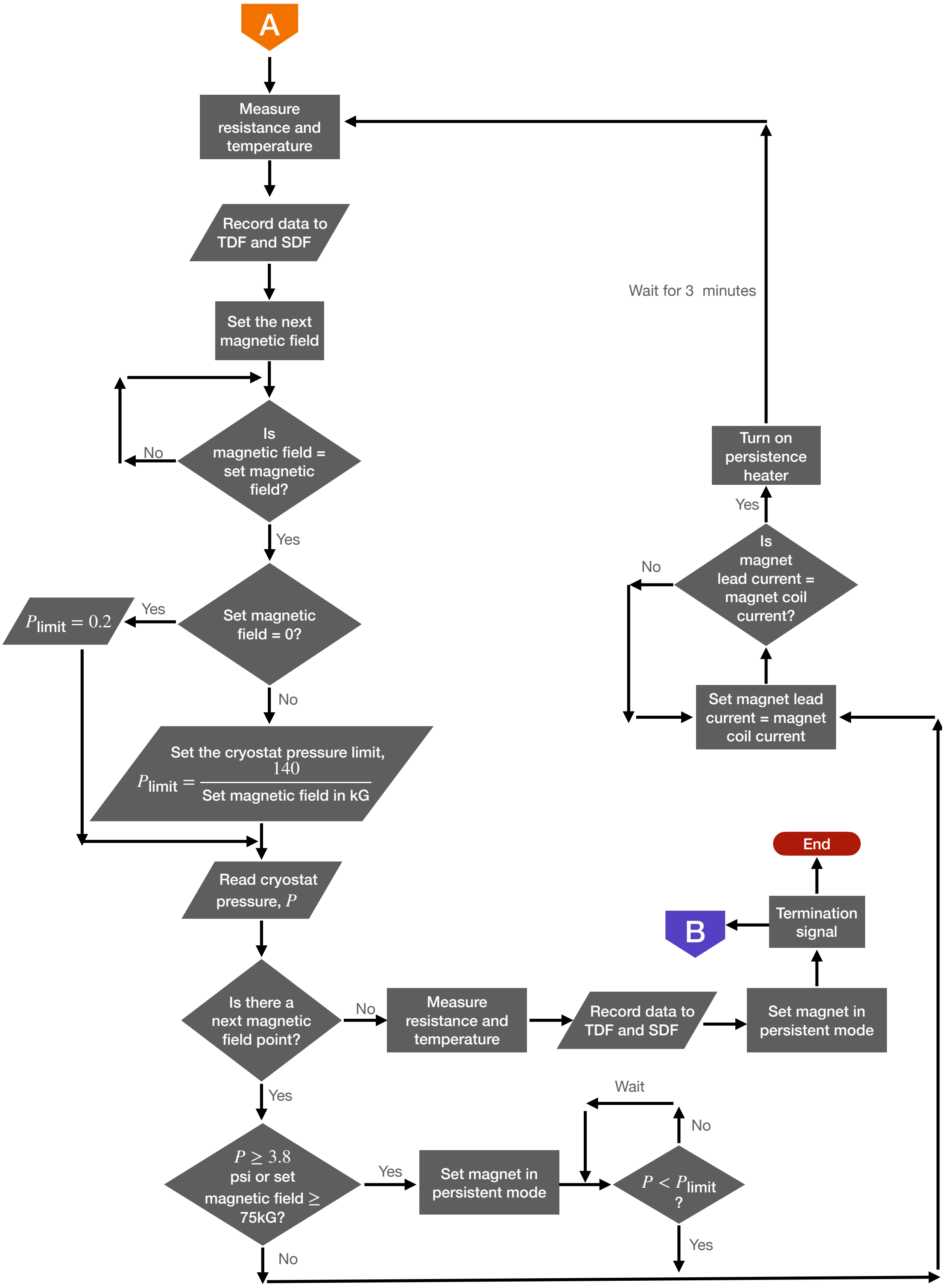
A
Measure resistance and temperature
Record data to TDF and SDF
Set the next magnetic field
Is magnetic field = set magnetic field?
No
Yes
Set magnetic field = 0?
Yes
$P_{\text{limit}} = 0.2$
No
Set the cryostat pressure limit, $P_{\text{limit}} = \frac{140}{\text{Set magnetic field in kG}}$
Read cryostat pressure, P
Is there a next magnetic field point?
No
Measure resistance and temperature
Record data to TDF and SDF
Set magnet in persistent mode
Termination signal
End
B
Yes
$P \geq 3.8$ psi or set magnetic field $\geq$ 75kG?
Yes
Set magnet in persistent mode
$P < P_{\text{limit}}$?
Wait
No
Yes
No
Set magnet lead current = magnet coil current
Is magnet lead current = magnet coil current?
No
Yes
Turn on persistence heater
Wait for 3 minutes

Fig. 4.17 Logical flow chart of the magneto/ Hall resistance program, part-2

Chapter 5

$LaVO_3$/ $SrTiO_3$, Experimental data and discussion

5.1 Introduction

The motivation of investigating $LaVO_3$/ $SrTiO_3$ [001] interfaces is discussed already in chapter 3. From the discussions in chapter 1, we also have an understanding of the temperature range where such interfaces may exhibit measurable quantum phenomena. We carried out magneto-transport measurements on the $LaVO_3$/ $SrTiO_3$ [001] interfaces and discovered that these interfaces host unconventional superconductivity. The onset temperature for the superconducting phase to kick in is about 250 mK. The superconducting transition is broad. We have also observed that the interface is highly disordered where superconducting islands, separated by bad metallic background, are percolatively connected. The experimental data and the conclusions will be discussed in the following sections.

5.2 Sample preparation

To prepare the 2DEG at the $LaVO_3$/$SrTiO_3$ interfaces, our collaborator deposited a thin film of $LaVO_3$ on $SrTiO_3$ by pulsed laser deposition (PLD) using polycrystalline target $LaVO_4$. To get TiO_2 terminated $SrTiO_3$ [001] surface, the $SrTiO_3$ substrate was annealed at 900^0 C for 2 hours in the presence of air. To remove the SrO particles formed on the surface of annealed $SrTiO_3$ substrate, it was then sonicated in deionized water at 60^0 C for 15 minutes. The substrate was further annealed at 900^0 C for 2 hours to improve the quality of TiO_2 terminated step and terrace structure. $LaVO_3$ over a TiO_2 terminated single crystal of $SrTiO_3$ in [001] orientation was grown at 600^0C under $1x10^{-6}$ Torr oxygen partial pressure. $4J/cm^2$

laser fluence was used on the target for the optimum growth. Atomic force microscopic (AFM) images and reflection high energy electron diffraction (RHEED) patterns for the prepared $SrTiO_3$ and the $LaVO_3$ surfaces confirm that both are atomically flat as shown in Fig. 5.1 **b,c,d,e**. The periodic oscillations in the intensity of the specular spot of the RHEED pattern, observed during the growth of $LaVO_3$ films, suggest a layer-by-layer growth. Fig. 5.1. **f** shows such a pattern during a 50 mono layers of $LaVO_3$ growth. Fig. 5.1 **g** shows the sheet resistance of that interface as a function of temperature. It decreases as the temperature is reduced, suggesting a metallic behavior. The *inset* of Fig. 5.1 **g** depicts the Hall measurements at room temperature. The hall data implies n-type carrier is present at the interface (please refer to Fig. 5.1 caption for more details). $LaVO_3$/$SrTiO_3$ interfaces are known to conduct with observed anomalous magneto-transport [6; 32] and optical properties [37]. We have controlled the conducting properties of these interfaces by electrical gating (from the bottom of the $SrTiO_3$ substrate), which further supports the fact that the conducting phase is not spread throughout the bulk. We have carried out our ultra-low temperature measurements on two interfaces: $LaVO_3$(50 uc)/$SrTiO_3$ and $LaVO_3$(100 uc)/$SrTiO_3$.

5.3 Discovery of unconventional superconductivity at $LaVO_3$/$SrTiO_3$ interfaces

$LaVO_3$(50 uc)/$SrTiO_3$ was our choice of interface for the initial ultra-low temperature characterization.

5.3.1 Methods

The $LaVO_3$/ $SrTiO_3$ heterostructure was mounted on the sample PCB and electrically connected to the PCB tracks by wedge wire bonding using 1 mil thin Aluminum wires. The sample holder then is clamped to the sample stage and transferred into the Dilution refrigerator using the vacuum manipulator. The details of this process and the instrumentation are discussed in the previous chapter. The sample was then cooled to the base temperature (28 mK). Sample connections were made in standard Hall geometry, where bonding wires were placed in a specific position on a 5x5 mm sample. A conventional four-probe method was used for all the resistance (R) measurements. The AC resistance measurements were performed using an SR830 lock-in amplifier. The temperature was controlled using the home-built heater in the sample space. The RuOx resistive thermometer in the sample space was read by Lakeshore 372 controller for temperature values (T). For DC voltage (V) vs current (I)measurements, Keithley 6221 current source and Keithley 2000 multimeter were

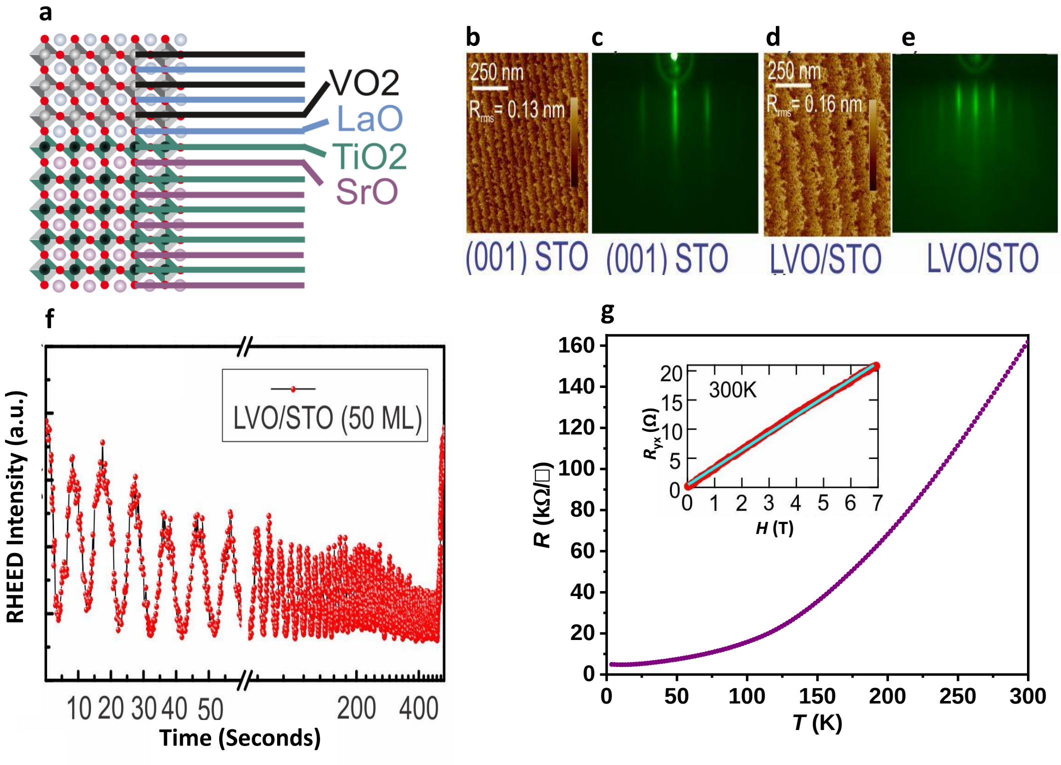

Fig. 5.1 **Preparation of 2DEG at the $LaVO_3/SrTiO_3$ interfaces: a** The schematic of the $LaVO_3/SrTiO_3$ s. **b**, **c** the AFM image and RHEED pattern of the (001) $SrTiO_3$ before deposition, respectively. **d**, **e** the AFM image and RHEED pattern for the $LaVO_3/SrTiO_3$ surface after deposition, respectively, showing a smooth crystalline growth of film. **f** RHEED oscillations for the films grown at $4 J/cm^2$ laser fluence as a function of time indicate the controlled deposition of $LaVO_3$ film over (001) $SrTiO_3$ substrate. **g** The sheet resistance of the sample. The *inset* shows the Hall measurement of the $LaVO_3/SrTiO_3$ interface at 300K. R_{yx} instead of R_{xy} was measured here, which resulted in an opposite slope in Hall measurement for the n-type carrier.

used. For Point Contact Andreev Reflection (PCAR) spectroscopy SR830 lock-in amplifier, Keithley 6221 current source and Keithley 2000 multimeter were used as shown in Fig.4.15. The SSPCARS measurement is discussed in 4.6

For all the AC measurements, a current of 100 nA at 789 Hz was sent through the sample, and the voltage drop was measured by the lock-in amplifier. The time constant of the lock-in amplifier was kept at 300 ms. A proper sensitivity protocol for the lock-in amplifier was maintained. For the temperature-dependent measurements, we increased the heater current in the steps of $2\mu A$ while waiting for 17 seconds at each step for the sample to thermalize before measuring the voltage drop across the sample. Sample temperature was swept from 28 mK to 500 mK in $\sim$ 9 hours. The $V-I$ data was recorded in the steps of 0.04 μA. The waiting time at each step was 3 seconds.

5.3.2 Data, analysis and discussions

Fig. 5.2 **a** represents the resistance (R) vs. temperature (T) curve. The feature of this curve indicates a superconducting transition onset at about 250 mK. The transition is seen to be broad, which completes below 130 mK. With an increasing magnetic field, the transition temperature monotonically goes down, as expected for a superconductor. The superconducting transition disappears at a magnetic field H_{c2} of 4.5 kG. Using the clean limit relationship (equation 2.37) for a type -II superconductor, we found that the coherence length of the superconducting state $\xi \sim 28$ nm. For a typical perovskite oxide 2DEG, the effective thickness of the superconducting layer is much smaller [17], and hence it is rational to surmise that the LaVO3/SrTiO3 interfaces host two-dimensional superconductivity. *Inset* of Fig. 5.2 **a** shows $H_C - T_C$ phase diagrams derived from the $R-T$ data.

The T_C was defined as a temperature below the superconducting transition onset where the resistance drops to $x\%$ of the normal state. We have plotted $H_C - T_C$ for $x = 85, 50$ and 10 respectively. For all the cases, the phase diagram shows approximately a linear dependence which was earlier seen in certain other 2D superconductors as well [38]. For the grey horizontal line in Fig. 5.2 **a** crossing through the $R-T$ curves, all the intersection points represent 85% of normal state resistance for the respective curves.

The error (*err*) in T_C is calculated from the spread in the superconducting transition along the temperature axis in the $R-T$ data. After smoothing and differentiating the $R-T$ data w.r.t. T, we obtain curves (as shown in Fig. 5.3 **a**) for each $R-T$ taken at different magnetic fields. The peak represents the onset of the superconducting transition. The spread (σ as shown in Fig. 5.3 **a**) of the transition is defined as the difference in T from the peak position to where the half-maximum occurs on the right-hand side of the peak. $\pm 5\%$ of σ for each $R-T$ data is taken as the error in T_c. For higher magnetic fields, the peak in dR/dT could not be captured within the measurement limit. For such data, the magnitude of *err* was approximated by extrapolating the same at the preceding magnetic field values. As shown in Fig. 5.3 **b**, *err* for different lower field values are fitted linearly. Using the parameters for this fit and taking the applied field as the independent variable, we extracted errors in T_C for higher field values.

We measured the $V-I$ characteristics in a four-probe measurement geometry (Fig. 5.2 **b**) at 28 mK, deep in the superconducting state, where we found a signature of critical current and monotonic suppression of that with increasing magnetic field. This further confirms our discovery of superconductivity at the $LaVO_3/SrTiO_3$ interfaces. It should be noted that the superconducting phase detected at the $LaVO_3/SrTiO_3$ interfaces is fragile in nature. This could be due to the formation of individual superconducting islands connected through percolative paths. The system as a whole becomes slightly resistive ($\sim 10\Omega$) even at very low currents of $\sim$ 50 nA and at magnetic fields as small as 100 Oe.

In chapter 3, we already have seen that the partial band structure calculation of $LaVO_3$/SrTiO3 suggests that not only this interface has multiband carriers (Ti(d) and V(d) bands cross the Fermi energy) but also hosts spin-polarized carriers. Therefore, two key features, namely the existence of multiple bands at the Fermi energy and the finite magnetic moment of the V electrons in the system, make the $LaVO_3/SrTiO_3$ interface a rich electronic system. Therefore, the impact of such unique effects on the emerging superconducting phase warrants detailed spectroscopic investigation. In this context, we note the similarities with the cuprate superconductors where the parent materials are antiferromagnetic Mott insulators (like $LaVO_3$), and in the cuprates, the superconductivity obtained upon doping are unconventional in nature [39].

One significant difficulty in directly probing the superconducting energy gap of the oxide 2DEGs is that the superconducting phase hides underneath an insulating layer. This makes standard transport spectroscopic tools like scanning tunneling spectroscopy and point-contact spectroscopy extremely challenging. In this work, we have created sub-surface metallic point contacts using wire-bonded junctions (of Al wires) with the interface and performed soft point contact Andreev reflection spectroscopy on the $LaVO_3/SrTiO_3$ interfaces to directly probe the superconducting energy gap and the sub-gap states, if there is any. In Fig. 5.4 **a**, we present a representative point-contact Andreev reflection spectrum along with its temperature dependence from 28 mK to 250 mK.

Before discussing the data on $LaVO_3/SrTiO_3$, let us first briefly recall from the chapter 2 the spectral features expected due to Andreev reflection from point contacts between normal metals and conventional (s-wave, BCS) superconductors. When the barrier potential is zero ($Z = 0$), the finite temperature differential conductance (dI/dV) spectra should be more or less flat below the superconducting gap [40]. For non-zero barriers ($Z \neq 0$), two peaks in dI/dV vs. V appear at $\pm\Delta/e$, where Δ is the superconducting energy gap and e is the charge of a single electron (discussed in section 2.5). In some cases, additional spectral broadening can be seen [41] due to finite quasiparticle lifetime and certain inelastic scattering processes under the point contact. No other spectral features are expected.

On the other hand, in point contact spectra involving superconductors with non-s-wave or mixed angular momentum gap-symmetry, for $Z \neq 0$, sub-gap spectral features coexisting with the double-peak structure may also be present [42; 43]. In Fig. 5.4 **a**, we find that at

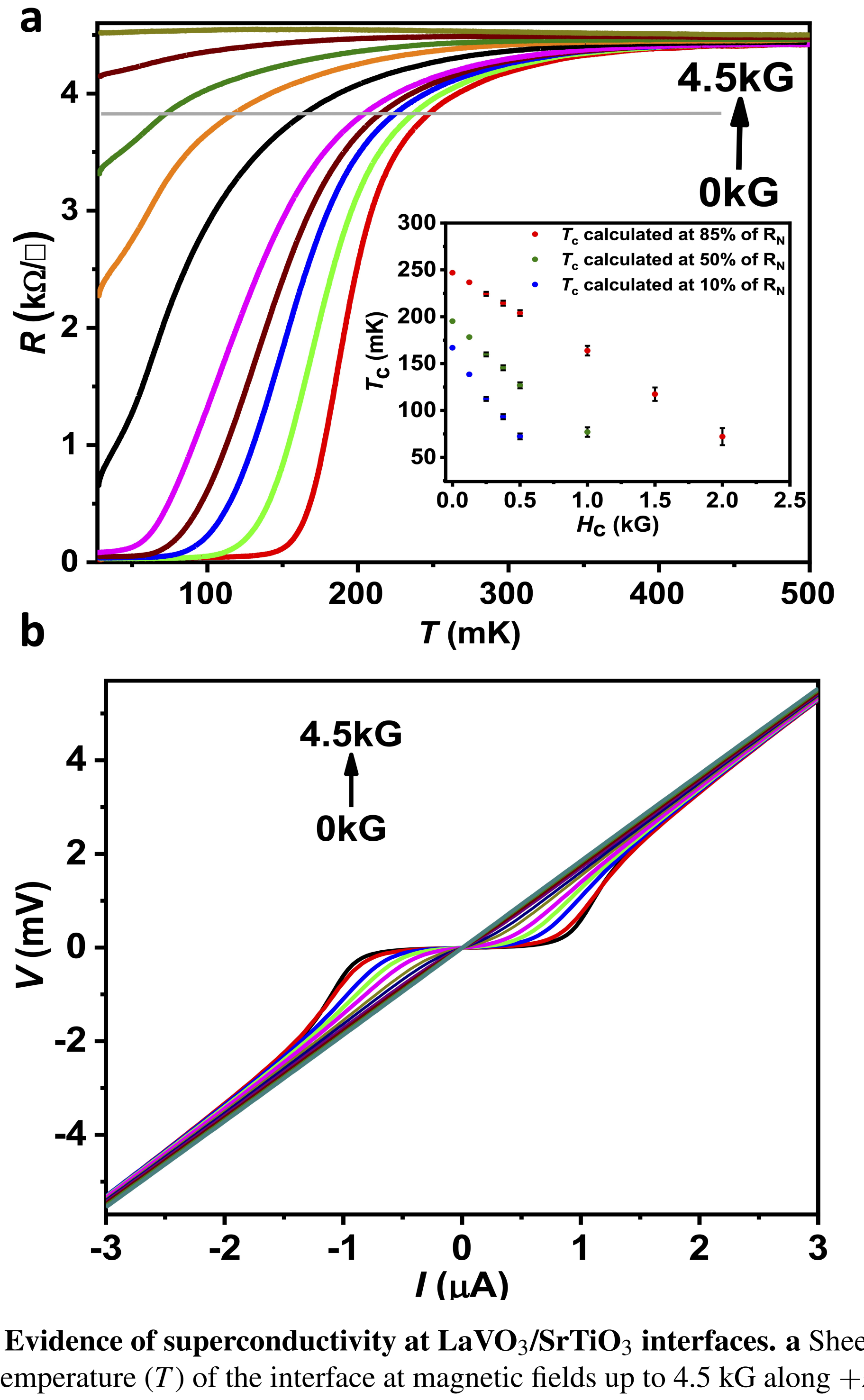

Fig. 5.2 **Evidence of superconductivity at LaVO$_3$/SrTiO$_3$ interfaces. a** Sheet resistance (R) vs. temperature (T) of the interface at magnetic fields up to 4.5 kG along $+\hat{z}$ (vertically up). **b** V vs. I characteristics at magnetic fields up to 4.5 kG along $+\hat{z}$. The *inset* in **a** shows $H_c - T_c$ phase diagram.

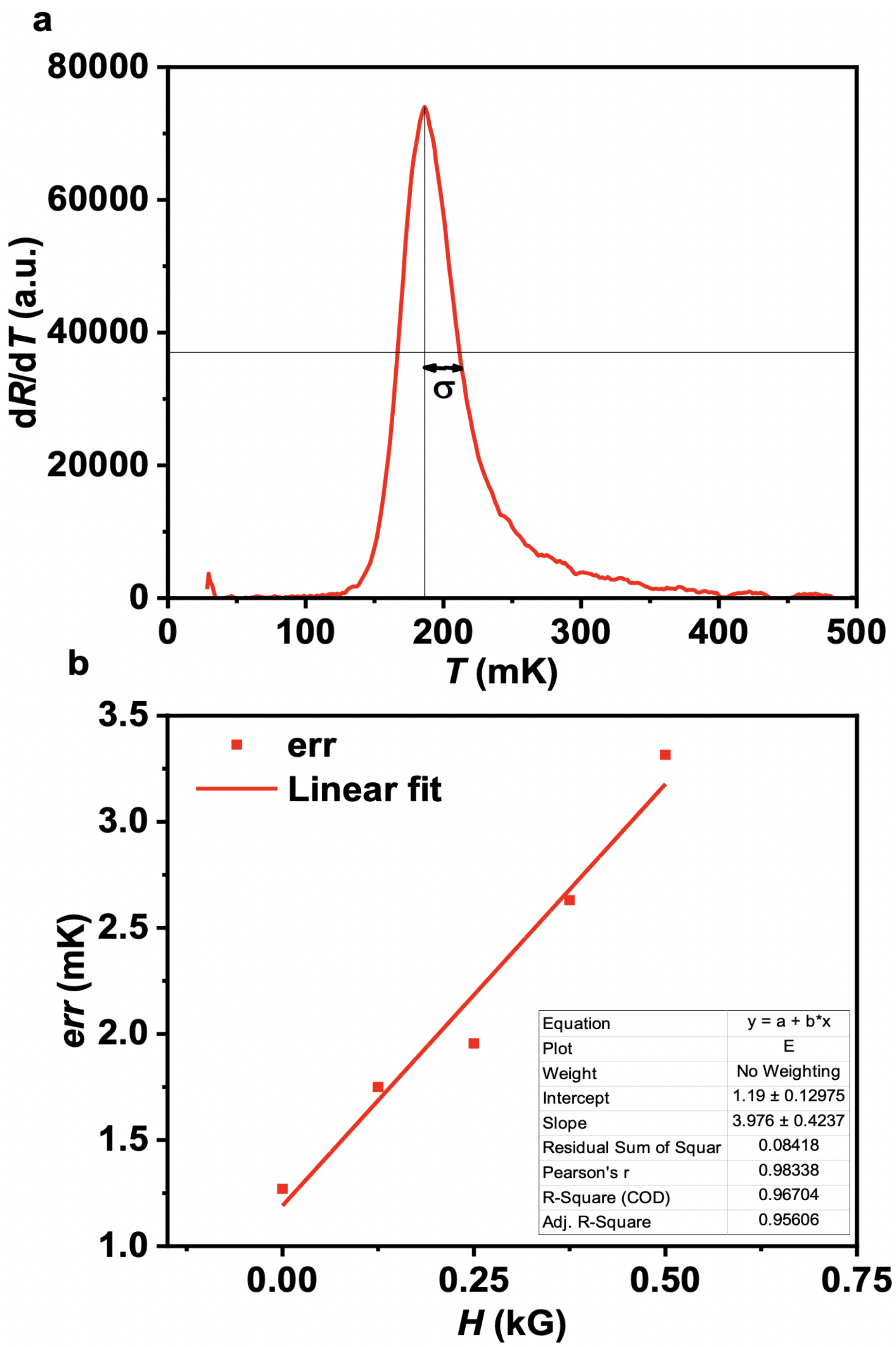

Fig. 5.3 **a** dR/dT vs T derived from the R-T data taken at 0 kG for the superconducting state. **b** Calculated error values for T_C measured at different field. The inset shows the parameters for the linear fit.

the lowest temperature, the dI/dV spectrum shows a shoulder around 250μV followed by a peak at zero-bias. With increasing temperature, all the spectral features, along with the peak at zero bias, undergo suppression. Notably, the energy scales where all such features appear are also relatively larger than expected for a conventional superconductor. All these collectively suggest a clear deviation from conventional superconductivity.

Before analyzing such data, it is most important first to rule out the possible artifacts that may give rise to similar spectral features. Earlier it was shown by Kumar and Sheet [44] that anomalous features might emerge in point contact experiments involving superconductors if the point contacts are far from the ballistic regime. In such a scenario, within a multi-constriction model, the authors showed that if some constrictions have very low critical currents, a pronounced zero-bias conductance peak may also emerge. In such a situation, it is most important first to confirm that the contacts are either in the ballistic or in the diffusive regime of transport. Usually, the spectra from the non-ballistic transport also give rise to conductance dips in superconducting point contacts [45]. In our experiments, we have rejected all such spectra showing conductance dips (examples are shown in Fig. 5.6) and considered only those free from such artifacts for our analysis. Furthermore, we have noted the temperature dependence of the normal state resistance as a function of temperature, which remains almost unchanged as expected for ballistic point contacts. Finally, we have employed the Wexler's formula ($R_{PC} = \frac{2h/e^2}{(ak_F)^2} + \Gamma(l/a)\ \frac{\rho(T)}{2a}$, where $\Gamma(l/a)$ is a numerical factor close to unity.) to find the contact diameter which was found to be approximately 4 nm. This is smaller than the typical mean free path measured on $LaVO_3/SrTiO_3$ interfaces [46]. Therefore, all the arguments given above collectively suggest that the reported experiments have been performed in the ballistic (or diffusive) regime where energy-resolved spectroscopy is possible.

Regarding our data (Fig. 5.4 **a**), we first note that the ratio of the low-bias and high bias dI/dV in case of the point contact is more than 2, the maximum value expected due to Andreev reflection from a conventional superconductor. To understand this deviation, we compared our experimental spectra with the calculated spectra for superconductors with non-s-wave order parameter symmetries published in the literature. We found that strikingly similar spectral features as ours appeared in the calculated dI/dV vs V spectra for a superconductor with mixed angular momentum symmetry [47]. In the same work, it was argued that the zero bias peak on top of a broader Andreev reflection-dominated zero bias feature, along with a large low-bias conductance enhancement, could be a result of mixing of a regular s-wave order parameter (Δ_s) with a triplet (Δ_p) order parameter. The relative contribution from the triplet state is smaller ($\Delta_s > \Delta_p$). In such a case, when a magnetic field suppresses the non-s-wave component, a double peak structure should prevail. We indeed found that in our case the zero-bias peak was suppressed by an increasing external magnetic field, the spectra first formed a flat region around $V = 0$ (Fig. 5.5) and eventually led to a double-peak feature (*inset* of Fig 5.4 **b**). Beyond this point, the features associated with superconductivity got further suppressed gradually and eventually disappeared at a field of 2.7 kG. As suggested by the spectroscopic experiments, the possibility of a triplet component in the order parameter is consistent with the fact that the V electrons, carrying non-zero magnetic moments, populate the Fermi energy of the 2DEG between $LaVO_3$ and $SrTiO_3$. The s-wave and the non s-wave components might emerge in the two distinct bands in the momentum space.

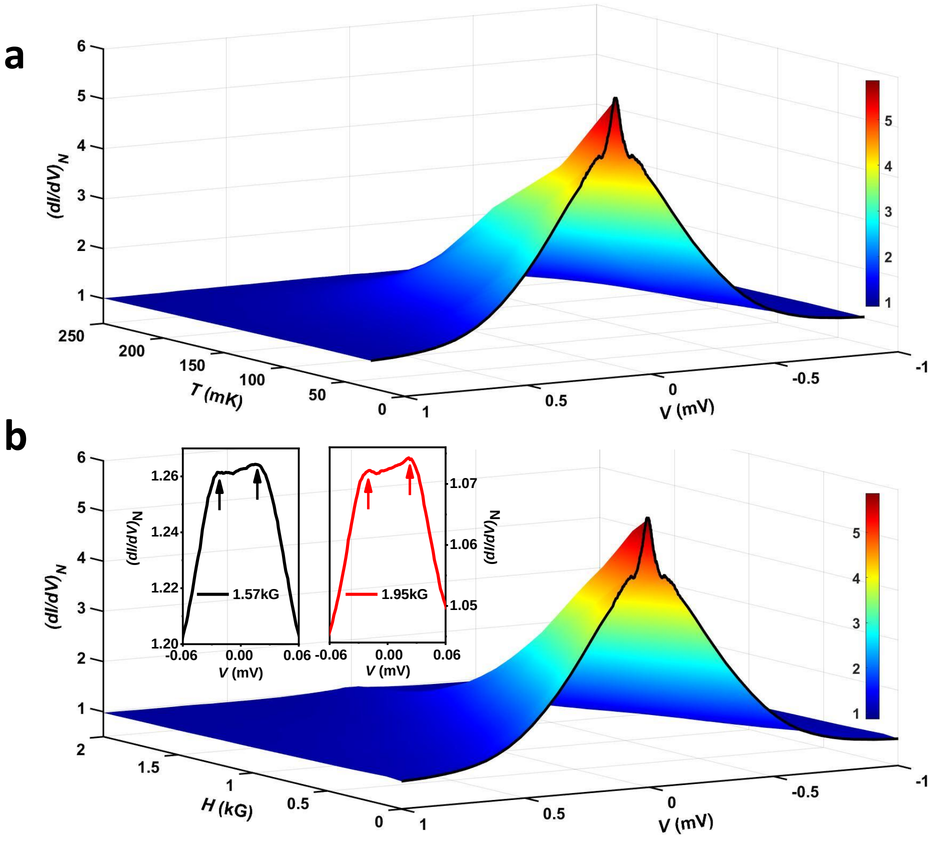

Fig. 5.4 **Indication of unconventional superconductivity: a** Temperature dependence of normalized differential conductance $\frac{dI}{dV}$ *vs* applied DC bias (V). The lowest temperature and zero field data is shown as a black line (in both **a** and **b**). **b** Magnetic field dependence of normalized differential conductance $\frac{dI}{dV}$ *vs* applied DC bias (V). The *inset* shows a double peak feature around $V = 0$ at higher magnetic fields in 2D plots.

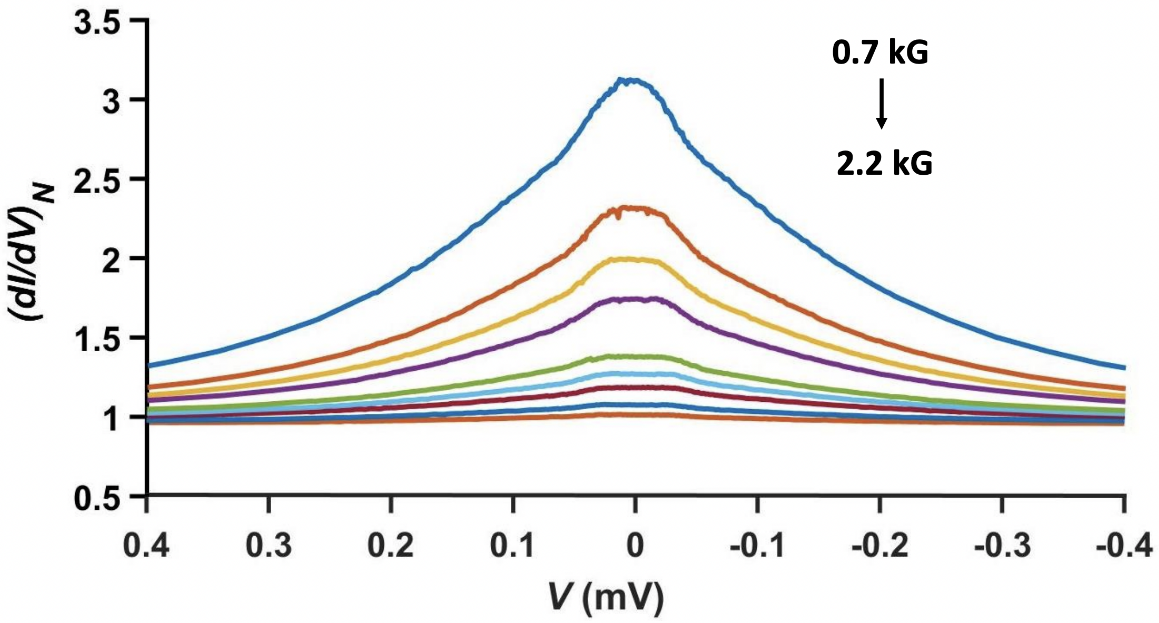

Fig. 5.5 PCS spectra for the ballistic point contact at higher magnetic field values showing the zero bias feature becoming flatter with increasing magnetic field.

5.4 $LaVO_3/SrTiO_3$ interface: a ferroelectric controlled superconductor

In the previous section, we discussed that the $LaVO_3/SrTiO_3$ interface exhibits superconducting transition but never reaches a zero resistance state. The $V-I$ data also demonstrates finite resistivity beyond the superconducting transition of the interface. This suggests that the interface has a mixed phase (normal and superconductor) and warrants further investigation. We have performed gate-dependent measurements (The circuit diagram is shown in Fig. 4.14) to explore the normal phase of the mix while the superconducting phase is deep in the superconducting state. We have performed these measurements on $LaVO_3$(100 uc)/$SrTiO_3$ interfaces.

5.4.1 Methods

The sample mounting and loading mechanism were the same as discussed in the last section. We have performed electronic transport/magneto-transport measurements at different gate voltages. The gate voltage was swept from one point to the next at 50 mV/min. At each gate voltage, we waited 30 minutes to stabilize the charge distribution in the sample. The resistivity during this waiting period for each gate voltage never changed appreciably, which

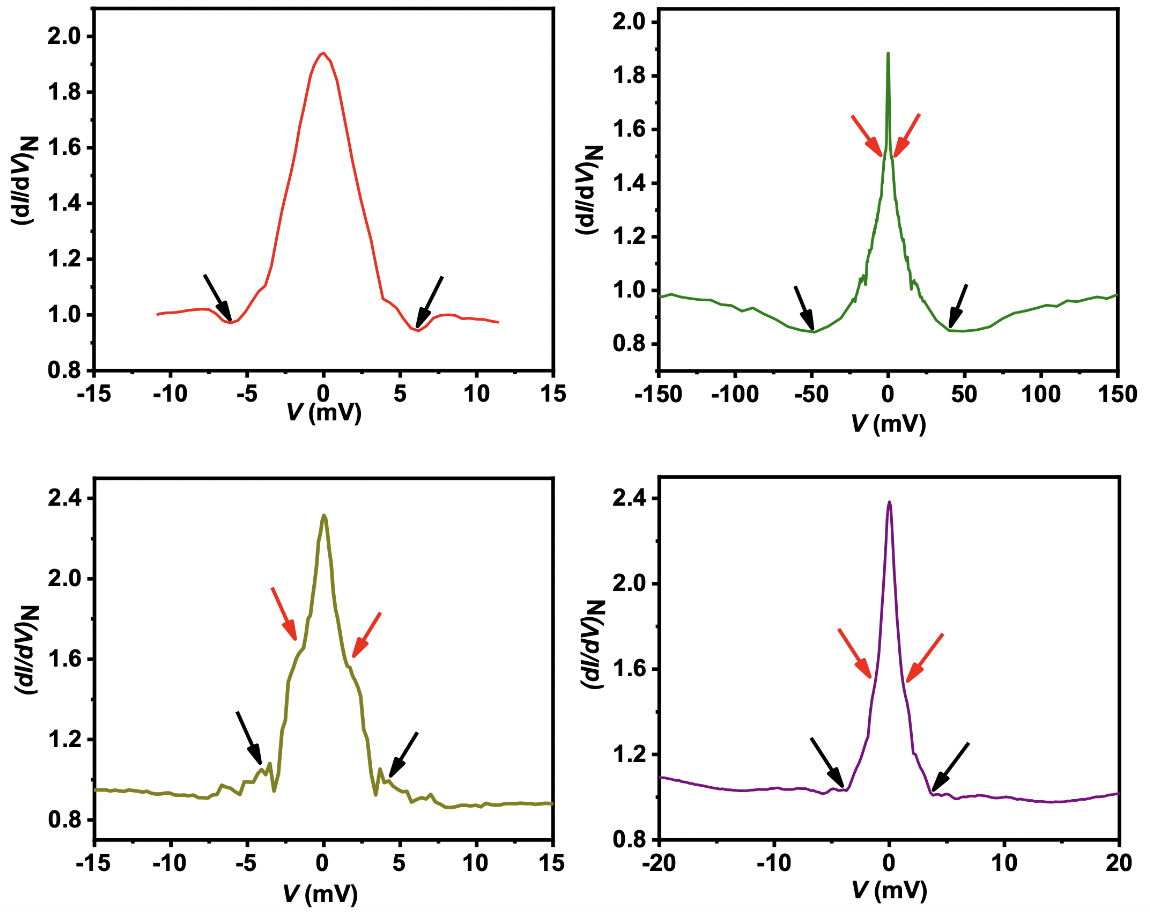

Fig. 5.6 Spectra showing critical current dips(indicated by black arrows) on different point contacts. In these spectra, the signature of the low-bias slope change(indicated by red arrows) are also seen. This could be due to non-zero contribution of Andreev Reflection in an intermediate regime.

confirms the optimization of our gate sweep parameters. However, to be extra careful to not perform measurements at a non-equilibrium charge distributions within the sample, we have always waited 30 minutes after the gate voltage reached the set value. We have measured $R-T$ (Fig. 5.8) and $V-I$ (Fig. 5.9) at each gate point. $R-T$ and $V-I$ measurement methods are discussed in section 5.3. For some of the points, we measured Hall resistance. We have used Hall geometry. We supplied 1.5μA current through the sample, and the output was measured by the SR830 lock-in amplifier. The magnetic field sweep rate on the magnet power supply was set at 25 G/sec. However, the sweep rate was even slower as our maximum data point interval was 1kG, and for the PID controller in the power supply, the interval was within the error limit where the maximum control was required. The magnetic field sweep rate does not change the Hall data until there is noticeable Eddy current heating in the sample space. We have never gone to that limit. We have continuously monitored the leakage current from the gate electrode to the interface and never allowed a leakage current ≥ 1 nA.

5.4.2 Data, analysis and discussion

To explain the non-zero resistance below the superconducting transition, a model, as shown in Fig. 5.7, can be considered where superconducting islands are separated by a bad metallic background. For superconducting transition for this model, three possible scenarios can be expected, as described below.

1. The inter-island distances are so small that electrons from different islands can form Cooper pairs. In such a case, phase coherence among all the islands should be established, and the islands should act as a whole superconductor ignoring the non-superconductor interlinks. In such a scenario, zero resistance is expected below superconducting transition, given that the superconducting volume fraction is large enough.

2. The inter-island distances are small but not too small to maintain inter-island phase coherence, but the superconducting wave functions of different islands overlap to result in a zero resistance state. Josephson junction-like features are expected in such a scenario.

3. The inter-island distances are too large for the superconducting wave functions to overlap. Inter-island phase coherence is also not possible. Below the superconducting transition, non-zero resistance is expected in this case.

From Fig. 5.8, it is evident that both the normal state resistance and the superconducting state resistance vary systematically with gate voltage (V_G). For $+ve$ and $-ve$ gate voltages, the resistance drops or increases respectively with higher V_G magnitude. The T_C, however, does not change noticeably. For similar measurements on LaALO$_3$/SrTiO$_3$, the T_C had very prominent gate dependence, and the observed change in T_C was $\sim$ 200 mK. This phenomenon was due to the change in carrier density, n, with gate voltage. In our case, the resistance at both normal and superconducting states was more responsive to the gate than T_C. This also suggests that the LaVO$_3$/SrTiO$_3$ interfaces have different mechanisms, controling superconductivity, and the effective n at the interface possibly does not change.

To ascertain that the carrier density does not change gate dependent Hall measurement is performed (Fig. 5.9). The Hall data certainly indicates no noticeable change in n with V_G. In previously reported works in LaAlO$_3$/SrTiO$_3$ interfaces, in the application, very high V_G (of the order of 100V) n was observed to vary a few times of the natural value.

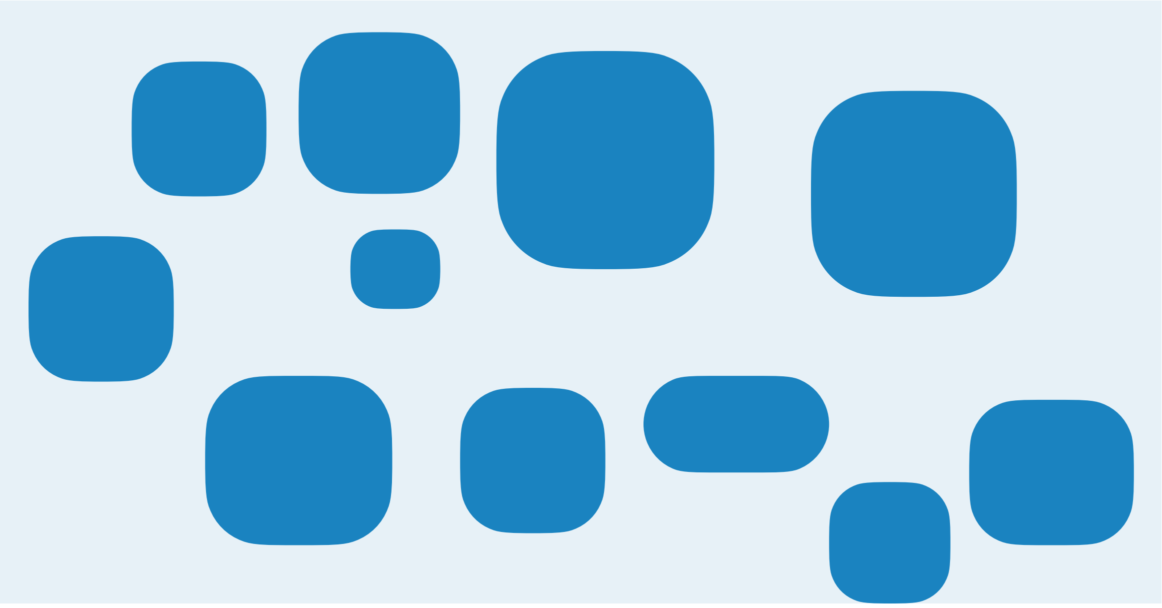

Fig. 5.7 Graphic representation of a model that may explain the non-zero resistivity of the superconducting state. The deep blue structures are superconducting islands, separated by bad metallic background (light blue).

For $LaVO_3/SrTiO_3$ interfaces, indeed, this is not the case. The Hall measurement is a non-local measurement, and for a disordered system like $LaVO_3/SrTiO_3$ interfaces, the voltage probes can measure a potential difference purely due to the difference in the current paths (SAD and SBD) on which the probes are located as shown in Fig. 5.10. For a disordered system resistance of both SAD and SBD can change independently with V_G and the potential difference measured between A and B may not be systematic with V_G. This may be possible if the disorders are sensitive to V_G.

In the case of $LaVO_3/SrTiO_3$ interfaces, we have observed that n does not change prominently with V_G, although the effective resistance of the interfaces is highly sensitive to the gate. This indicates that the disorders are reactive to V_G, and the change in disorders due to V_G is reflected as a change in electronic mobility, μ at the interface. Hence, the change in resistivity with V_G. For an ideal metallic system in the absence of any magnetic field, the potential difference between A and B should be zero or may be brought to zero by using a bridge circuit. Applying a magnetic field perpendicular to the sample plane should result in a pure Hall effect. For $LaVO_3/SrTiO_3$ interfaces, since the resistance of paths SAD and SBD independently vary with V_G, a universal probe/ bridge circuit configuration to zero the potential difference between probes A and B at different V_G in the absence of any magnetic field is not possible. In such cases, the path-dependent contribution must be subtracted from the magnetic field-dependent resistivity data. However, while doing so, one must be careful

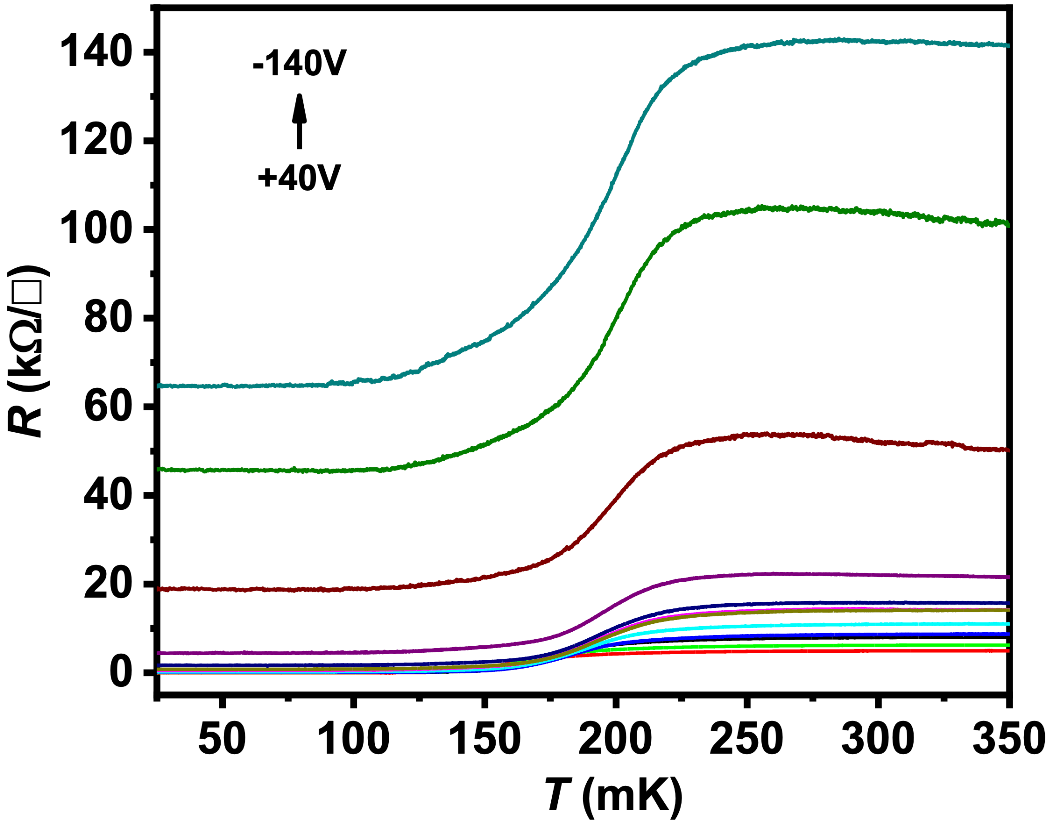

Fig. 5.8 Resistivity R vs temperature T graph at different gate voltages. T_C does not change appreciably with gate voltage.

about the phase of the lock-in amplifier signal to confirm that the subtracted resistivity is only due to path differences. The resistance of the paths *SAD* and *SBD* should systematically change with the magnetic field. For the Hall measurements, we have recorded Hall voltage (potential difference between probes A and B) for both $+ve$ and $-ve$ magnetic fields and then antisymmetrized to obtain Fig. 5.9. For higher V_G towards $-ve$ side since the resistance of the interface becomes higher, measuring voltage becomes difficult for three main reasons,

1. Since we use a ballast resistor of 1 MΩ, for the very high resistance of the sample the current flow through the circuit is also affected.
2. For high resistance, the fluctuation across the voltage probe increases.
3. Lock in amplifier input impedance is also low (10 MΩ). For very high sample resistance, a considerable portion of the current may drain to the ground through voltage probes as well.

For all these reasons, the Hall data for higher sample resistance values are not very smooth.

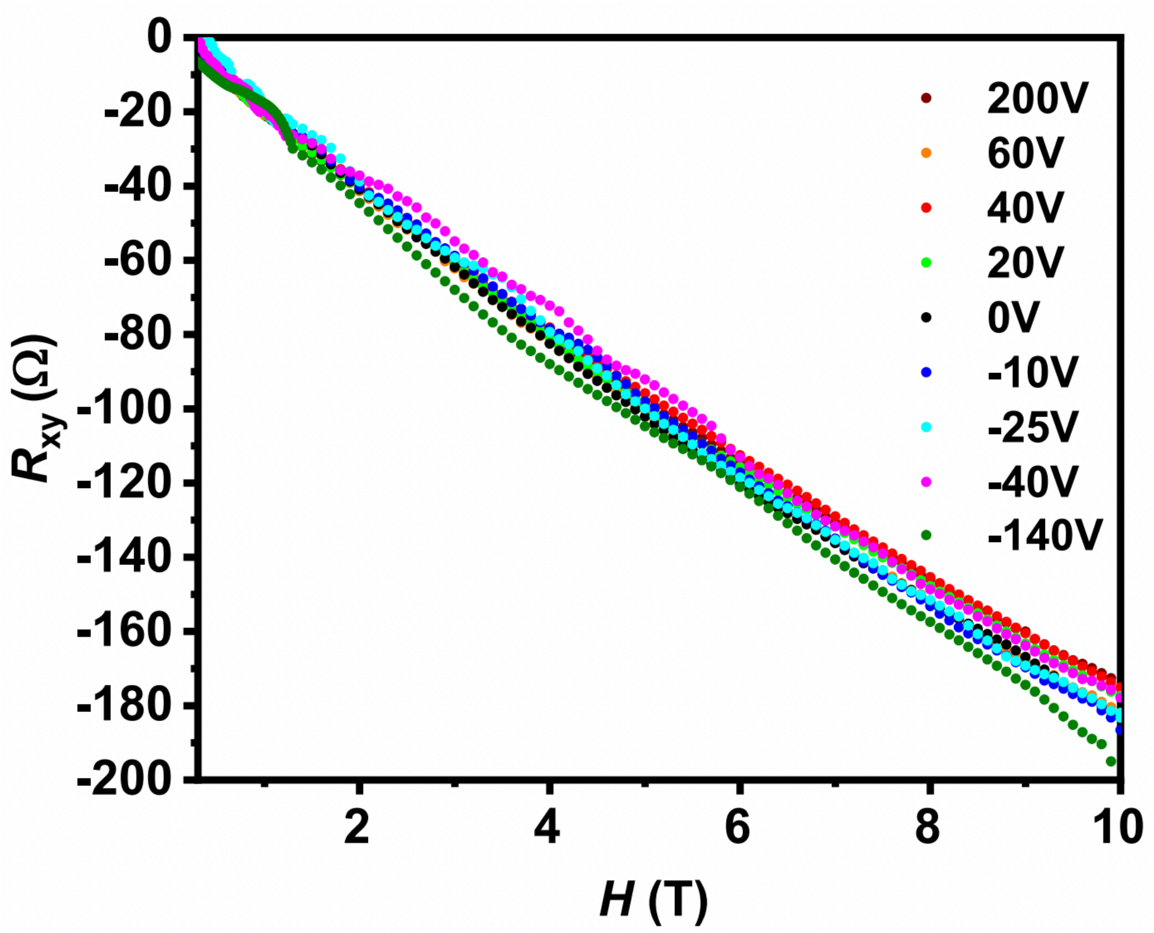

Fig. 5.9 Hall data recorded at different gate voltages at 350 mK. The carrier density is more or less constant at different gate voltages.

The hall data we obtained is non-linear and consistent with a previous report on the $LaVO_3/SrTiO_3$ interface [6]. The hall data at $V_G = 0$ is presented in Fig. 5.11. As seen from Fig. 5.11, the recorded hall data has a maximum deviation from the imaginary linear Hall at about 4.5T. There are different phenomena which may cause a non-linear Hall effect. However, in the case of $LaVO_3$/ $SrTiO_3$ interfaces, the available evidence directs towards two possibilities. In the following, we shall discuss briefly the different origins of non-linearity in the Hall effect and, by the selection by an elimination process, converge to the possibilities in our case,

- Quantum effect becomes prominent in a high magnetic field. In such a case, during field sweep, the system switches from classical to the quantum regime at a very high magnetic field, and non-linearity in the Hall effect is observed. The critical magnetic field for the classical to quantum transition is inversely proportional to the carrier

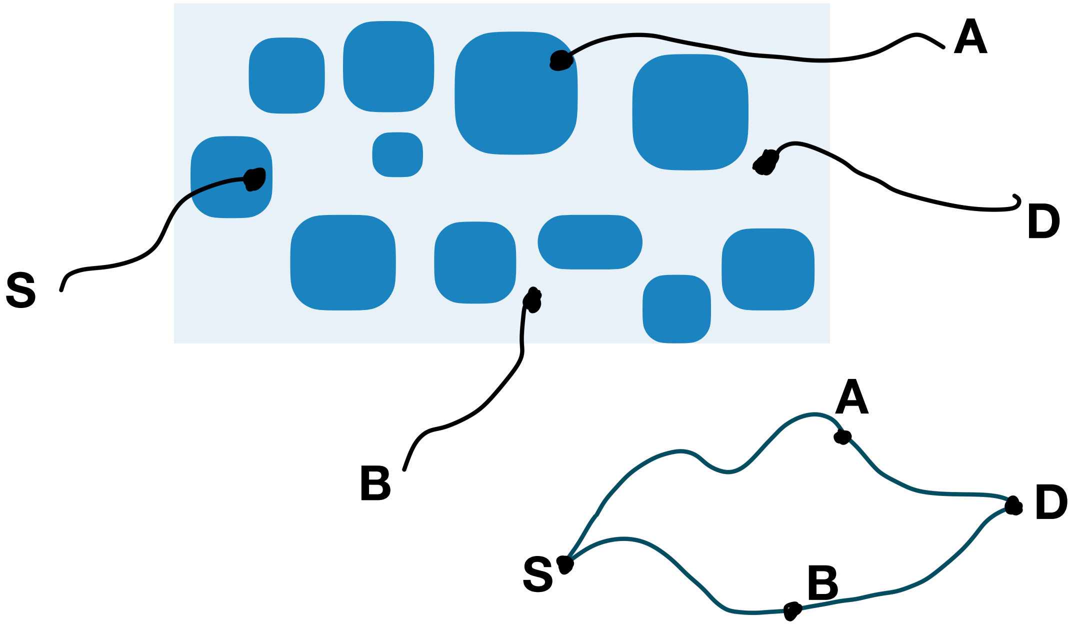

Fig. 5.10 Example of a non-local probe configuration on a disordered system (island system in our case). Probes *S* and *A* are connected to two superconducting islands, whereas probes *B* and *D* are connected to the background. *S* and *D* represent the source and the drain, respectively. *B* and *D* are voltage probes. The current from *S* to *D* can be divided into different paths: *SAD* and *SBD* are two such paths on which probes *A* and *B* are located.

mobility of the sample. In our case, the carrier mobility is 220 cm^{2}V^{-1}S^{-1}, which scales to a value above 45T where the quantum effect may kick in. As we have observed the non-linearity in Hall at about 4.5 T, the quantum effect is not responsible in this case.

- Presence of magnetic order in the sample may also result in a non-linear Hall effect/ anomalous Hall effect. The effective magnetic field encountered by the carriers is affected as the magnetization in a sample with magnetic ordering varies with an applied magnetic field. Consequently, the Hall effect is non-linear so long the magnetization does not saturates. Beyond an applied field where the sample magnetization saturates, Hall voltage goes linear. LaVO$_3$ undergoes an antiferromagnetic transition at 145K, and previously this phenomenon was reported to be responsible for non-linear Hall in LaVO$_3$/ SrTiO$_3$ interfaces. However, the same non-linearity in the Hall is reproducible both at low and room temperatures, which suggests that the non-linearity in our case is not due to the inherent magnetization of the material.

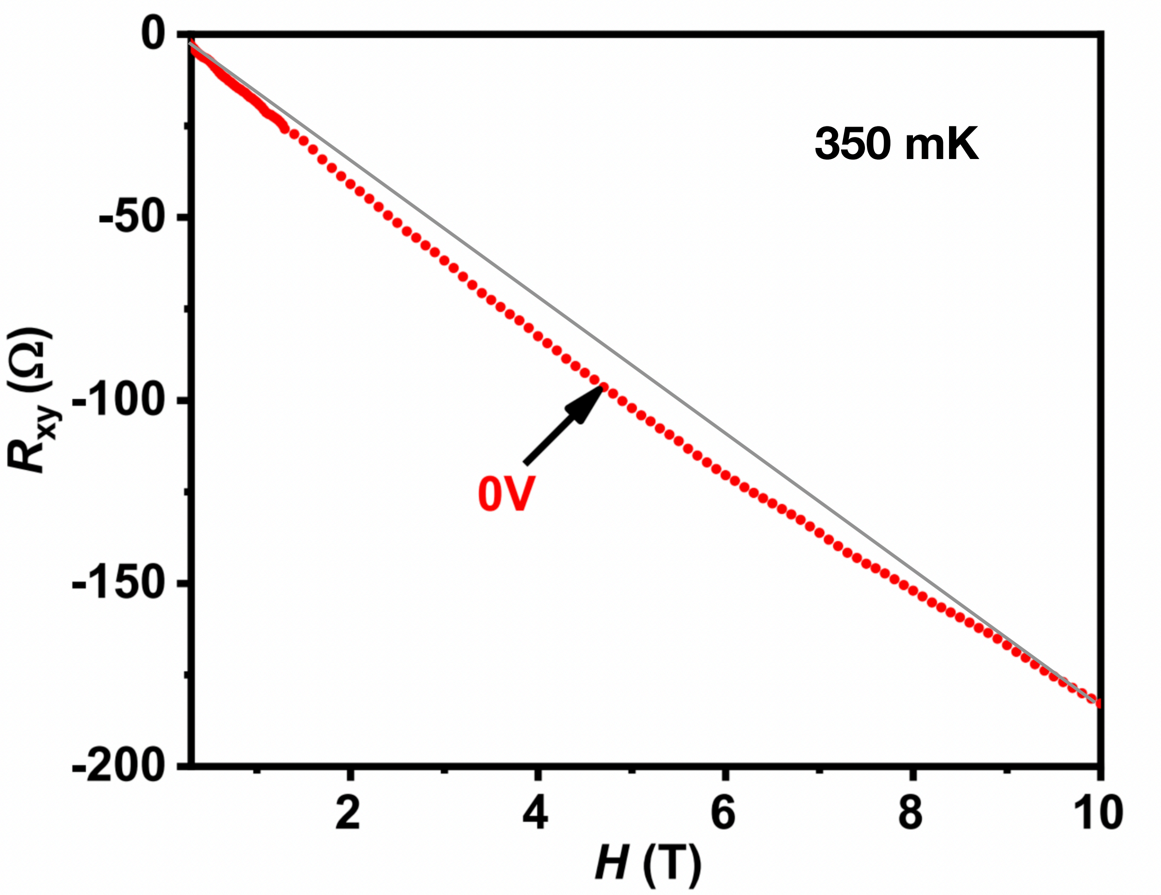

Fig. 5.11 Hall data (red dots) recorded at $V_G = 0$ at 350 mK. The straight grey line is the reference for an imaginary linear hall effect with the same initial and end data points.

- Presence of two conducting channels or two types of carriers may also result in non-linear Hall. In our case, it is difficult to verify whether there are multiple conducting channels. Although the $LaVO_3$ layer is not conducting, the presence of multiple conducting channels cannot be denied based only on this fact. However, our band theory calculation (chapter 3) confirms the presence of two types of carriers at the interface.

Thus based on our observations and theoretical calculation, we can firmly conclude that the non-linear Hall at $LaVO_3$/ $SrTiO_3$ interface is mainly due to the presence of two carriers from two different bands (Ti-*d* and V-*d*). However, the presence of multiple conducting channels cannot be ignored as well. The gate-dependent resistivity is also evident from Fig. 5.12, where voltage vs current data is plotted at different gate voltages. The critical current, I_C, measured at 27 mK, varies with V_G in a similar fashion, i.e. at higher V_G magnitude in the $+ve$ direction I_C increases and vice versa. Both Fig. 5.8 and 5.12 confirm that the superconducting transition is not sharp. Thus, both I_C and T_C have distributions, and one can define them differently. For example, T_C can be defined the same as earlier, The temperature where the resistance drops to 85% of the normal state resistance. I_C can be defined by the peak positions of the derivatives of the graphs in Fig. 5.12. However, for any definition, the basic characteristics remain the same, and a qualitative discussion should suffice to conclude the experimental results. Similarly, there is the distribution of H_{C_2} as well as can be seen in Fig. 5.13, where resistivity as a function of the magnetic field is plotted at different gate voltages at 27 mK. Fig. 5.13 also suggests that H_{C_2} is not very sensitive to the gate, which concludes that the superconducting coherence length, ξ, does not change with the gate voltage. In our island picture, the distribution of T_C, I_C, and H_{C_2} can be attributed to the fact that they may vary from island to island.

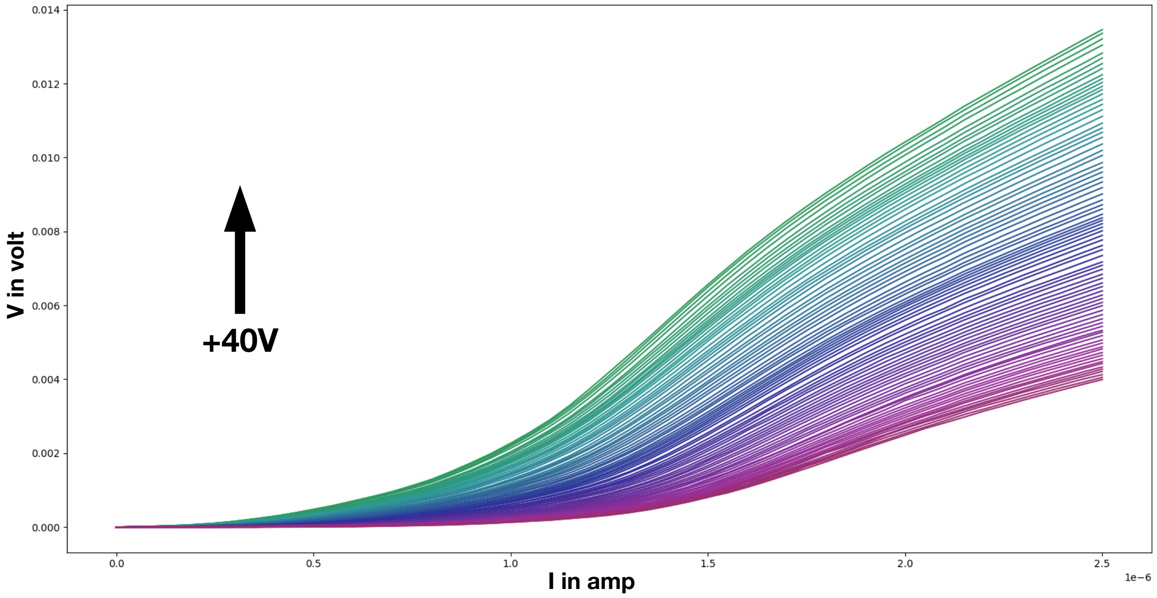

Fig. 5.12 Voltage V vs current I graph, recorded at 27 mK at different gate voltages.

To understand the phenomenon that allows change in interface electrical resistance for both superconducting and normal states while maintaining other parameters like T_C and H_{C_2} constant, we need to revisit the superconducting island model. In chapter 3, we have already discussed that it is highly likely that the $LaVO_3/SrTiO_3$ interface is ferroelectric. The ferroelectric domains act as local gates at the interface that modulate the local carrier density, creating a nonuniform carrier distribution associated with the ferroelectric domains throughout the interface. The local carrier density depends upon the polarization of the ferroelectric domain. Thus, the whole conducting interface is fragmented into domains of different carrier densities.

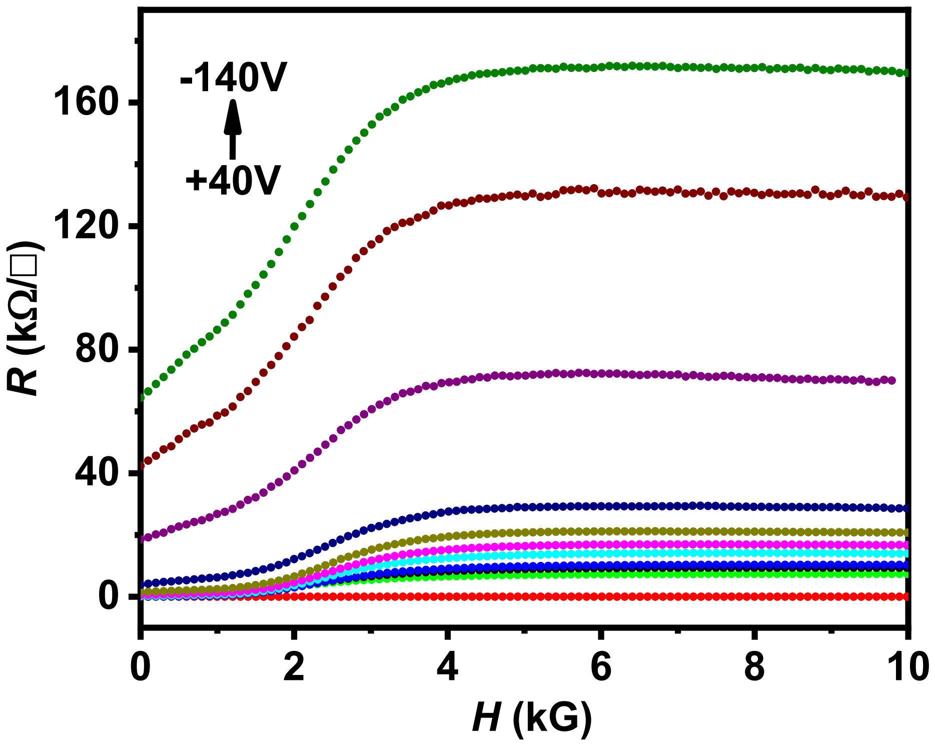

Fig. 5.13 Resistivity R vs temperature T graph, recorded at 27 mK at different gate voltages. H_{C_2} does not change with gate voltage.

For a small range of polarization values of ferroelectric domains, the associated conducting domains display superconductivity. We shall call this range of polarization P_{SC} and the remaining range P_N. With V_G, the ratio of effective ferroelectric domain areas with P_{SC} and P_N changes. Consequently, the size of the associated conducting domains changes as well. We call the conducting domains that can undergo superconducting transitions, superconducting islands and the rest of the conducting domains are called background. In a simplistic picture, the size of the superconducting islands changes in a way, as shown in Fig. 5.14. The size of the islands grows or shrinks with increasing V_G in $+ve$ and $-ve$ direction respectively, since, the size of the ferroelectric domains associated with them or responsible for their existence changes with V_G. As the islands grow (shrink) in size, the inter-island distance decreases (increases) and the effective resistance between two islands go down (up). We have observed this in both gate-dependent R vs T data and gate dependent V vs I data.

The change in resistance with V_G in our island picture can be modeled theoretically using the network resistor model (not within the scope of this discussion). This process, to a certain degree, only changes the superconducting island size, not the carrier density or superconducting characteristics, since the size of the ferroelectric domains varies with V_G whereas domain-wise P_{SC} and P_N are expected to remain constant. Thus, in our case, we have observed that T_C and H_{C_2} do not change appreciably. We have mentioned earlier that the background is a bad conductor; we also observed that the normal state tends to show an insulating behaviour at higher V_G on the $-ve$ side. In Fig. 5.15 R vs T graphs at $V_G =$ -100V and -120V are shown. In both cases, when the superconductivity is suppressed by the application of 1 T magnetic field, the interface displays insulating behaviour. At higher temperatures (above 300mK), the graphs recorded in the absence and presence of a magnetic field tend to overlap. The little mismatch of these graphs is due to the misalignment of the voltage probes, which in a magnetic field could read some excess (less) voltage drop due to the Hall effect. Magnetoresistance of the interface may also contribute to this. For both graphs recorded in 1T magnetic field, an onset of insulating to metallic transition can also be observed at a temperature below 60 mK (grey arrows).

Also, from Fig. 5.8, it can be observed the normal state undergoes a transition from metallic to an insulating state as V_G increases on the $-ve$ side. This effect could be attributed to the fact that the ratio between the areas covered by superconducting islands and the background varies with gate voltage. It can be expected that at a low value of the ratio (V_G is $-ve$ and high), the interface behaves as an insulator in the normal state. In contrast, for a higher value, the interface becomes a conductor. Although we assumed that P_{SC} and P_N should remain constant during a gate sweep, in reality, they could experience a subtle change favourable to the direction and intensity of the V_G. Thus, the exchange of carriers between the superconducting islands and the background during a gate sweep and, consequently, changes in relative carrier density is possible. In our case, this effect was weak and barely noticeable. By taking derivative of the curves in Fig. 5.8 with respect to temperature and considering the peak position of the respective curves along temperature axis as T_C (Fig. 5.16 **b**) we can extract T_C vs V_G graph (Fig. 5.16 **c**). The derivatives are noisy, as shown in Fig. 5.16 **a**, and determination of the peak position from the graph is impossible. However, an average of 100 points after the derivative is quite systematic, and the peak position is very clear. We have also verified the peak positions by 7th order polynomial fitting of the R vs T curves near the inflection points and taking derivative with respect to T of the fitted curves (not shown here). In both methods, the peak positions were the same. Our T_C vs V_G graph (Fig. 5.16 **c**) has a peak near -120V and the graph has almost dome-like shape.

Similar feature was observed in case of LaAlO$_3$/SrTiO$_3$ interfaces [21]. The dome shape of the T_C vs V_G graph for LaAlO$_3$/SrTiO$_3$ interface was more prominent, and the T_C had a change of 250 mK in a similar range of gate voltage sweep as ours. In case of

$LaAlO_3/SrTiO_3$ interfaces the T_C had a sharp fall as V_G increased in the $-ve$ side. This was called the underdoped regime. For an increase in V_G in the $+ve$ side, the T_C had a slight increase initially, and then there was a gradual drop. This regime where T_C had a gradual drop was called the overdoped regime. In the case of $LaVO_3/SrTiO_3$ interfaces, we have observed the opposite phenomenon. As can be seen from Fig. 5.16 **c**, in our case, the presence of underdoped and overdoped regime seems to be on the $+ve$ and the $-ve$ side of V_G. This contradiction certainly poses a serious question. However, this could be explained by our island model. As discussed earlier, the size of the superconducting islands grows bigger with increasing V_G in the $+ve$ side. This also means that the component of P_N along P_{SC} may grow bigger, which as a result, favours higher carrier density in the background. The higher background carrier density should be achieved by acquiring extra carriers from the ground or the superconducting island. In our case, the carrier transfer from the superconducting islands while lowering the carrier density of the islands themselves is more favourable. Consequently, the superconducting islands reach the underdoped regime.

Similarly, when V_G increases in the $-ve$ direction, the islands shrink in size. At the same time, the carrier density of the islands grows since the component of P_N along P_{SC} decreases, and the background is more favourable to lower carrier density. Consequently, the superconducting islands reach the overdoped regime. This should also be noted that in our case, the change in T_C is much smaller ($\sim$ 40mK), and thus the exchange of carriers between the superconducting islands and the background is minimal.

5.5 Conclusion

We have investigated a relatively unexplored perovskite oxide heterostructure conducting interface, $LaVO_3/SrTiO_3$ [001] and discovered that the interface is superconducting below 250 mK. The superconductivity is unconventional in nature, and the order parameter has a non s-wave signature. The $LaVO_3/SrTiO_3$ [001] interface is disorder, and the superconducting state has non-zero resistance below the transition. Our investigation revealed that the ferroelectricity at the interface results in fractured superconducting domains (we call them islands) with a bad metallic background. The ferroelectricity allows the superconducting domains to be controlled by gating. In a sense, the superconducting state can be modulated by tuning the in situ disorder by an external electric field. Thus, the $LaVO_3/SrTiO_3$ [001] interface is complex and a potential system to study disordered low dimensional superconductors where exotic phases (like Bose Metal) may be achieved by controling the disorder.

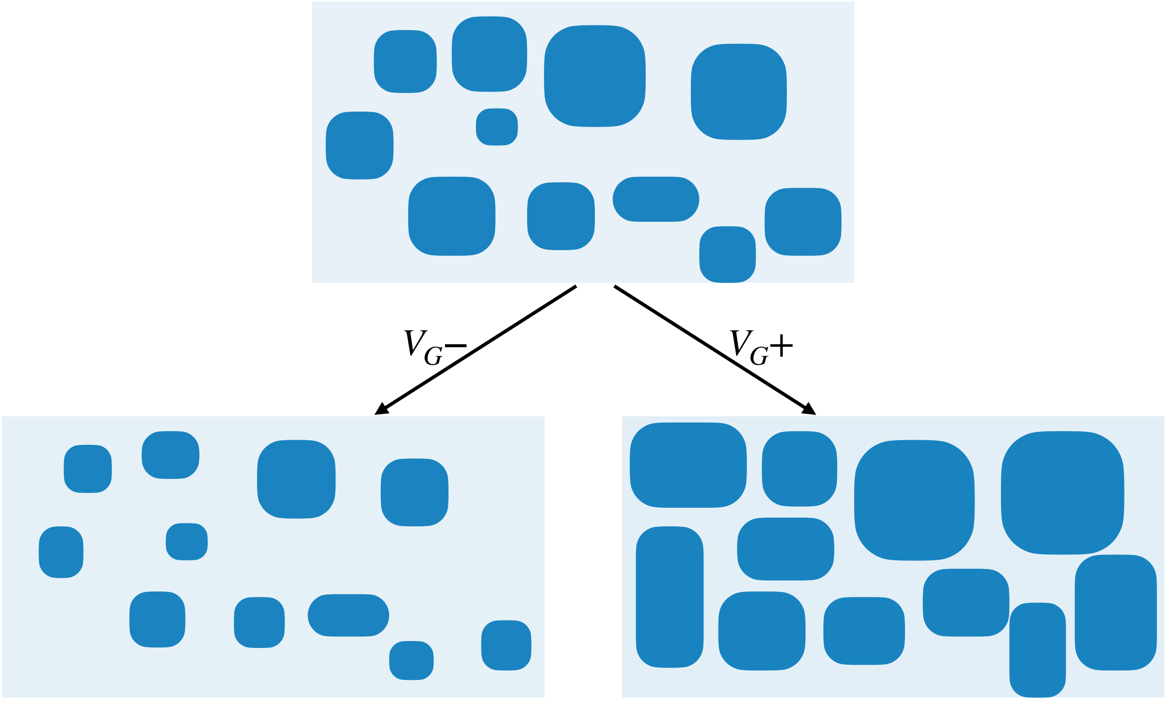

Fig. 5.14 The size of the superconducting island changes with varying gate voltage, V_G. For higher V_G value on the negative side (V_G-), the superconducting islands' size decreases, whereas, on the positive side (V_G+), the superconducting islands grow in size.

5.6 Contribution

- **Fig. 5.1 and LaVO$_3$/ SrTiO$_3$ heterostructure samples:** Anamika Kumari and Suvankar Chakraverty, Quantum Materials and Devices Unit, Institute of Nano Science and Technology, Sector-81, Punjab, 140306, India.
- Some parts of the ultra low temperature experiments were carried out jointly with Mona Garg and Nikhlesh Singh Mehta.

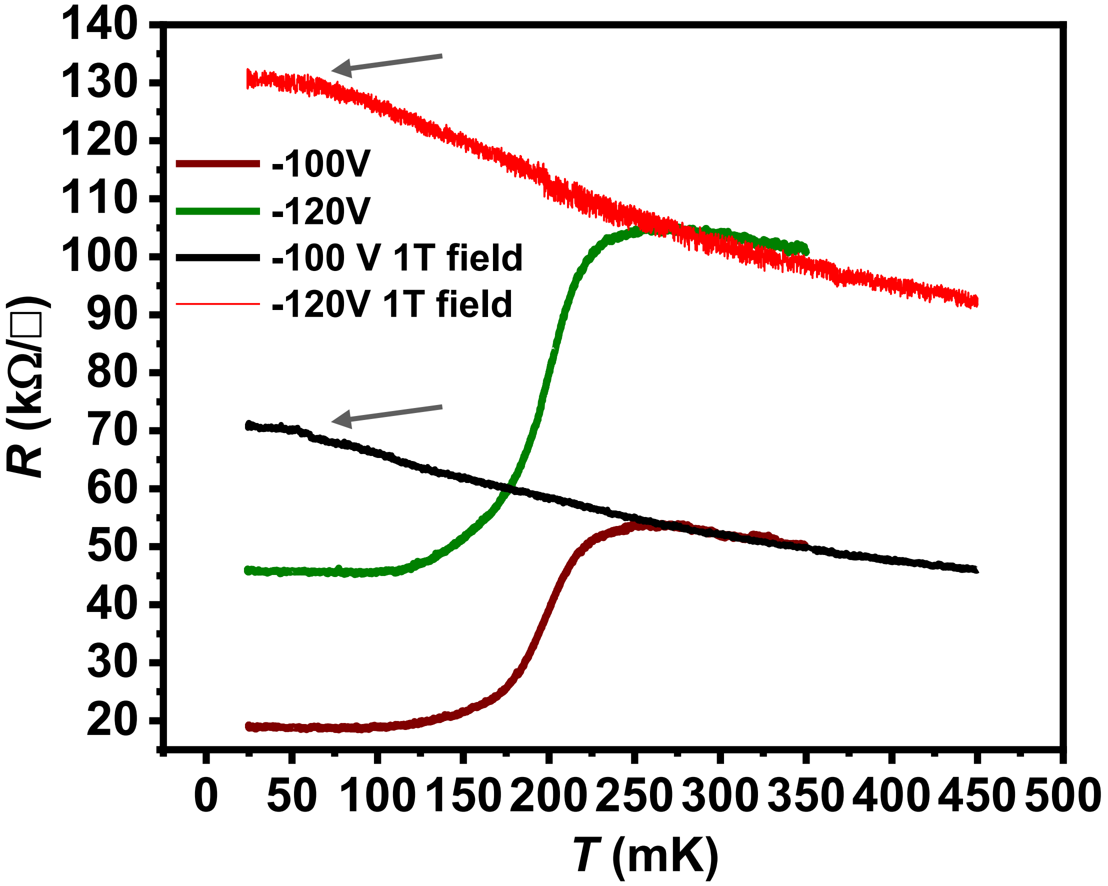

Fig. 5.15 Resistivity vs temperature data recorded at -100V gate voltage in the absence (brown) and presence (black) of the magnetic field. Similar data was recorded at -120V gate voltage in the absence (green) and presence (red) of the magnetic field. The gray arrows point to the region where metal-to-insulator transitions occur in the black and red graphs.

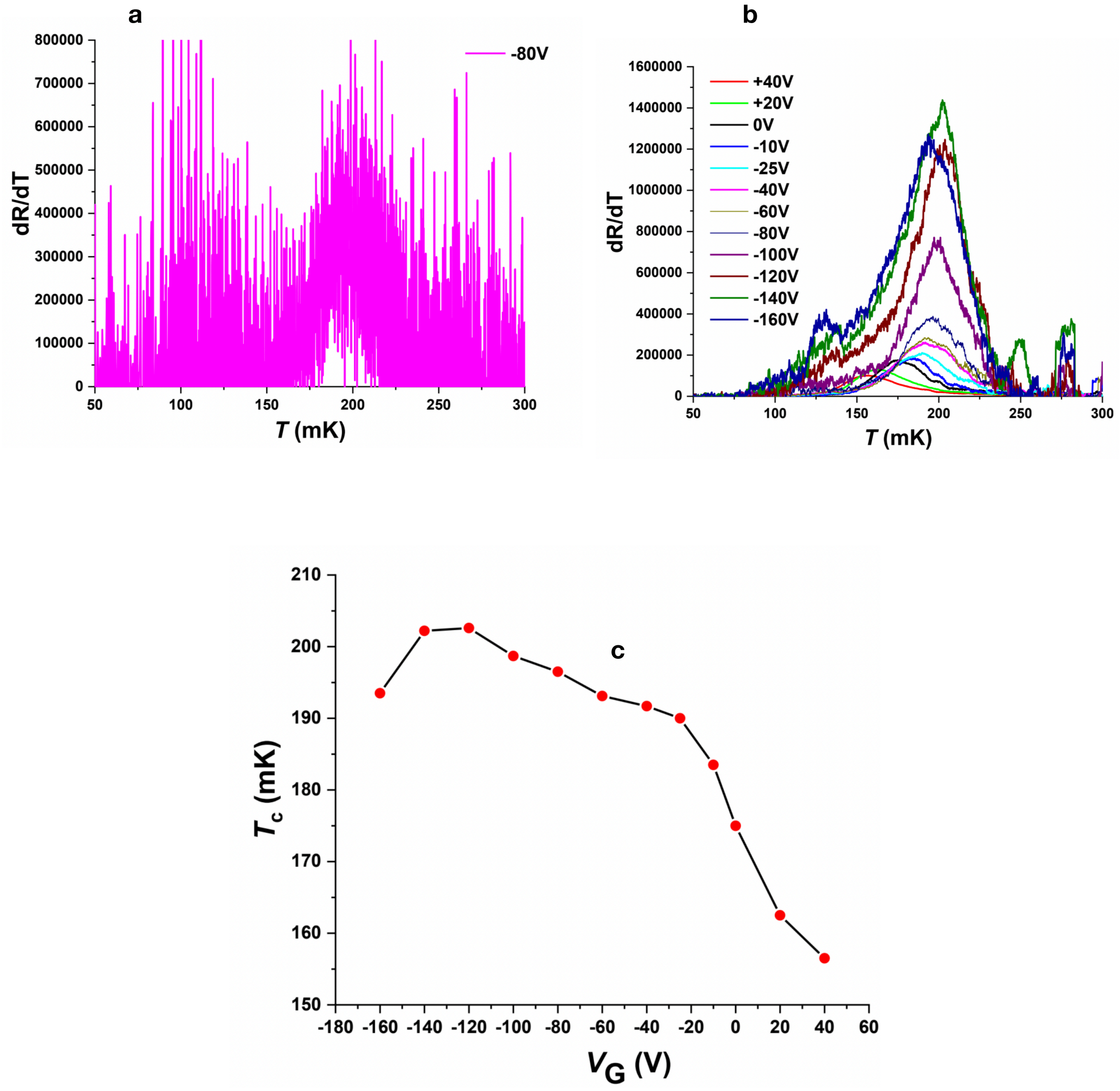

Fig. 5.16 **a** Derivative of the resistivity vs temperature graph with respect to the temperature recorded at -80V gate voltage. The graph is noisy. **b** Similar graphs after 100 points averaging. **c** Considering T_C to be the peak positions of the respective graphs in **a** T_C vs gate voltage is plotted.

Chapter 6

Scanning tunneling spectroscopy (STS) and quasi-particle interference (QPI)

6.1 Introduction

We have briefly discussed in chapter 2 how probing the density of states helps us determine superconducting energy gaps. Acquiring density of states data for any material allows us to learn about the material at a quantum level. Scanning tunneling spectroscopy (STS) is one of the key tools to measure the relative density of states on the surface of a material. STS is a highly sensitive measurement technique, requiring a complicated electronic and noise-isolated set-up. Such measurements can provide complex information about the material surface. Quasi-particle interference (QPI) pattern on the surface is one such information that can be probed by the STS method to extract momentum space data for the material. To understand how the QPI data is acquired, we should first discuss STS in detail.

6.2 Scanning Tunneling Spectroscopy (STS)

Scanning Tunneling Spectroscopy is an energy-resolved measurement which relies on a quantum phenomenon, tunneling. The method requires a very sharp conducting tip, ideally one atom at the end of the tip and a conducting sample. The tip-to-sample distance is such that in the application of a bias voltage between the tip and the sample, electrons can tunnel from the tip to the sample or vice versa, depending upon the direction of the applied voltage. It is evident that for the tunneling mechanism to work, the electron wavefunction must have some spread from the sample to the tip without them being in physical contact. The usual distance between the tip and the sample is of the order of Å. This tunneling phenomenon allows a current, also known as the tunneling current, through the circuit that depends upon the applied bias voltage. By measuring the current, information on the conducting surface at the quantum level can be obtained. The tunneling current is not any kind of breakdown current. If an ac bias voltage is applied, the tunneling current will also be an ac with the same phase as the bias voltage, unlike for capacitive connections where the phase changes by $\frac{\pi}{2}$.

In a very general sense, for a material, the density of states, $\rho(E)$ is related to the charge density, n, by the following equation,

$$n = \int_E \rho(E) f(E) dE \tag{6.1}$$

where $f(E)$ is the Fermi distribution function, and the integral is taken over all the energy range. Now, STS can probe $\rho(E)$ and if $\rho(E)$ can be mapped on a surface for different energies, followed by summing all those maps, one should be able to acquire the charge density mapping of the surface. Fortunately, this summation process is a well-known technique called scanning tunneling microscopy (STM). Binning and Rohrer invented STM in 1982, which won them the Nobel prize in physics in 1986 [48]. STS is basically an STM technique with some modifications that allow real-time probing of $\rho(E)$. STM technique is so powerful and sensitive that for an atomically flat metallic surface, the atoms can be imaged. It is always true that measuring a cumulative effect (n, in this case) is easier than measuring the causal components of that effect ($\rho(E)$ at different E's, in this case). Thus, STS is more sensitive than STM.

In Fig. 6.1 **a** schematic of a STM circuit is presented. A bias voltage V is applied between the tip and the sample. The tunneling current runs through a current-to-voltage amplifier, the output from which gives the measurement of the current. The tip is attached to an end of a piezo tube. In this case, the outside of the tube is divided into quadrants by X (X+, X-), Y (Y+, Y-) and Z electrodes. The tip can be driven in different directions by applying proper voltages in the different electrodes. The voltages are applied with respect to the ground. The inner surface of the piezo tube is grounded. In some piezo tubes, Z movement is controlled by X and Y electrodes.

Theoretically, the tunneling current could be calculated from the time-dependent perturbation theory [49] where the tunneling probability rate of an electron from a state μ in the sample to a state ν in the tip, $P_{\mu\nu}$ is given by Fermi's golden rule,

$$P_{\mu\nu}(t) = \frac{2\pi}{\hbar} \delta(E_\mu^S - E_\nu^T) |M_{\mu\nu}|^2 \tag{6.2}$$

Here, $M_{\mu\nu}$ is the tunneling matrix elements for tunnelling between a state μ in the sample with energy E_μ^S and a state ν in the tip with energy E_μ^T (superscripts S and T represent sample

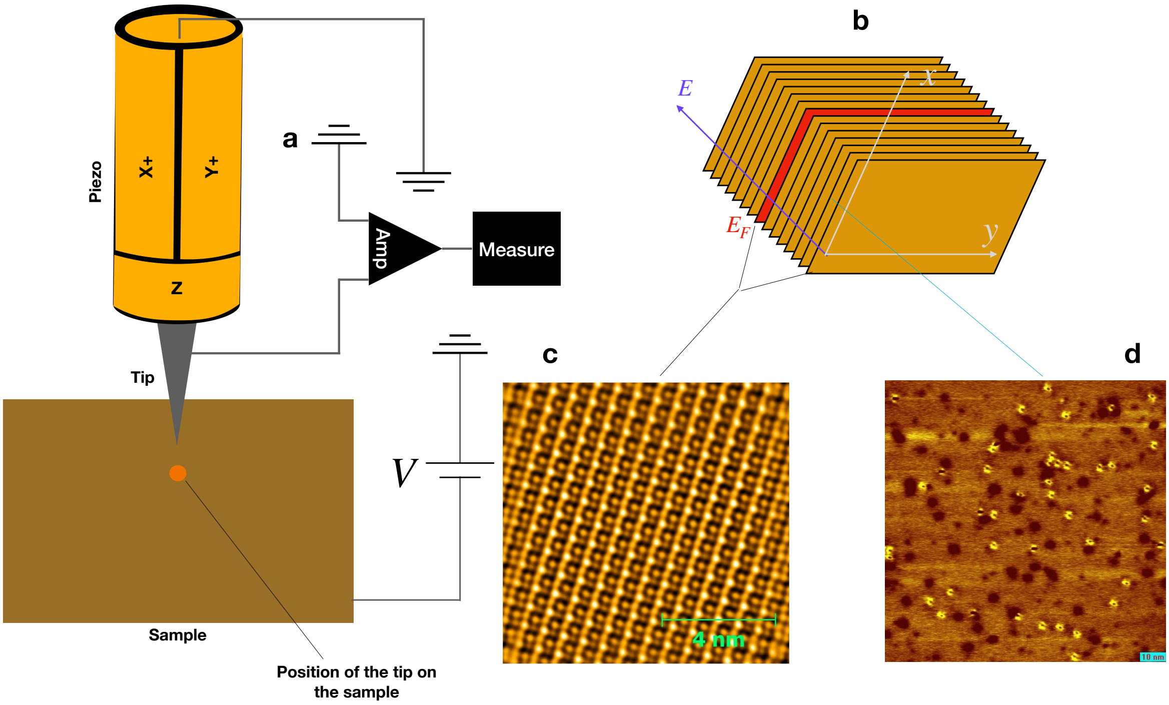

Fig. 6.1 **a** STM circuit diagram. The yellow patches on the piezo, marked as X+, Y+ and Z, are electrodes to drive the tip along X, Y and Z directions. X- and Y- electrodes are located at the opposite sides of the X+ and Y+ electrodes (not shown here). V is the applied voltage between the tip and the sample. The orange dot on the sample represents the position on the sample where the tip is scanning. The tip is exactly above the orange dot and not touching the sample. The tunneling current runs through an amplifier marked as 'Amp' here. The output from the amplifier is measured.**b** STS mapping/ $\rho(E)$ mapping at different energy values. Respective axes are shown. Each rectangle on the stack represents ρ as a function of X and Y at different energy values. There should be an infinite number of such rectangles to cover the whole energy spectrum. However, for any material, a certain energy range is only relevant. The red rectangle represents the ρ map at the Fermi energy E_F. **C** the atomic resolution image of the surface of a sample ($PtSn_4$), acquired by STM. Ideally, the image should represent the summation of all rectangles in the stack, but for a metal above E_F, ρ should be zero. Thus, it is sufficient to consider energy up to E_F. **d** ρ mapping of the $PtSn_4$ surface, a rectangle out of the stack.

and tip respectively). The expression (6.2) is valid for both tip-to-sample and sample-to-tip tunneling of electrons. Thus, the tunneling current $I \propto eP_{\mu\nu}$. The delta function in the expression of $P_{\mu\nu}$ also suggests that the expression is valid for elastic tunneling only, i.e., the energy remains constant in the process. Inelastic tunneling is also possible when excitations of phonons, photons, spin etc., are involved. For our purpose, the discussion is limited to elastic tunneling only. Although $P_{\mu\nu}$ represents the tunneling probability from a state μ to ν, the tunneling requires μ to be filled and ν to be empty. And the tunneling current should have a contribution from all such states. We know that for electrons, the probability of a state at energy E to be occupied is given by $f(E)$ and the probability for the same state being unoccupied is given by $1 - f(E)$ where $f(E)$ is the Fermi distribution function. A bias voltage, V, between the sample and the tip shifts the energy levels of the sample with respect to the tip by eV. In thermal equilibrium, the effective tunneling current from sample to tip, $I_{S\to T}$, in the presence of bias voltage is

$$I_{S\to T} = \frac{4\pi e}{\hbar}\sum_{\mu\nu} f(E^S_\mu)[1 - f(E^T_\nu)]|M_{\mu\nu}|^2\delta(E^T_\nu - E^S_\mu - eV). \tag{6.3}$$

Similarly, the current from tip to sample, $I_{T\to S}$ is

$$I_{T\to S} = \frac{4\pi e}{\hbar}\sum_{\mu\nu} f(E^T_\nu)[1 - f(E^S_\mu)]|M_{\mu\nu}|^2\delta(E^T_\nu - E^S_\mu - eV). \tag{6.4}$$

The Fermi energy E_F for both sample and tip are taken to be zero. The factor of 2 in equations (6.3) and (6.4) to incorporate the spin quantum number is included. The effective tunneling current, I, is the difference of $I_{S\to T}$ and $I_{T\to S}$.

$$I = \frac{4\pi e}{\hbar}\sum_{\mu\nu}[f(E^S_\mu) - f(E^T_\nu)]|M_{\mu\nu}|^2\delta(E^T_\nu - E^S_\mu - eV) \tag{6.5}$$

In continuous limit the summation for both the indices, μ and ν, can be replaced by $\int \rho(E)dE$, where $\rho(E)$ represents the density of states at energy, E. The equation (6.5) is then transformed in the following form,

$$I = \frac{4\pi e}{\hbar}\int [f(\varepsilon - eV) - f(\varepsilon)]|M|^2\rho^T(\varepsilon - eV)\rho^S(\varepsilon)d\varepsilon. \tag{6.6}$$

Since the energy levels of the sample with respect to the tip are shifted by eV, it is sufficient to limit the integration to eV. At low temperatures where k_BT is smaller than the energy resolution required for the experiment, the Fermi function is sharp or considered a step function. Thus, for low temperature, the expression of I is,

$$I = \frac{4\pi e}{\hbar}\int_0^{eV} |M|^2\rho^T(\varepsilon - eV)\rho^S(\varepsilon)d\varepsilon. \tag{6.7}$$

Tungsten tips are used for our measurements. For tungsten, the density of states is considered to be flat near the Fermi surface, and I in that case is,

$$I = \frac{4\pi e}{\hbar}\rho^T(0)\int_0^{eV} |M|^2\rho^S(\varepsilon)d\varepsilon. \tag{6.8}$$

Equation (6.8) immediately suggests that $\frac{dI}{dV} \propto \rho^S(eV)$. $\frac{dI}{dV}$ can be directly measured by a lock-in amplifier, and the method is similar to what we discussed in section 4.6, except that in this case, the current is measured instead of the voltage. It is also evident that equation (6.8) must be satisfied for this method to work. Equation (6.8) is only valid for low temperatures. Thus, the $\rho(E)$ mapping is efficient only at the low-temperature range. We have performed our experiments in a He3 refrigerator which allows the sample space to go as cold as about 330 mK.

To understand the mechanism of $\rho(E)$ mapping, we need to understand the working principle of STM. In our case, we use constant current mode for STM. A constant voltage is applied between the sample and the tip, and a current value is set. A scanning area is selected and divided into pixels. By driving the piezo along the XY plane, the tip is moved from pixel to pixel in a raster pattern. The size of the pixel is limited by the resolution of the XY movement of the piezo. At every pixel, to maintain the constant current, depending upon the local electronic and topographic configuration, the tip is engaged towards or retracted from the sample by controling the Z electrode. The voltage values at the Z electrode to maintain the constant current is recorded for each pixel which gives the topographic image. At each pixel, once the tip is stabilized for the set current and applied voltage, the lock-in current value is recorded, which basically is $\rho(E)$. Essentially, we obtain a spatial map of $\rho(E)$. The typical timescale of the measurement is of the order of 1 mS/ pixel. Atomically flat sample surfaces are well-suitable for STM/ STS experiments. To obtain an atomically flat surface, layered samples are cleaved in an ultra-high vacuum at 77K. Some materials cannot be cleaved. For those samples, the surface is first polished, then argon ions are bombarded onto the surface at high energy to attain a clean and smooth surface finish.

6.3 Quasi particle interference (QPI)

In the last sections, we have discussed how STS can map the density of states. For a perfectly clean crystal (without any defect), the electronic wave function ψ_{nk} is Bloch's wave function, and the expression is:

$$\psi_{nk}(r) = e^{ik\cdot r} u_{nk}(r) \tag{6.9}$$

where n and k represent band index and crystal momentum, respectively. r is the position coordinate, and $u_{nk}(r)$ is a function with the periodicity of the lattice. The local density of states $\rho(E,r)$ at energy E and position r, in this case, is calculated to be:

$$\rho(E,r) = \psi^*_{nk}(r)\psi_{nk}(r) = \sum_k u_k(r)u^*_k(r)\delta(E-\varepsilon(k)) \tag{6.10}$$

Certainly, the k information is lost in the summation here. However, in the presence of defects, the Bloch states elastically scatter from the defect sites, consequently mixing the states. A mixed state $\psi_E(r)$ is:

$$\psi_E(r) = \sum_k e^{ik\cdot r} u_k(r). \tag{6.11}$$

The inter-band scattering is possible as long as the energy is conserved. Thus, in the expression, there is no band index. The density of states in this case is:

$$\rho(E,r) = \psi_E^*(r)\psi_E(r) = \sum_{kk'} u_k(r) u_{k'}^*(r) e^{i(k-k')\cdot r}. \tag{6.12}$$

It is evident that $\rho(E,r)$ is a mixture of periodic functions with periodicity $\frac{2\pi}{q}$ for allowed q, where $q = k - k'$. STS can capture this periodicity. Ideally, for a particular energy, $\rho(E,r)$ map can be obtained using the STS technique, then the components of different q values can be extracted by fast Fourier transforming the map. A fast Fourier transformation (FFT) is an auto-correlation process where two copies of the acquired maps are compared with each other by giving one a relative shift with respect to the other to extract different q values. It is also natural to consider that the intensities of the periodic functions for different q values are not the same. Thus, for simplification, only those q values are considered where scattering from state $|k\rangle$ to $|k'\rangle$ has the highest probability [50]. This constrains $|k\rangle$ and $|k'\rangle$ to those values where the joint density of states have maximums. For a mapping of a finite area, the discontinuity at the map boundaries behaves like a delta function for FFT, which invokes unnecessary frequency amplitude in the spectrum. This effect is suppressed using a window function while performing the FFT. In the next chapter, the experimental work where the QPI measurements were done on $PtSN_4$ will be discussed.

6.4 Conclusion

The STS technique is very effective in measuring the relative density of states of a sample surface. Angle-resolved photoemission spectroscopy (ARPES) is another technique that can measure the density of states. However, the strength of STS lies in its ability to map the spatial density of states, unlike ARPES, where the spatial average of the density of states is acquired. STS mapping is very useful for extracting QPI data. The analysis of QPI data can provide information about the surface band structure.

Chapter 7

$PtSn_4$, STS data and discussion

7.1 Introduction

PtSn4 is a topologically non-trivial material, a topological semimetal, accommodating a Dirac node arc in the band that emerges from the surface states. In topological semimetals, the valence and conduction bands cross each other, leading to non-accidental, symmetry-driven degeneracy in the Brillouin zone. Such degeneracy cannot be lifted by tuning the Hamiltonian without breaking the same symmetry that causes/protects the band-crossing without hybridization [51–53]. In three-dimensional topological semimetals, the band-crossing may happen at discrete k points. The Weyl and the Dirac semimetals are examples of that [54]. Within the low-energy approximation, the dispersion near the band crossing is seen to be linear (Dirac-like). The band-crossing may also happen at multiple, consecutive k points along a closed curve, a nodal line. In such cases, there are three possibilities: (a) The nodal line may run across the Brillouin zone. In this case, the ends of the line meet at the zone boundaries. (b) The line forms a closed loop within the Brillouin zone. (c) Multiple connected loops may form a chain-like structure in the Brillouin zone. The systems showing either of the aforementioned features are collectively known as the topological nodal line semimetals [55–58]. While the existence of the Dirac and Weyl fermions have been demonstrated in a number of material systems like Cd_3As_2 [59–61], TaAs [62–64], Na_3Bi [65; 66] etc., a clear demonstration of a topological nodal line semimetal remains an unachieved goal. Based on angle-resolved photo-emission (ARPES) experiments, $PbTaSe_2$[67] and ZrSiS [68] were earlier found to be the most promising candidate nodal line semimetals. More recently, ARPES experiments suggested a strong possibility of the existence of nodal arc states in $PtSn_4$, a compound that displays unusually large magnetoresistance and hosts an extremely complicated band structure [69].

7.2 Data and discussion

In [69], PtSn$_4$ was chosen as a candidate system for topological semimetallicity solely based on the observation of extremely large magnetoresistance ($\sim 5 \times 10^5\%$) in the material [70–72]. The ARPES experiments indicated the existence of multiple gapless Dirac-like features extending along a line consisting of multiple k points, giving rise to a nodal arc with Dirac dispersion at each gapless k point. The indication of such a feature is special because this hints at the possibility of the first observation of an “open-loop" Dirac nodal line. All the previously proposed nodal line material systems were thought to host closed-loop nodal lines. Motivated by these exciting possibilities, we employed STS on high-quality single crystals of PtSn$_4$.

The quality of the single crystals (the structure is shown in the *inset* of Fig. 7.1 **a**) used in this study is reflected in Fig. 7.1 **a** where a large residual resistivity ratio (RRR) of ~ 396 is seen. In Fig. 7.1 **b** we show a typical atomic resolution image of the ultra-high vacuum (UHV)-cleaved surface of PtSn$_4$. Fig 7.1 **c** depicts a larger area image where defect states in PtSn$_4$ are seen. We found two types of defects, appearing as bright/dark spots in the STM images. Such randomly distributed defect states with an atomically flat background is an ideal environment for QPI spectroscopy. In order to perform QPI spectroscopy, we have carried out the density of states mapping at various energies. A representative map (corresponding to the topography in Fig. 7.1 **c**) captured at V = 100 mV is shown in Fig. 7.1 **d**. Clear interference patterns around the defects can be seen. Such density of states map is then fast Fourier transformed (FFT) to extract momentum space information. From this point on, unless specified otherwise, wherever we mention QPI pattern, we refer to FFT pattern of the density of states mapping.

In order to investigate the evolution of the momentum space features with energy, we have captured energy-dependent QPI spectroscopic maps for both the conduction and the valence bands. The experimentally obtained QPI features were analyzed by developing a theoretical model for QPI in PtSn$_4$ by our theoretical collaborators. The model involves calculating the joint density of states (JDOS) at a given wave vector q and energy ω

$$JDOS(q,\omega) \quad = \quad \int A(k+q,\omega)A(k,\omega)dk \tag{7.1}$$

with the spectral function $A(k,\omega)$ given by,

$$A(k,\omega) = \frac{1}{\pi} Im \sum_a G_{aa}(k,w) \tag{7.2}$$

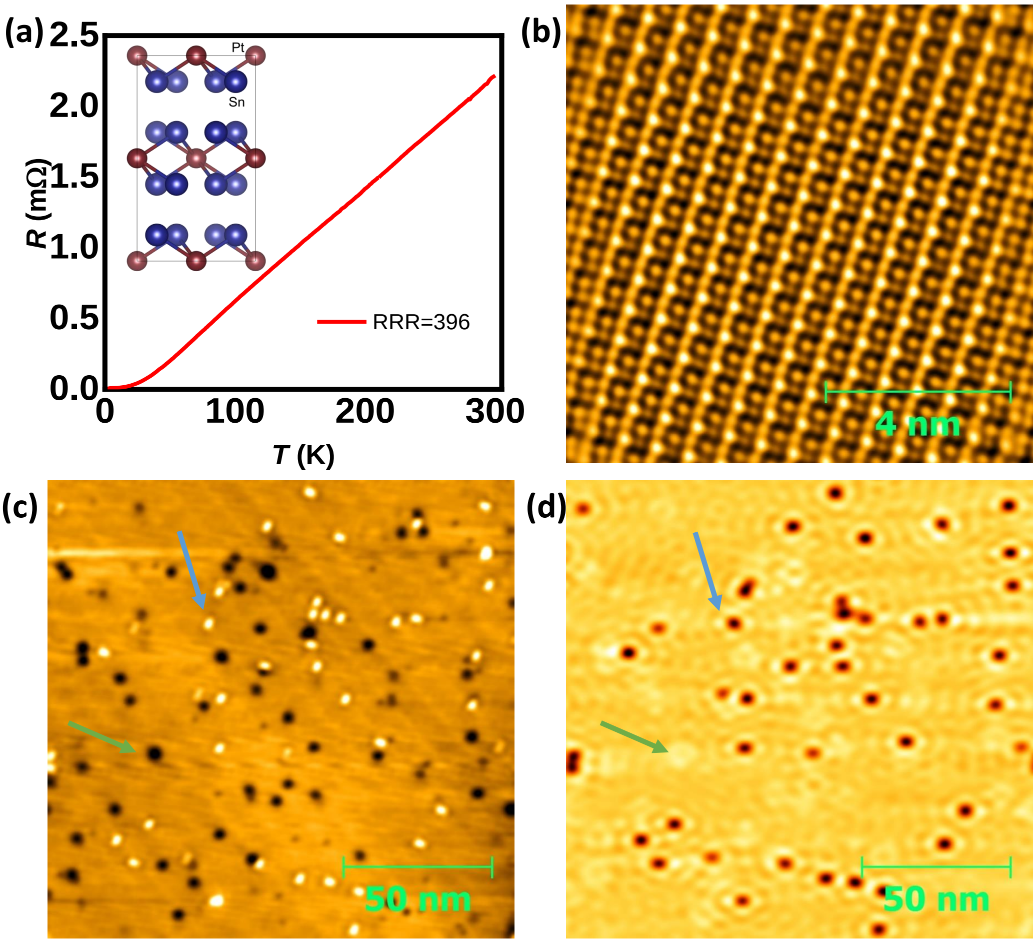

Fig. 7.1 **a** R-T data of the crystal. The orthorhombic unit cell of $PtSn_4$ is shown in the inset, **b** Atomic resolution image of cleaved surface of $PtSn_4$ **c** Large area topograph (154nm×154nm) showing bright and dark defects recorded at V_b = 100 mV and I_t=290pA. **d** dI/dV map of the topographic image shown in **c**.)

Where the sum runs over orbital index a. The spectral function in turn is obtained from the Green's function,

$$G_{aa}(k,\omega) = \sum_n \frac{|f_{a,n}(k)|^2}{(\omega + i\eta - \lambda_n(k))} \tag{7.3}$$

with $\lambda_n(k)$ are the band energies for a band n corresponding to a Hamiltonian H_k that has been obtained from a DFT calculation by our collaborators. Similarly, $f_{a,n}(k)$ represents the components of the eigenvectors of the Hamiltonian matrix.

The experimental momentum space QPI patterns for the conduction band, extracted at 300 mK, at energies 50 meV, 100 meV, 200 meV and 300 meV are shown in Fig. 7.2 **a-d**.

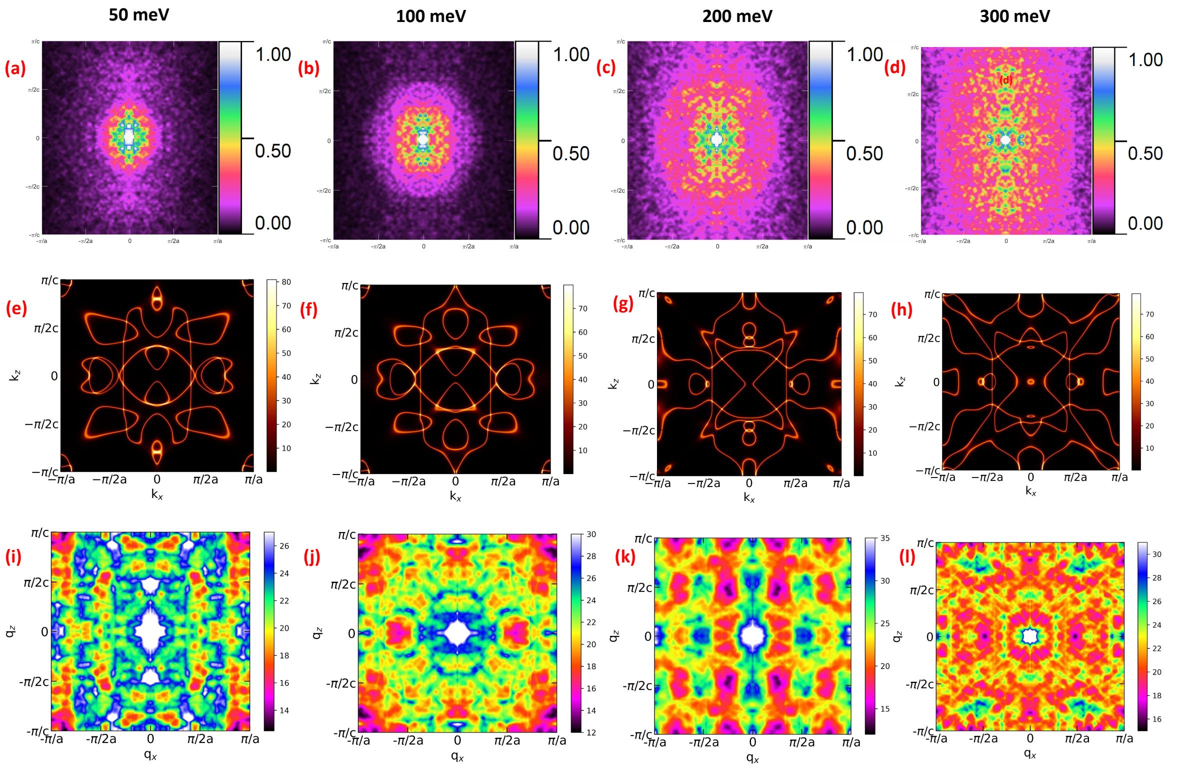

Fig. 7.2 **a-d** Experimentally measured QPI images for energies 50 meV, 100 meV, 200 meV and 300 meV. **e-h** shows the corresponding constant energy surfaces. **i-l**) are the simulated QPI plots with in a full BZ (-π to π).

The image processing details have been discussed at the end of this chapter. The evolution of the pattern between 50 meV and 300 meV is clearly seen. The calculated constant energy surfaces for the same energy values are shown in Figure 2(e-h). The corresponding simulated QPI plots are shown in Fig. 7.2 **i-l**. The simulated QPI within a full BZ (-π to π) reveals good agreement between experiment and theory, thereby confirming the validity of the model.

Now, to investigate the features associated with the topological properties of PtSn$_4$, we focus on the valence band QPI spectroscopy. The valence band experimental QPI plots recorded at energies -40 meV, -50 meV, -100 meV and -200 meV are shown in Fig. 7.3 **a-d**. The evolution of the pattern is clearly seen here as well. The calculated constant energy surfaces for the same energy values are shown in Fig 7.3 **e-h**. The corresponding simulated QPI plots are shown in Fig. 7.3 **i-l**. Again, a good agreement between the theoretical and the experimental QPI patterns is seen. Here we note that this agreement is, although the calculated QPI have been based on the bulk bands, confirming contributions of the bulk electronic structure to the surface JDOS.

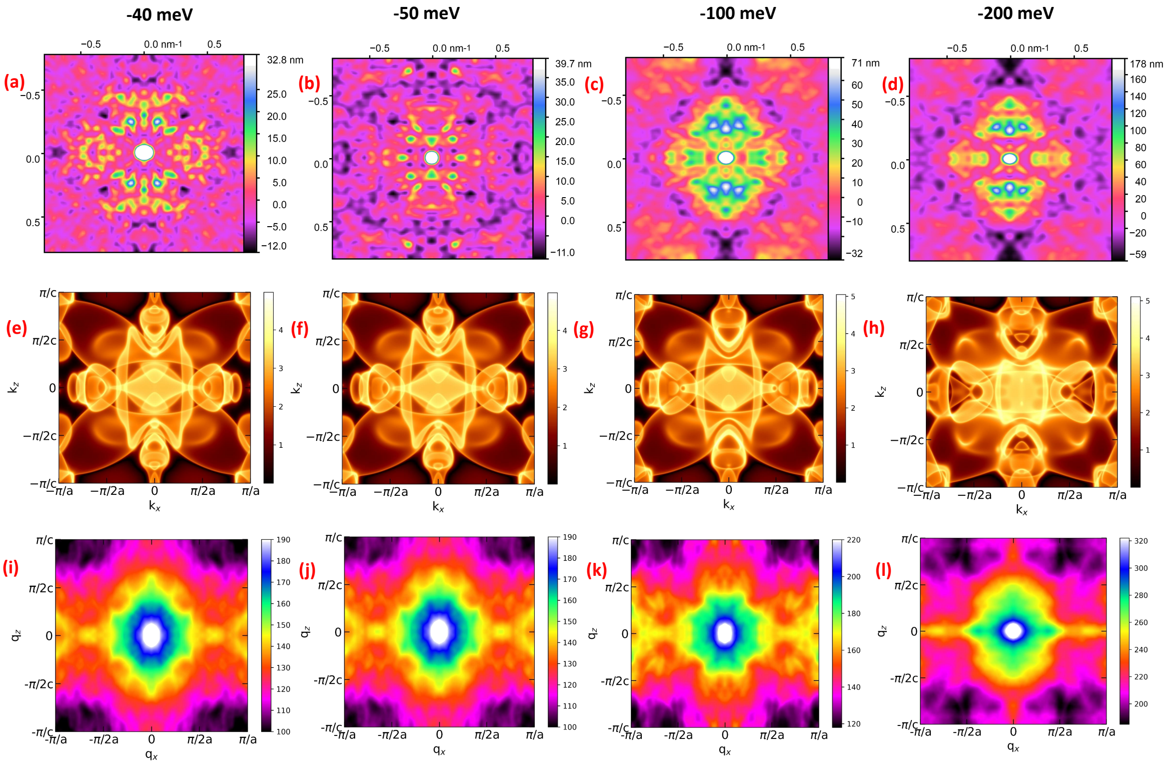

Fig. 7.3 **a-d** Experimentally measured QPI images for energies -40 meV, -50 meV, -100 meV and -200 meV. (e)-(h) shows the corresponding constant energy surfaces. **i-l** are the simulated QPI patterns with in a full BZ (-π to π).

Despite the agreement between theory and experiments discussed above, we also note that the QPI calculated from the bulk electronic structure cannot extract several peaks observed (experimentally) in the energy window around $E = -10$ meV, and that are dispersive for lower energies. To highlight this fact, we have separately considered the experimental QPI plot captured at -15 meV in Fig. 7.4 **a**. In this plot, we have marked three such scattering wave vectors (q_1, q_2, q_3) which could not be accounted for within our bulk band-based QPI calculations. Interestingly, these wavevectors show good agreement with expected JDOS contributions from nodal arc states found in Ref [69]. Particularly, the $q_1 \sim \frac{\pi}{4c}$ at $E = -15$ meV corresponds to an intra-pocket contribution from the nodal arc whereas the q_2, q_3 correspond to the inter pocket contributions. A qualitative sketch of the nodal arc state as obtained in Ref [69] showing the relevant q-vectors is given in Fig. 7.4 **a**. For lower energies, the q vectors seem to agree well with experimental QPI patterns shown in Fig 7.4 **b**. Therefore, we surmise that the QPI peaks at q_1, q_2, q_3 are due to contributions from the topological nodal arc states.

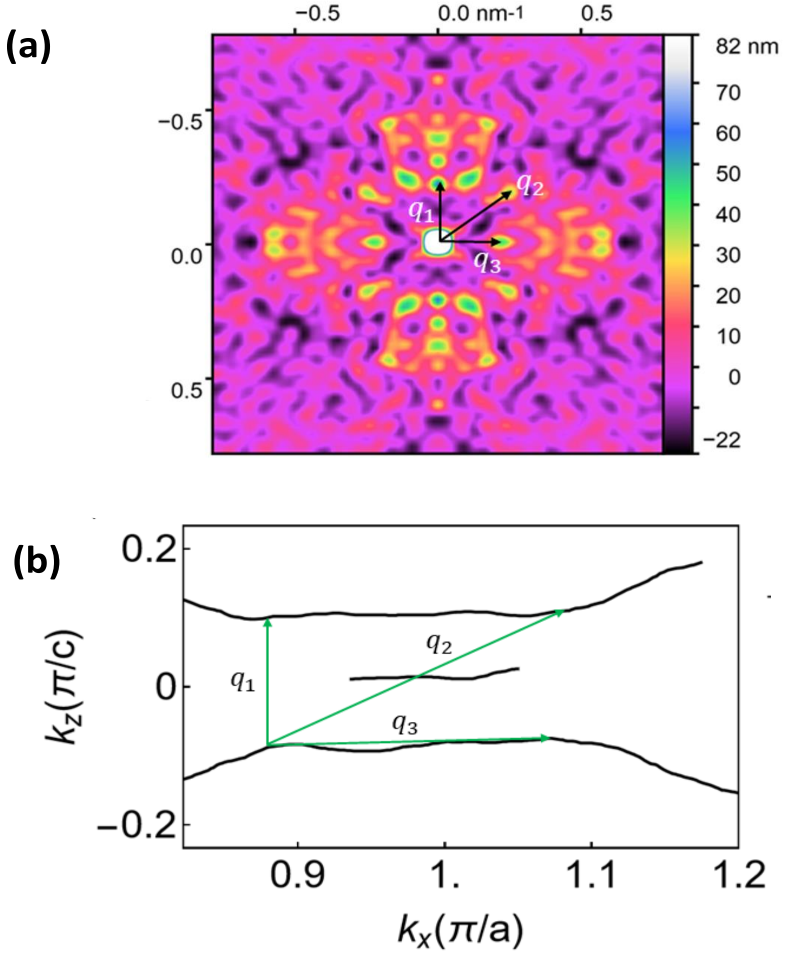

Fig. 7.4 **a** The experimentally extracted QPI patterns for -15 meV. **b** A qualitative sketch of nodal arc state. Relevant q vectors (q_1, q_2, q_3) are showing by the green arrows.

7.3 Image analysis

The image processing is done using Gwyddion software. The obtained atomic resolution topographic image had an oblique stretch due to piezo creep in the STM scanner at 77K. The obliqueness was constant for all scan rates and angles, which suggests that creep has a particular direction. Consequently, the lattice parameters we obtained were 7.182Å and 7.152Å instead of 6.418Å and 6.384Å, respectively. The oblique stretch was also evident from the obtained lattice angle 85.06° instead of the expected 90°. This error was corrected by an affine transformation. After the correction, we have observed that by a rotation of 47.70° to the image the lattice axes are aligned along the vertical (c-axis) and the horizontal (a-axis) direction respectively. Taking the correction parameters for the topographic image as the reference, the same correction was done on each DOS map. The corrected DOS map for -20 mV is shown in Fig. 7.5. The Fourier space image of a DOS map was obtained by Fast Fourier transformation (FFT). Blackmann windowing function was used to suppress the features from the discontinuity at the image boundary. To enhance the sharpness of the FFT image mean value was subtracted beforehand.

The root mean square (RMS) value was also preserved during the transformation. The FFT image was rotated by an angle of 47.70° and then symmetrized for both c and a-axes. The portion containing the first Brillouin zone (BZ) was cut from the symmetrized image for further processing (Fig. 7.6). Let us name this image $BZ_{\text{symmetrized}}$. The $BZ_{\text{symmetrized}}$ was then filtered by taking 2 pixels Gaussian averaging(Fig. 7.7). Let us call this image BZ_{Filtered}. The background was subtracted from BZ_{Filtered} to enhance the feature sharpness further. The background was extracted by 40 pixels Gaussian averaging of the $BZ_{\text{symmetrized}}$. The final image is presented in Fig. 7.8.

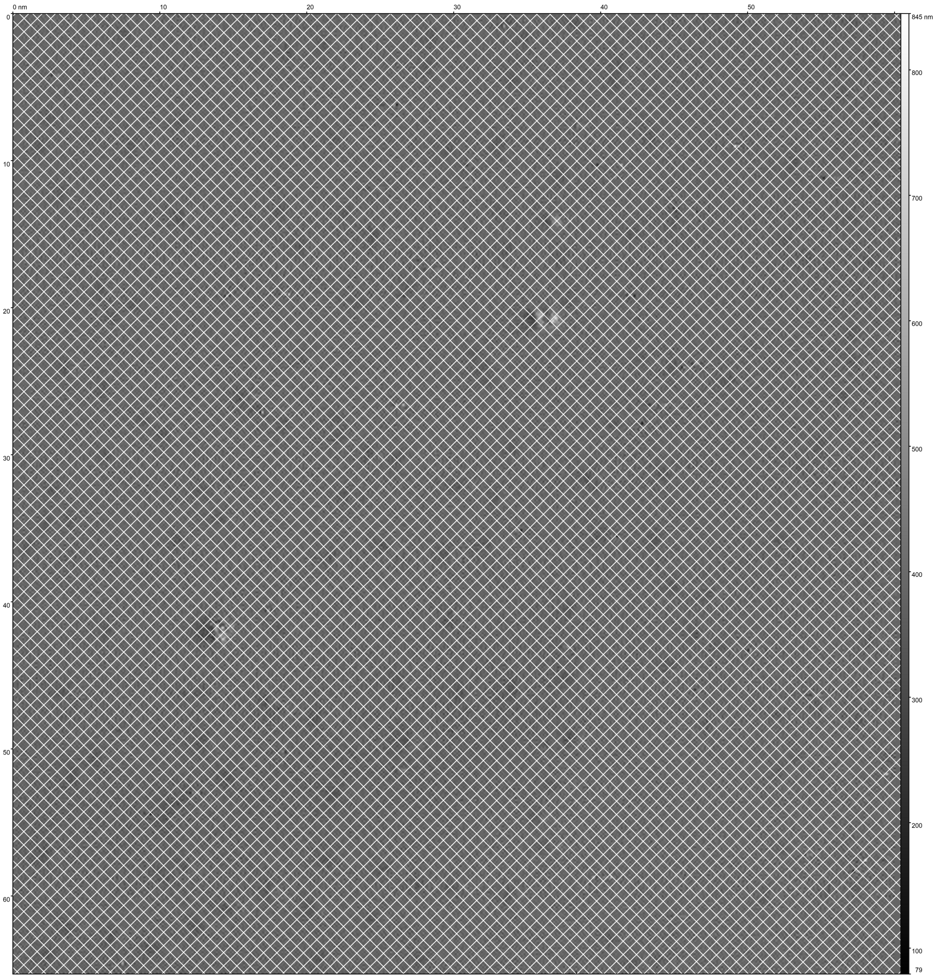

Fig. 7.5 Oblique corrected DOS map for -20 mV. The checker pattern is to represent the lattice after correction. Each node of the checker pattern represents one Pt atom.

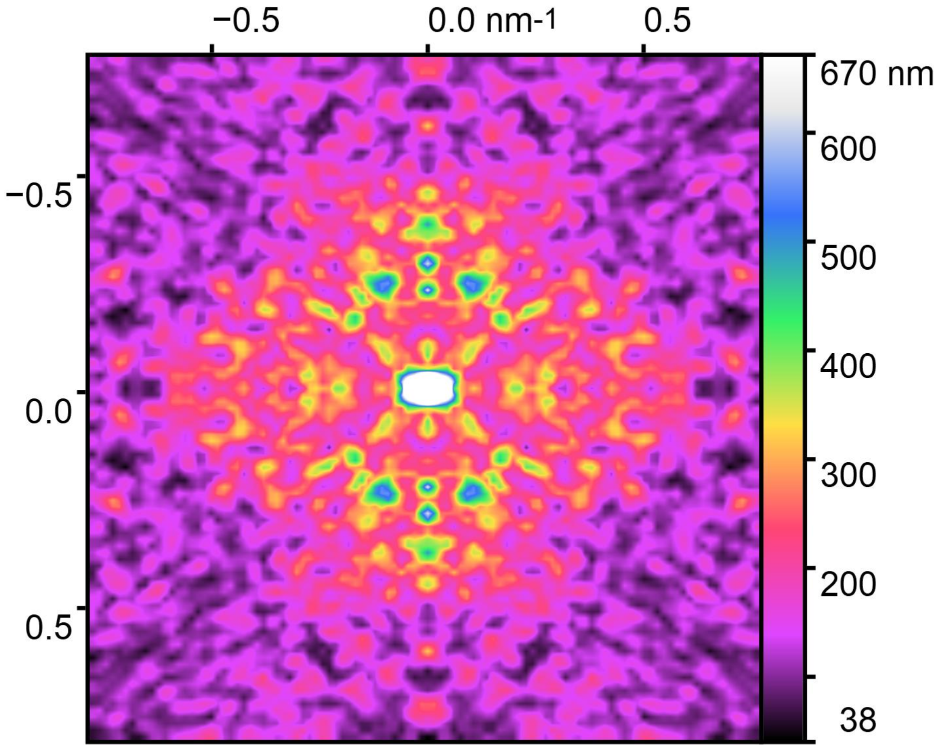

Fig. 7.6 Brillouin zone cut of the symmetrized FFT.

7.4 Conclusion

In conclusion, we have performed energy dependent quasiparticle interference (QPI) spectroscopy on the candidate nodal line semimetal $PtSn_4$. We found special scattering vectors in the momentum space that are not accounted for by our DFT-based bulk QPI simulations. We have presented how such special scattering vectors may emerge from the Dirac nodal arcs and inter-arc scattering. The findings are consistent with previous results obtained from ARPES experiments on $PtSn_4$.

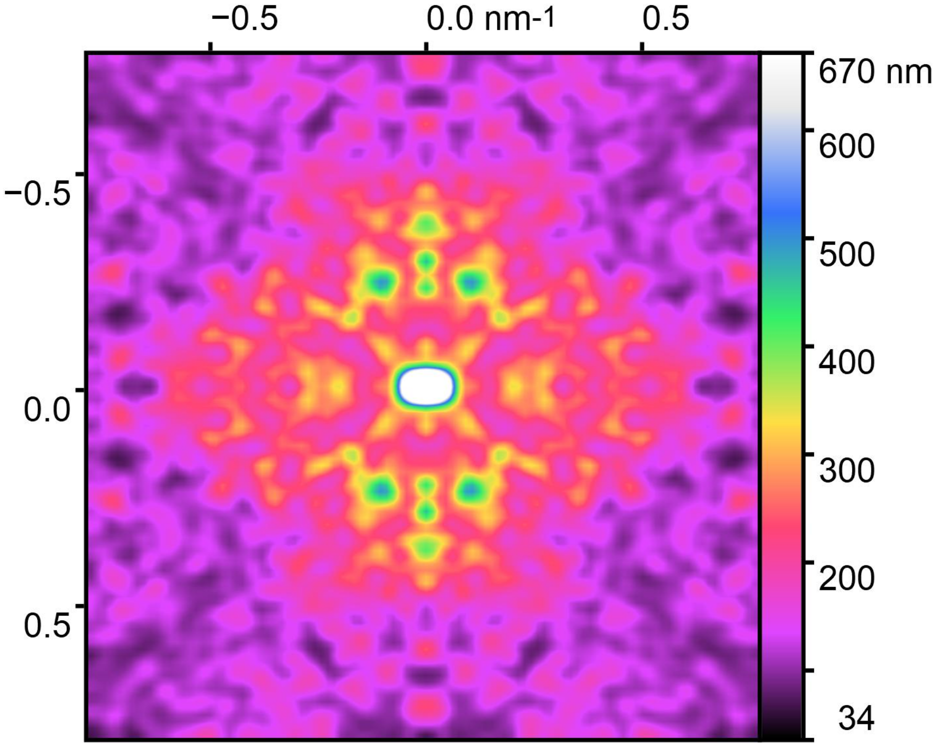

Fig. 7.7 After 2 pixels averaging to smooth the data

7.5 Contribution

- **PtSn$_4$ sample, Fig. 7.1 a:** Ratnadwip Singha and Shubhankar Roy, Saha Institute of Nuclear Physics, HBNI, 1/AF Bidhannagar, Kolkata 700 064, India; Prabhat Mandal, S. N. Bose National Centre for Basic Sciences, JD Block, Sector III, Salt Lake, Kolkata, PO 700106, India.

- **Theoretical analysis of QPI, Fig. 7.2 e-l, Fig. 7.3 e-l, Fig. 7.4 b:** Anirban Das, Mayank Gupta, B.R.K. Nanda and Shantanu Mukherjee, Center for Atomistic Modelling and Materials Design, Indian Institute Of Technology Madras, Chennai 600036, India.

- Some parts of the STS measurements were carried out jointly with Deepti Rana and Aastha Vasdev

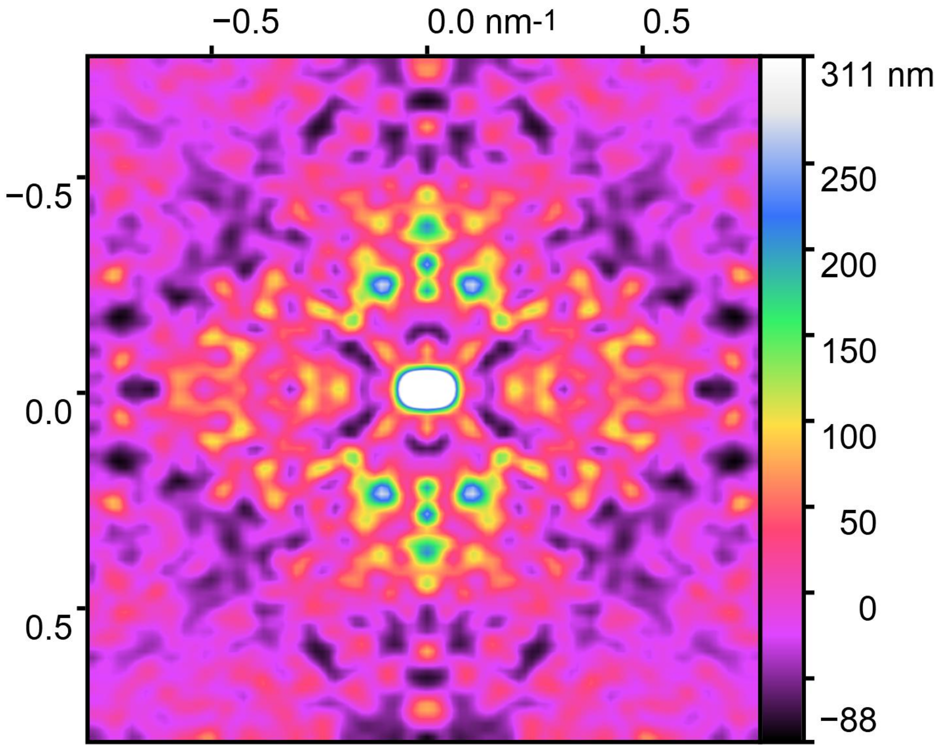

Fig. 7.8 Final QPI data after background subtraction.

Chapter 8

Concluding remarks

This thesis primarily encompasses my work in ultra-low temperature transport and spectroscopic imaging regime. To achieve our goal we have set up an ultra-low temperature laboratory from the scratch. We have designed our sample space for ultra-low temperature measurements in the dilution refrigerator. We set up an intelligent data acquisition protocol which mitigates the risk of boiling off liquid Helium when the magnet in the dilution refrigerator system is in driving mode. In this set up we have performed our magneto transport measurements to discover superconductivity in $LaVO_3$/ $SrTiO_3$ heterostructure interface. The discovered superconductivity is unconventional in nature and has mixed-order parameter. The unconventionality arises from the V-*d* bands in $LaVO_3$. The superconducting phase is fractured in space, like superconducting islands over a non-superconducting background. Our gate-dependent measurements revealed that the islands' sizes could be controlled using an electric field, which immediately suggested that the islands are connected to Ferroelectric domains. The existence of the ferroelectric domains could possibly be due to the expansive strain that the interface encounters due to the lattice mismatch of $LaVO_3$ and $SrTiO_3$. This new discovery is intriguing in its own sense.

We also have performed a spectroscopic investigation of $PtSn_4$, a proposed topologically non-trivial material with a Dirac nodal arc in the band that emerges from the surface states. Our objective was to probe the nodal arc states. To achieve that, we have employed ultra-low temperature scanning tunneling spectroscopy (STS) to acquire the quasi-particle interference (QPI) data on the surface. The experimental QPI data are in good agreement with theoretically produced data. In our experiment, we have found signatures that allow us to conclude that in QPI data, there are some states that originate from the nodal arc and inter-arc scattering.

Future Prospects

The $LaVO_3$/ $SrTiO_3$ interface should be investigated at the microscopic level to understand how the change in ferroelectric domains modulates the carrier density locally and the mechanism of carrier exchange between the islands and the background. This is also a potential system to study disordered low-dimensional superconductors where exotic phases (like Bose Metal) may be achieved by controling the disorder. Our QPI data on PtSn4 not only confirms the previous report of PtSn4 being a nodal arc semimetal but also helped to acquire further insights into the system, which will be beneficial in research in topologically non-trivial systems.

Bibliography

[1] A. Ohtomo & H. Y. Hwang, *Nature* **427**, 423-426 (2004).

[2] A. Ohtomo, D. A. Muller, J. L. Grazul & H. Y. Hwang, *Nature* **419**, 378-380 (2002).

[3] S. Thiel, G. Hammerl, A. Schmehl, C. W. Schneiderand & J. Mannhart, *Science* **313**, 5795 (2006).

[4] R. Ohtsuka, M. Matvejeff, K. Nishio, R. Takahashi & M. Lippmaa, *Applied Physics Letters* **96**, 192111 (2010).

[5] Pouya Moetake et al., *Applied Physics Letters* **99**, 232116 (2011).

[6] Y. Hotta, T. Susaki & H. Y. Hwang, *Phys. Rev. Lett.* **99**, 236805 (2007).

[7] K. Zou et al., *APL Materials* **3**, 036104 (2015).

[8] N. Wadehra et al., *Nature Communications* **11**, 874 (2020).

[9] H. Zhang et al., *Phys. Rev. Lett.* **121**, 116803 (2018).

[10] N. Nakagawa, H. Y. Hwang & D. A. Muller, *Nature Materials* **5**, 204–209 (2006).

[11] Z. Q. Liu et al., *Phys. Rev. Lett.* **107**, 146802 (2011).

[12] A. Ohtomo & H. Y. Hwang, *J. Appl. Phys.* **102**, 083704 (2007).

[13] G. Herranz et al., *Phys. Rev. Lett.* **98**, 216803 (2007).

[14] S. Ohta, T. Nomura, H. Ohta & K. Koumoto, *J. Appl. Phys.* **97**, 034106 (2005).

[15] C. Q. Tang, Z. Xia, S. Yao & S. Chen, *Cryst. Res. Technol.* **31**, 821 (1996).

[16] C. J. Shin, H. I. Yoo & C. E. Lee, *Solid State Ionics* **178**, 15–18 (2007)

[17] M. Basletic et al., *Nature Materials* **7**, 621–625 (2008)

[18] G. Herranz, F. Sánchez, N. Dix, M. Scigaj & J. Fontcuberta, *Scientific Reports* **2**, 758 (2012)

[19] N. Reyren et al., *Science* **317**, 5842 (2007).

[20] J. Biscaras, N. Bergeal, A. Kushwaha, T. Wolf, A. Rastogi, R.C. Budhani & J. Lesueur *Nature Communications* **1**, 89 (2010).

[21] A. D. Caviglia et al., *Nature* **456**, 624-627 (2008).

[22] Z. Chen et al., *Phys. Rev. Lett.* **126**, 026802 (2021).

[23] J. Bardeen, L. N. Cooper, and J. R. Schrieffer, *Phys. Rev.* **108**, 1175 (1957).

[24] M. Tinkham, Introduction to Superconductivity (McGraw-Hill, New York, 1996).

[25] R. A. Jishi, Feynman Diagram Techniques in Condensed Matter Physics (Cambridge University Press, 2013).

[26] L. Aggarwal et al., *Nature Materials* **15**, 32-37 (2016)

[27] C. C. Tsuei & J. R. Kirtley, *Rev. Mod. Phys.* **72**, 969 (2000)

[28] A. F. Andreev, *Sov. Phys. JETP* **19**, 1228 (1964).

[29] Y. G. Naidyuk and I. K. Yanson, Point-Contact Spectroscopy (Springer, 2005).

[30] R. Tomar et al., *Adv. Mater. Interfaces* **2019**, 1900941

[31] A. V. Mahajan, D. C. Johnston, D. R. Torgeson & F. Borsa, *Phys. Rev. B* **46**, 10966

[32] R. Tomar , S. Kakkar, C. Bera & S. Chakraverty, *Phys Rev. B* **103**, 115407 (2021)

[33] K. A. Müller & H. Burkard, *Phys. Rev. B* **19**, 3593 (1979)

[34] J. H. Haeni et. al, *Nature* **430**, 758–761 (2004)

[35] P. Das, R. Bruyn de Ouboter & K. W. Taconis, *Low Temperature Physics* **LT9** 1253–1255 (1965)

[36] Dr. Zuyu Zhao & Dr. Chao Wang, Cryogenic Engineering and Technologies, Principles and Applications of Cryogen-Free Systems (CRC Press).

[37] S. Goyal et al., *Solid State Communications*. **316–317**, 113930 (2020).

[38] J. Liang et al., *Proceedings of the National Academy of Sciences*. **117**, 221-227 (2020).

[39] C. C. Tsuei, & J. R. Kirtley, *Rev. Mod. Phys*. **72**, 969–1016 (2000).

[40] G. E. Blonder, M. Tinkham & T. M. Klapwijk, *Phys. Rev. B*. **25**, 4515–4532 (1982).

[41] A. Pleceník, M. Grajcar, Š. Beňačka , P. Seidel & A. Pfuch, *Phys. Rev. B*. **49**, 10016–10019 (1994).

[42] Y. Tanaka & S. Kashiwaya, *Phys. Rev. Lett*. **74**, 3451–3454 (1995).

[43] J. A. Sauls, *R. Soc. A*. **376**, 20180140 (2018).

[44] R. Kumar & G. Sheet *Phys. Rev. B*. **104**, 094525(2021).

[45] G. Sheet, S. Mukhopadhyay & P. Raychaudhuri, *Phys. Rev. B*. **69**, 134507 (2004).

[46] R. Tomar et al., *Adv. Mater. Interfaces*. **7**, 1900941 (2020).

[47] Y. Takabatake, I. S. Suzuki & Y. Tanaka, *Phys. Rev. B*. **103**, 184515 (2021).

[48] G. Binnig, H. Rohrer, Ch. Gerber & E. Weibel, *Phys. Rev. Lett.* **49**, 57 (1982).

[49] Samir Lounis, arXiv:1404.0961

[50] Jennifer Eve Hoffman, *PhD Thesis (2003): A Search for Alternative Electronic Order in the High Temperature Superconductor* $Bi_2Sr_2CaCu_2O_{8+\delta}$ *by Scanning Tunneling Microscopy*

[51] A. Burkov, *Nature Materials* **15**, 1145–1148 (2016).

[52] A. Bernevig, H. Weng, Z. Fang & X. Dai, *J. of the Phys. Soc. of Japan* **87**, 041001 (2018).

[53] B.Q. Lv, T. Qian, & H. Ding, *Rev. Mod. Phys.* **93**, 025002 (2021).

[54] N.P. Armitage, E.J. Mele, & A. Vishwanath, *Rev. Mod. Phys.* **90**, 0015001 (2018).

[55] C. Fang, H. Weng, X. Dai & Z. Fang *Chinese Phys. B* **25**, 117106 (2016).

[56] R. Yu, Z. Fang, X. Dai, X. & W. Hongming, *Front. Phys.* **12**, 127202 (2017).

[57] Yang et al. *Advances In Physics: X* **3**, 1414631 (2018).

[58] A. A. Burkov, M.D. Hook & L. Balents, *Phys. Rev. B* **84**, 235126 (2011).

[59] M. Neupane et al. *Nature Communications* **5**, 3786 (2014).

[60] Z. K. Liu et al. *Nature Materials* **13**, 677–681 (2014).

[61] S. Borisenkoet al. *Phys. Rev. Lett.* **113**, 027603 (2014).

[62] S.Y. Xu et al. *Science* **349**, 613–617 (2015).

[63] B. Q. Lv, et al. *Phys. Rev. X* **5**, 031013 (2015).

[64] L. Yang, et al. *Nature Physics* **11**, 728–732 (2015).

[65] Z. K. Liu et al. *Science* **343**, 864–867 (2014).

[66] Z. Wang et al. *Phys. Rev. B* **85**,195320 (2012).

[67] G. Bian et al. *Nature Communications* **7**,10556 (2016).

[68] L. M. Schoop et al. *Nature Communications* **7**, 11696 (2016).

[69] Y. Wu et al. *Nature Physics* **12**, 667–671 (2016).

[70] E. Mun et al. *Phys. Rev. B* **86**, 079909 (2012).

[71] J. Yan, et al. *J. Phys.: Condens. Matter* **32**,315702 (2020).

[72] X. Luo et al. *Phys. Rev. B* **97**, 205132 (2018).